December 2016

Characterizing the Performance of a Ferrofluid-Based Electromagnetic Energy Harvester under Direct and Parametric Excitations

Saad F. Alazemi
Clemson University, salazem@clemson.edu

Characterizing the Performance of a Ferrofluid-Based Electromagnetic Energy Harvester under Direct and Parametric Excitations

---

A Dissertation
Presented to
the Graduate School of
Clemson University

In Partial Fulfillment
of the Requirements for the Degree
Doctor of Philosophy
Mechanical Engineering

---

by
Saad Alazemi
December 2016

Accepted by:
Dr. Mohammed F. Daqaq, Committee Chair
Dr. Ardalan Vahidi
Dr. Gang Li
Dr. Lonny L. Thompson

Abstract

When a container carrying a magnetized ferrofluid is subjected to external mechanical stimuli, the sloshing motion of the magnetized ferrofluid generates a time-varying magnetic flux, which can be used to induce an electromotive force in a coil placed adjacent to the container. This process generates an electric current in the coil, and therewith, can be used to transduce external vibrations into electric energy providing a unique approach for vibration energy harvesting using liquid-state transduction materials. As compared to traditional vibratory energy harvesters that employ solid transduction elements, this approach offers several advantages including, but not limited to, conformability to different shapes and increased sensitivity to external excitations.

In this dissertation, a bench-top experiment was first constructed to demonstrate the feasibility of the proposed concept for vibratory energy harvesting. A rectangular plastic container carrying ferrofluid was placed inside a pick-up coil which is wound around a ferrite core. The whole setup was mounted on an electrodynamic shaker table which provided a controlled acceleration at the containers base. The external magnetization is applied using permanent magnets with maximum magnetic field intensity of 92 mT. Series of experiments were carried out to determine the optimal configuration of coil windings with respect to the sloshing and magnetic field directions. It was found that the output power of the device increases an order of magnitude when the coil is wound perpendicular to the sloshing motion and magnetic field lines.

For the optimal configuration determined experimentally, a nonlinear analytical model which governs the electro-magneto-hydrodynamics of the harvester was developed. An approximate analytical solution of the model was obtained using perturbation methods for two different types of excitation; namely for a case involving the primary resonance excitation of the first mode and a case involving the principle parametric resonance of the first two modes.

For the case involving the primary resonance of the first mode, it was observed the approxi-

mate analytical solution fails to capture the qualitative behavior of the harvesters response for some ferrofluid height to container width ratios. Upon further inspection, it was observed that for those critical height-to-width ratios, the sloshing conditions are such that a two-to-one internal resonance between the first two sloshing modes can be activated. To account for the internal resonance, a modified version of the perturbation solution was devised and used to obtain a solution of the governing equations capable of capturing the influence of the internal resonance on the dynamics.

Overall, it was shown that the developed model is capable of capturing the qualitative behavior of the dynamics of the harvester for both cases of excitation and for various magnetic field distributions. It was observed that the orthogonality of the magnetic field distribution along the width the container to the shape of the mode being excited plays a critical role in determining the output power of the harvester. Specifically, regardless of the input excitation level and the size of the induced sloshing waves, very little energy can be harnessed from the environment when the magnetic field distribution is an even (odd) function of the containers width while the mode shape being excited is an odd (even) function of the width. It was shown that, unlike the primary resonance scenario, a threshold excitation level must be achieved in the principle parametric resonance case before the harvester can produce measurable voltage levels. This threshold increases with the strength of the applied magnetic field.

Dedication

This dissertation is dedicated to the memory of my beloved father, my wonderful mother, my brothers, my sisters, and to my loving and supportive wife, Eiman, and to my children, Ali and Hana.

Acknowledgments

First, I would like to thank God for all He has and continue to bestow on me; for giving me a wonderful family, a great advisor, and the opportunity to complete this work.

I would like to express my special appreciation and thanks to my advisor Dr. Mohammed Daqaq. He has been a tremendous mentor for me, and a best friend for me and my family. I would like to thank him for his encouragement, motivation, patience, and invaluable guidance. Without his guidance, and support, it would have been impossible to conduct this research. Special thanks to Dr. James Gibert; for his support during my first year in Clemson and for his endless friendship.

My sincere thanks also goes to my committee members: Dr. Ardalan Vahidi, Dr. Gang Li, and Dr. Lonny L. Thompson, for their insightful comments, suggestions, and encouragement. I also thank all the professors I have taken courses with: Dr. Mohammed Daqaq, Dr. Ardalan Vahidi, Dr. Georges Fadel, Dr. Jim Brannan, Dr. Brian Fralix, Dr. Robert Lund, and Dr. Patrick Gerard. Also, I would like to thank the great staff members and technicians: Ms. Gwen Dockins, Mr. Jamie Cole, Mr. Michael Justice, and Mr. Stephen Bass for their help which has played an important role in the completion of this work.

I extend special thanks to my colleagues and office mates: especially Dr. Amin Bibo for his collaboration, endless help, late nights discussions, invaluable comments and his friendship; Dr. Meghashyam Panyam, Abdraouf Abusoua, Dr. Ali Alhadidi for all the help, support, and making my years in the office and the lab enjoyable and memorable. Also, I would like to thank Dr. Ravindra Masana, Clodoaldo Silva, Dr. Gregory Batt, Qifan He, Yuhao Wang, Raveen Kumar, Wen-an Jiang, and Yawen Xu.

My deepest gratitude goes to my family without whom it would have been impossible to realize this dream: My wonderful mother, Hana Aboud, for her kindness, unconditional love, encouragement, support, and for her lovely smile all the time. My brother Ali, for his endless help,

encouragement, unquestionable support, and making every thing easy for me, many thanks for him. My brothers and sisters, Sara, Nadiya, Nora, Nawal, Magboula, Fowziyah, Ghanima, Manal, Najat, and Saud.

This last word of acknowledgment I have saved for my dear wife Eiman Alazemi, who has been with me all these years and has made them the best years of my life. Her endless support, encouragement, and quiet patience was in the end what made this dissertation possible. I also dedicate this Ph.D. thesis to my two lovely children, Ali and Hana who have given me much happiness and kept my hopes and dreams alive. Each one is deeply loved in a unique way. My son, Ali, has grown up watching me study and juggle between family and work. Hana, the little one, always tries to do everything possible to make her presence felt. Each has contributed immeasurably to family enjoyment in a very special way. I hope I have been a good father and that I have not lost too much during the tenure of my study. I love you more than anything.

Table of Contents

List of Tables

List of Figures

Chapter 1

Introduction

1.1 Motivations

Energy harvesting is the process by which ambient energy is captured and transformed into a useful form. Historically, mankind has relied on this process to fill its basic energy needs using windmills, sailing ships, and waterwheel. However, our ever increasing energy demands and changing research trends is pushing these old concepts into newer directions. Today, we continue to produce smaller and lower-power consumption devices that span different fields of technology. Wireless sensors, data transmitters, microcontrollers, and implantable medical devices that require only sub-milliwatts of average power to function are being developed [1, 2, 3, 3]. Unfortunately, further evolution of such technologies is currently being moderated by the lack of continuous scalable energy sources that can be used to power and maintain them. Batteries, which remain the most adequate power choice, have not kept pace with the device's demands, especially in terms of energy density [4]. In addition, their finite life span which necessitates regular replacement can be a very costly and cumbersome process. Consider, for instance, the difficulty of replacing batteries for a spatially-dense remotely-located wireless sensor network, or the risks involved in changing batteries for patients with implantable pace makers.

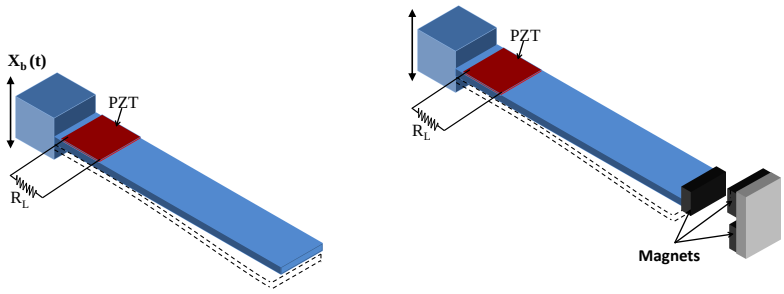

(a) (b)

Figure 1.1: Schematics of piezoelectric energy harvester.

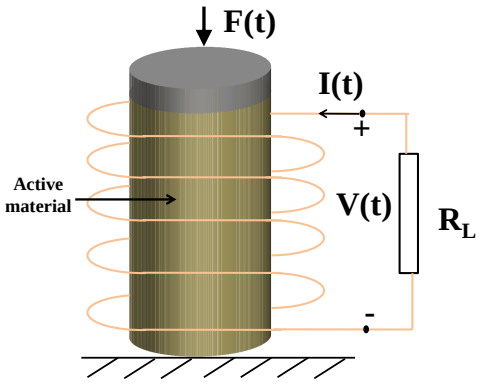

Figure 1.2: A schematic of a magnetostrictive energy harvester

1.2 Current Approaches: Solid-State Energy Harvesting

The past decade has witnessed a new evolution in energy harvesting technologies whereby the concept of micro-power generators (MPGs) was introduced [5, 6, 7, 8, 9]. MPGs are compact energy harvesting devices that can transform the smallest amounts of available wasted ambient energy into electricity. When embedded with electronic devices, these generators can provide a continuous power supply permitting an autonomous operation process. Within the vast field of micro-power generation, vibratory energy harvesting has flourished as a major thrust area. Various devices have been developed to transform mechanical motions directly into electricity by exploiting the ability of active materials (piezoelectric, and magnetostrictive) and electromechanical coupling mechanisms (electrostatic, and electromagnetic) to generate an electric potential in response to mechanical stimuli and external vibrations [10, 11, 12, 13, 14]. Typically, vibratory energy harvesters incorporate a solid-state material for energy transduction. For instance, in piezoelectric and magnetostrictive energy

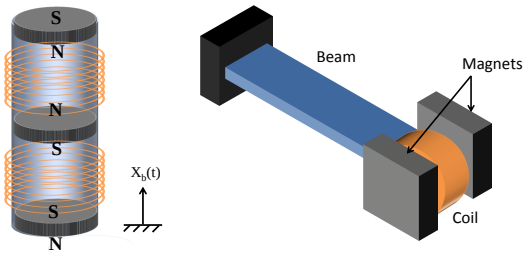

(a) (b)

Figure 1.3: Schematics of (a) Magnetostrictive, and (b) Electromagnetic energy harvesters.

harvesting as shown in Fig. 1.1 and Fig. 1.2, respectively, the strain produced in a piezoelectric beam or a magnetostrictive rod is transformed into electric charge or magnetic field via the piezoelectric and Villari effects, respectively [15, 16, 17]. Similarly, as shown in Fig. 1.3, in electromagnetic energy harvesters, external vibrations set a *solid* magnet in motion relative to a stationary coil or vise versa [5, 6, 18, 19, 20]. As per Faraday's law, the change in magnetic flux produces a current in the coil which can then be channeled into an electric load.

The solid-state nature of the transduction mechanism in current vibratory energy harvesters can place limitations on their capabilities especially in terms of conformability to different shapes and sensitivity to external excitations. This has lead the authors, among a few other researchers, to explore the use of liquid-state materials to transduce mechanical motions into electricity [21, 22].

1.3 Proposed Approach: Liquid-State Energy Harvester

Motivated by the obvious need for a scalable, sensitive, and conformable energy harvester, this endeavor proposes the use of liquid-state materials, namely ferrofluids, as the transduction mechanism in electromagnetic vibratory energy harvesters.

Ferrofluids were invented by NASA in 1962 as a liquid fuel for rocket applications and have since been used in many critical applications. For instance, ferrofluids have been investigated as a drug transport medium inside the human body. By using an external magnetic field force the drug can be transferred and held in the desired location and allowed to act for a period of time [23]. Furthermore, using the ferrofluid ability to convert electromagnetic energy into thermal energy, other researchers have also investigated heating the ferrofluid to achieve hyperthermia in

order to treat tumors [24]. Ferrofluids have also been studied as (i) an enhanced contrast agent for magnetic resonance imaging MRI [25]; (ii) working fluid in heat exchangers in order to enhance the heat transfer performance by changing the thermo-physical properties of the ferrofluid using an external magnetic field [26]; (iii) seals and lubricators because of their ability to provide positive pressure barrier; (iv) specialty coating systems; and (v) sensors, environmental seals, film bearings, and nuclear magnetic resonance (NMR) probes [27, 28].

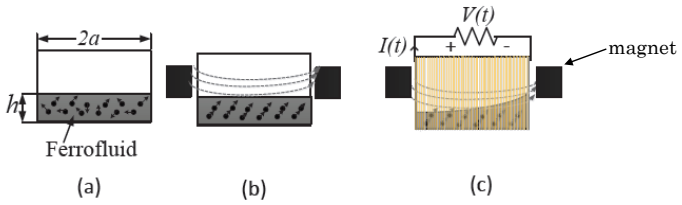

Figure 1.4: Schematics of ferrofluid particles (a) without external magnetization (b) with external magnetization (c) with external magnetization and base excitation.

Generally, ferrofluids consist of stable ferrous nanoparticles in colloidal suspension forming nanoscale permanent magnetic dipoles [29]. Each magnetic dipole is coated with a surfactant such that, in the absence of an external magnetic field, the magnetic dipoles are randomly oriented in the carrier fluid as shown in Fig. 1.4(a). However, when an external static magnetic field is applied, the dipoles rotate and produce a net magnetic moment such that the average direction of the fluid magnetization is parallel to the external field as shown in Fig. 1.4(b). When the magnetized fluid is subjected to external excitations with a frequency that matches one of the infinite modal frequencies of the fluid column (resonance condition), large amplitude surface waves, both horizontal and rotational, are excited, Fig. 1.4(c). The motion of the sloshing liquid creates a time-varying magnetic flux which can then be used to induce an electromotive force in a coil adjacent to the container. This process generates an electric current, $I(t)$, and therewith, transduce external vibrations into electric energy.

As shown in Fig. 1.5, the orientation of the magnetic dipoles relative to the magnetic field lines depends on the strength of the applied field; in a weak magnetization region, the magnetic field has a little influence on the direction of the dipoles; whereas, within the highly magnetized regions, the dipoles are strongly coupled to the applied field, and, are, hence, very hard to rotate.

The key significance of this novel concept for micro-power generation stems from the following advantages:

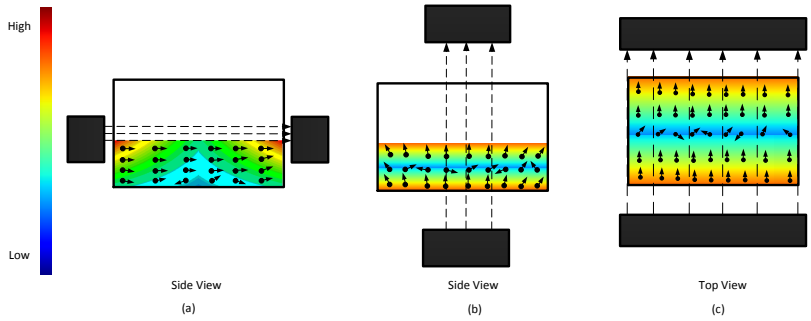

Figure 1.5: Magnetization of dipoles as a function of the applied magnetic field.

- **Conformability**: Since fluids can easily conform to different shapes, it permits the development and fabrication of energy harvesters with complex shapes, much more complex than the simple shapes that can be achieved using solid-state magnetic materials. This important quality will undoubtedly open new, and previously thought impractical applications, for energy harvesting.

- **Sensitivity**: Liquids are much more sensitive to low-level excitations than solids are; this is one reason why mammals ears incorporate a fluid called the Perilymph to transform mechanical vibrations from the middle ear into waves that can be carried to the sensory ducts at the end of the cochlear. Thus, it is believed that liquid-state materials are capable of responding to the smallest levels of environmental excitations including, but not limited to, the nature-common acoustic excitations.

- **Tunability**: The viscosity, and hence, stiffness of ferrofluids can be changed by applying an external magnetic field, a phenomena that has been documented and well-studied in the literature [30]. This occurs due to the action of the magnetic field which hinders the rotation of the individual dipoles. Thus, the modal frequencies of the fluid column can be tuned to the excitation frequency to maximize transduction efficiency by applying a static magnetic field. The field can be generated using a solid magnet, and, hence, does not consume additional power.

- **Enhanced Bandwidth**: Most linear energy harvesters operate efficiently only within a narrow frequency bandwidth where the excitation frequency is very close to the fundamental frequency of the harvester (resonance condition). Small variations in the excitation frequency around the harvesters fundamental frequency drop its small energy output even further making the energy harvesting process inefficient [31, 32, 33]. This becomes an even more pressing issue when one

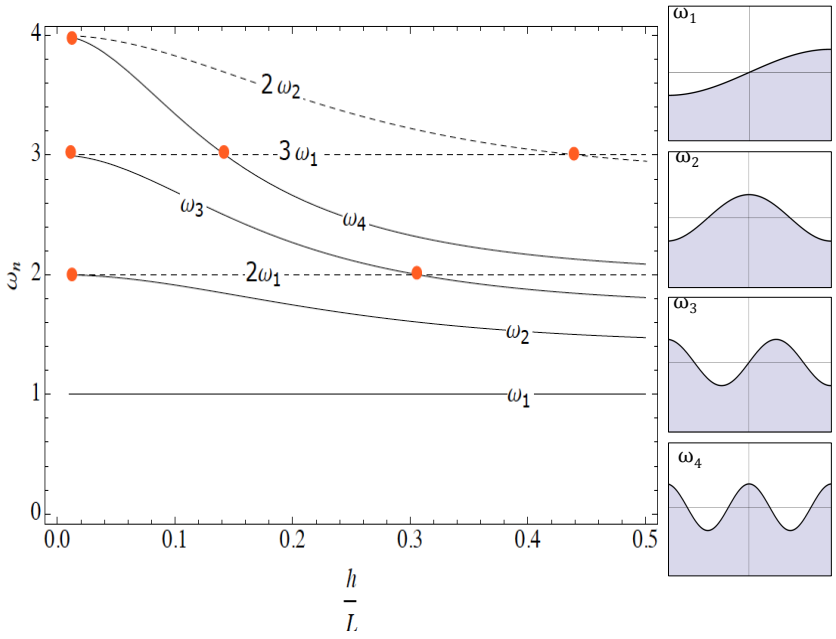

Figure 1.6: Variation of the modal frequencies of the fluid column with h/L

realizes that most environmental excitations have a broad-band or time-dependent characteristics in which the energy is distributed over a wide spectrum of frequencies or the dominant frequencies vary with time. Electromagnetic energy harvesters that incorporate solid-state magnets respond only at one modal frequency similar to the devices proposed by Mann and Sims [34] or at widely-spaced modal frequencies similar to the devices discussed in reference [35]. As such, they have a very narrow response bandwidth. A harvester incorporating liquid-state materials can respond at infinitely many closely-spaced frequencies, corresponding to the infinite modal frequencies of the fluid column which excite the large amplitude rotational and horizontal surface waves. The presence of a large number of closely-spaced modal frequencies can also facilitate the activation of nonlinear modal interactions between the different vibration modes. Such interactions occur when two or more modal frequencies of a certain nonlinear system are commensurate or nearly commensurate [36], i.e. multiple integers of each other. Fig. 1.6 depicts variation of the first flow modal frequencies of the fluid column with the hight-to-width ration, in a rectangular container. The figure illustrate that the modal frequencies are closely spaced and can become multiple integers of each others especially for small heights. This can lead to energy exchange among the commensurate modes resulting in large-amplitude responses over a wide range of frequencies which

broadens the voltage-frequency response curves, further enhancing the broadband characteristics of the ferrofluid-based harvester.

1.4 Dissertation Objectives and Contributions

In this electro-magneto-hydrodynamical device, fluidic, magnetic, and electrical domains play an interconnected, but yet unknown role, which is essential to characterize the harvester's performance. For instance, the volume, depth, and material properties of the ferrofluid; the strength and spatial distribution of the magnetic field; and the electric load, all influence the spatio-temporal evolution of the surface waves, which, in turn, governs the output power of the device. The availability of an accurate mathematical model of the system will undoubtedly aid in enhancing its performance, opening new avenues for energy harvesting. With this understanding, this dissertation aims to build the fundamentals necessary to evaluate and maximize the transduction efficiency of liquid-state (ferrofluid based) materials for harvesting vibration energy. To achieve this goal, the specific objectives of this dissertation are:

- **Develop an experimental proof-of-concept of the harvester:** The first objective of this thesis is to demonstrate that the sloshing of ferro-fluids in a base excited container can be used to harness energy effectively from a vibration source. To achieve this goal, a plastic rectangular container carrying a ferrofluid is placed inside a pick-up coil which is wound around a ferrite core and the whole setup is mounted on an electrodynamic shaker table which will be directly excited from the base as shown in Fig. 1.7. The external magnetization is applied using permanent magnets and the intensity and spatial distribution of the magnetization are varied by changing the external permanent magnets placement.

- **Determine the optimal configuration of the harvester:** In order to maximize the harvester's performance, it is essential to first characterize the optimal design configuration. For a given number of turns and cross-sectional area of the pick-up coil, the electromechanical coupling, and thereby, the output power changes significantly depending on the following three configuration parameters:

    1. Direction of magnetization with respect to windings.
    2. Direction of magnetization with respect to sloshing.

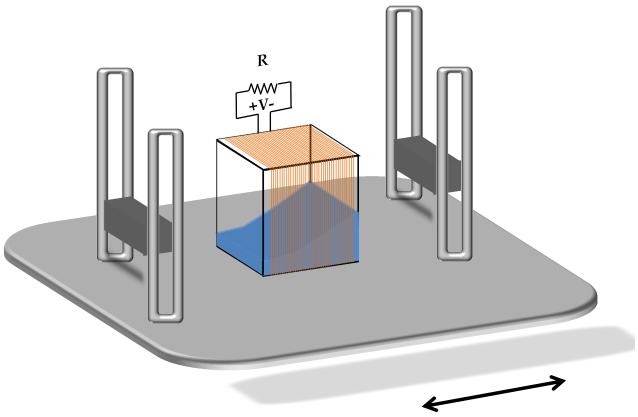

Figure 1.7: A schematic of the experimental system.

3. Direction of winding with respect to sloshing.

Therefore, the first goal of this experimental study is to investigate the optimal configuration of the harvester by assessing the relative performance for the aforementioned conditions.

- **Utilize nonlinear modal interactions to enhance the performance of the harvester:** Upon determining the optimal configuration, a series of experimental studies will be conducted to show that nonlinear modal interactions between the different vibration modes can be activated and used to improve the bandwidth of the harvester. To achieve this goal, we specifically choose the dimensions of the container and the height of the fluid column such that the modal frequencies of the sloshing ferrofluid are nearly commensurate. It is shown that this choice of parameters activates a two-to-one internal energy pump between the commensurate modes resulting in large-amplitude voltages over a wide range of frequencies, thereby improving the steady-state bandwidth of the harvester.

- **Invoke several assumptions on the fluid dynamics and magnetization of the ferrofluid to obtain an analytical model of the harvester:** By invoking several justifiable assumptions on the response behavior, we formulate an analytical model which describes the electro-magneto-hydrodynamics of the system. The model is able to capture, with reasonable accuracy, *i*) the magneto-hydrodynamic behavior which deals with the motion of the magnetized fluid in the container, and *ii*) the electromagnetic induction which deals with characterizing how the fluid motion is induced into electrical energy.

- **Use perturbation theory to obtain an approximate analytical solution of the model for the primary resonance case:** By linearizing the dynamics assuming small surface waves, we investigate variation of the modal frequencies with the height-to-width ratio of the fluid and identify the regions where internal resonances can be activated. Using the method of multiple scales, we obtain an approximate analytical solution of the harvester's response to a primary resonance direct base excitation of the first mode. We use the resulting solution to study the voltage response of the harvester at different fluid heights and for different magnetization profiles. We construct an experimental set up and use it to validate the resulting model. Finally, we present our conclusions regarding the validity of the model.

- **Assess the performance of the harvester under parametric excitations:** In addition to analyzing the response of the harvester to direct excitations; i.e., harmonic excitations that are perpendicular to the height of the container, we will also study performance under parametric excitations; i.e., excitations that are parallel to the height of the container. It is well known that when exciting a fluid columns parametrically near twice one of the its modal frequencies, large amplitude waves, also known as Farady's waves can be excited. To achieve this goal, a series of experiments will be carried out to assess performance in the parametric resonance case. An analytical model will also be obtained and solved for the parametric excitation scenario.

1.5 Dissertation Outline

The rest of the manuscript is organized as follows: In Chapter 2, the potential of utilizing a ferrofluid-based energy harvester to scavenge energy from vibratory base excitations is investigated. A series of experiments are carried out to investigate the optimal configuration of the harvester. Using the optimal configuration, a specific set of parameters are chosen to activate a two-to-one internal resonance between the first two vibration modes and used to illustrate that the internal resonance serves to improve the bandwidth of the harvester. In Chapter 3, a distributed-parameters nonlinear model of the harvester subjected to direct base excitation is derived. An approximate analytical solution of the model under primary resonance excitation is obtained using the method of multiple scales and compared to experimental findings. In Chapter 4, the performance of the harvester will be investigated under parametric excitations experimentally. An analytical model will also be obtained and solved for the parametric excitation scenario. Finally, Chapter 6 presents the

main conclusions of this research.

Chapter 2

Experimental Investigation

2.1 Operation Principle of the Harvester

Generally, when a container carrying a magnetized fluid is subjected to an external excitation, the fluid sloshes inside the container creating large surface waves, which, generates a change in the magnetic flux. According to Faraday's law of induction, variations in the magnetic field environment of a conductor induces a back electromotive force which can be used to generate a current in a closed-loop conductor. As such, when a coil is wound around the container, the motion of the fluid can be used to generate an electric current which can be harnessed to power electronic devices.

The magnetic flux, ϕ, passing through a given area, A, is defined as the dot product of the magnetic field vector with the unit vector normal to the area, i.e,

$$\phi = \mathbf{B}.\mathbf{A} = BA\cos\theta, \tag{2.1}$$

where θ is the angle between the magnetic field lines and the normal to the area formed by the loop. According to Lenz's law, the induced voltage, also known as the back electromotive force (emf), can be related to the change of flux through

$$\text{emf} = -N\frac{\partial\phi}{\partial t} = N\left(-\frac{dB}{dt}A\cos\theta - B\frac{dA}{dt}\cos\theta + BA\sin\theta\dot{\theta}\right), \tag{2.2}$$

where N is the number of turns. By inspecting Equation (2.2), it becomes evident that, for a

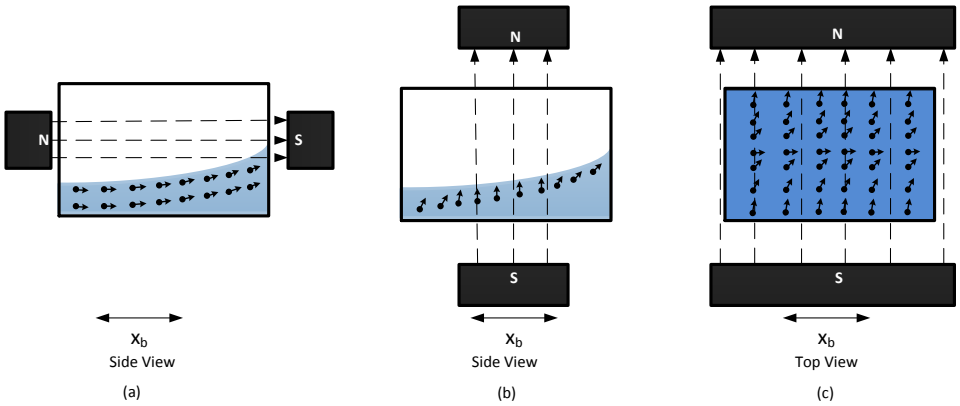

Figure 2.1: The effect of sloshing on the dipoles magnetization direction and the dipoles traveling path for different magnet placements

constant coil area, the back emf can be induced in the coil in one of the following ways:

1. Changing the magnitude of the field B with time; which is achieved by the bulk motion of the dipoles inside the container.

2. Varying the angle between the dipoles and the area vector A, which can occur when the sloshing motion of the fluid forces the dipoles to change their orientation.

2.2 Optimal Configuration

Based on this understanding, Fig. 2.1 illustrates three different scenarios for current induction, and hence, energy harvesting. In the first scenario, the sloshing direction is parallel to the magnetic field lines (parallel sloshing motion) and the change in flux is mainly due to the bulk motion of the fluid in the container due to the tidal motion of the fluid specially near the side walls. In the second scenario, the magnetic field lines are normal to the sloshing direction. Here, in addition to the bulk motion, the sloshing motion forces the dipoles to rotate with respect to the magnetic field lines. In the third scenario, also known as the cross-sloshing motion, little dipole rotation occurs and the change in flux is mainly due to the bulk motion of the fluid.

In order to maximize the harvester's performance, it is essential to first characterize the optimal design configuration. For a given number of turns and cross-sectional area of the pick-up coil, the electromechanical coupling, and hence, the output power change significantly depending on

the following three configuration parameters:

1. Direction of magnetization with respect to windings which determines the strength of the magnetic flux.

2. Direction of magnetization with respect to sloshing. When the magnetic field is parallel to the sloshing direction, the dipoles are magnetized parallel to the sloshing direction. This reduces the fluid's resistance to motion, which generally increases the relative speed of the moving dipoles. As a result, the rate of change of the magnetic flux increases.

3. Direction of winding with respect to sloshing. This affects both of the portion of the coil area experiencing a change of flux and the relative speed of the magnetic dipoles.

Therefore, the first goal of this experimental study is to investigate the optimal configuration of the harvester. Towards that end, the experimental setup depicted in Fig. 3.6 is constructed. A plastic cubic ferrofluid container with each side measuring at 10.16 cm is placed inside a pick-up coil which is wound around a ferrite core and the whole setup is mounted on an electrodynamic shaker table. The external magnetization is applied using permanent magnets with maximum magnetic field intensity of 92 mT. The intensity and the spatial distribution of the magnetization are varied by changing the external permanent magnets placement. A dSpace system is used for the purpose of controlling the shaker and for data acquisition. The harvested voltage is measured across a resistive load connected in parallel to the pick-up coil. The physical properties of the ferrofluid and the harvester are listed in Table 3.1.

Table 2.1: Harvester's properties and specifications.

Property	SI Units
Ferrofluid Flash Point	92°
Ferrofluid Initial Magnetic Susceptibility	3.52
Ferrofluid Viscosity at 27°	12 mPa.s
Ferrofluid Density at 25°	1420 kg/m^3
Number of Coil Turns	1500
Inductance of Coil Turns	1.55 H
Coil Resistance	254 Ohms

A series of experiments are then conducted to find the optimal configuration which yields the highest change in magnetic flux. The experiments are performed in the frequency domain at a constant base acceleration applied directly to the coil-tank assembly. In the first set of experiments, magnets of opposite polarity are used with different placement directions such that they produce a

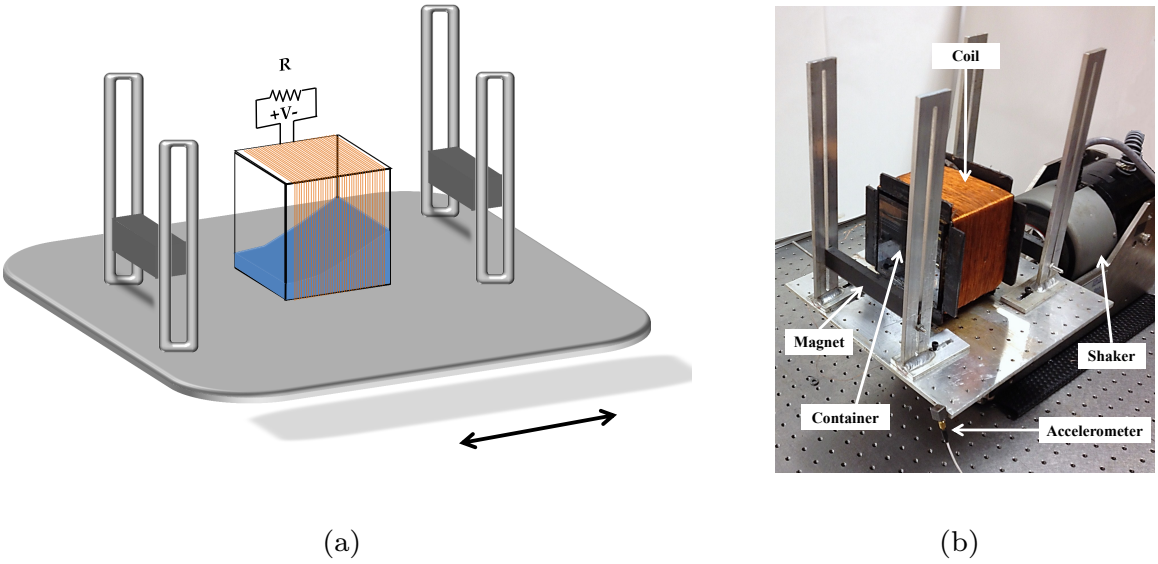

(a) (b)

Figure 2.2: (a) Schematic and (b) picture of the setup used in the experiments.

relatively uniform magnetic field-lines. Three winding directions are considered as shown in Figs. 2.3 (a), (b), and (c). In each scenario, the magnetic field lines are either oriented normal to sloshing, cross-sloshing, or parallel to sloshing, as denoted by the numbers present on each of the figures.

A quick comparison among Figs. 2.3 (a), (b), and (c) illustrates that, when the winding direction is parallel to the sloshing direction, the output voltage is almost double that obtained in the other two scenarios regardless of the magnetic field direction. This can be attributed to the fact that, in this scenario, the magnetized dipoles can cover a larger area as they move at a relatively higher speed with respect to the coil. This increases the change in magnetic flux which induces a higher current in the coil.

Additionally, it can be observed that, highest output voltage per unit acceleration is obtained when the magnetic field lines are parallel to the sloshing direction. This stems from the fact that, when the magnetic field lines are perpendicular to the sloshing direction, the magnetic dipoles align themselves perpendicular to the sloshing motion, forming string-like shapes parallel to the magnetic field lines, i.e., perpendicular to the sloshing direction. This increases the resistance of the fluid to move, thereby reducing its velocity and increasing its viscosity. This is also evident by the overdamped voltage response in that scenario. As such, it can be concluded that the best

performance is realized when the magnetic field lines and the windings are parallel to the direction of the sloshing motion.

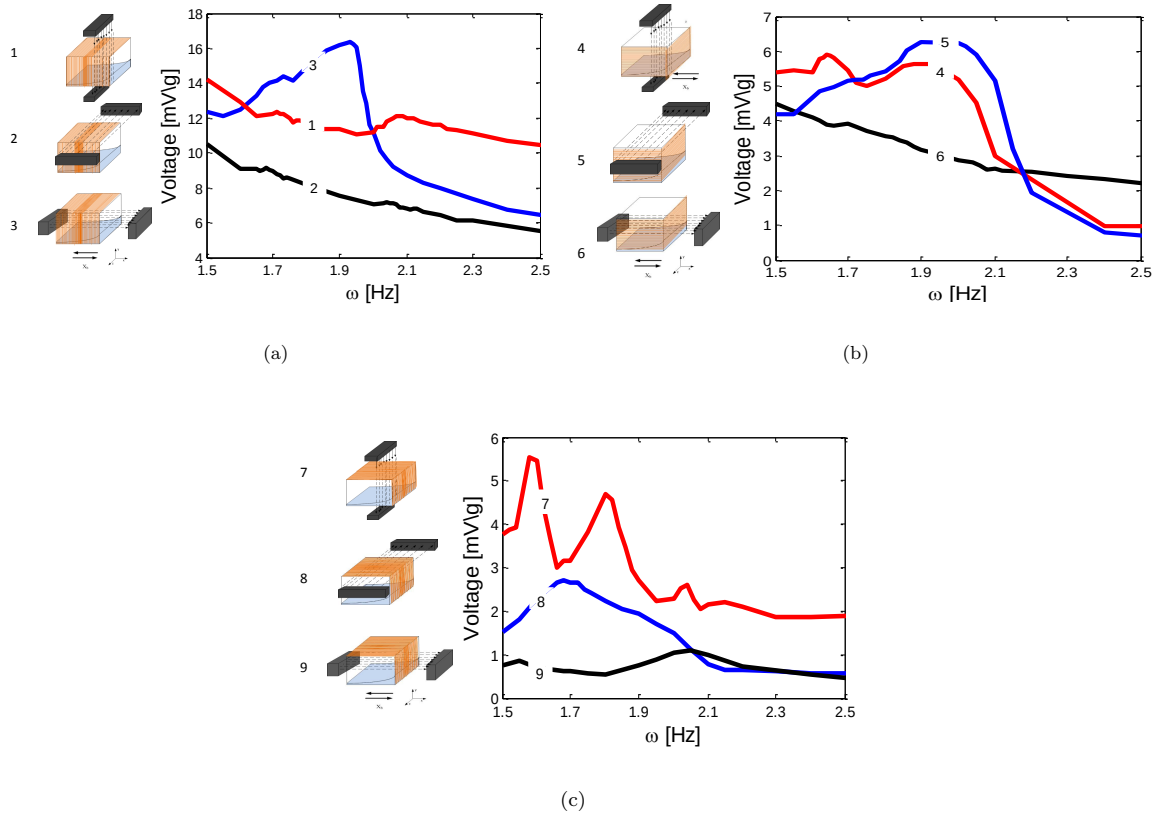

Figure 2.3: Frequency response curves of the output voltage for different magnetization and winding directions. Results are obtained at a fixed base acceleration of 0.5 g and an equivalent load of $R = 254$ Ohms.

2.3 Experimental Analysis

In this section, we study the response of the harvester in its optimal configuration to a harmonic excitation applied at its base. The magnetic field is adjusted by changing the distance between the permanent magnet and the center line of the container. Figure 2.4 illustrates variation of the magnetic field at the center line of the container measured as a function of the distance from the center of the magnet.

We start by placing the magnets at a distance of 4 cm from the side walls of the container. The base acceleration is set to $a_b = 0.3$ m/sec^2, and the excitation frequency is varied quasi-statically

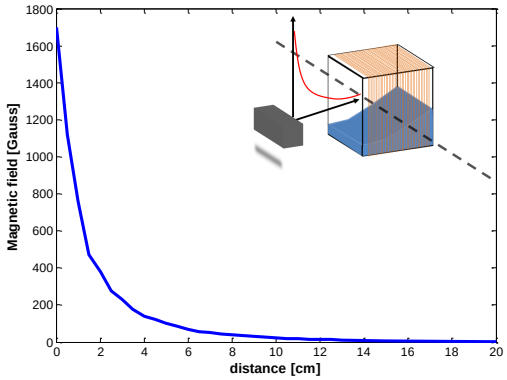

Figure 2.4: Variation of the magnetic field with the distance from the center of the magnet.

around the first modal frequency of the fluid column. In the absence of the external magnetic field, the modal frequencies of the two-dimensional sloshing motion can be approximated via [37]

$$\omega_n^2 = gk_n \tanh(\frac{n\pi h}{L}), \tag{2.3}$$

where h is the fluid height, g is the gravitational acceleration, L is the width of the container, and n represents the n^{th} sloshing mode. In the presence of the magnetic field, the apparent gravitational acceleration increases and all modal frequencies increase slightly.

Figure 2.5 depicts the voltage-frequency response curve for a liquid height, $h = 20$ mm. There are two peaks in the voltage-response curve. The first peak occurs near 1.8 Hz, while the second, which produces the higher peak voltage, occurs near 2.05 Hz. When inspecting Fig. 2.6, it can be correctly surmised that the second peak corresponds to the first modal frequency, ω_1. The first peak, on the other hand, does not correspond to any of the modal frequencies of the fluid column. In fact this peak occurs near half the second modal frequency, ω_2 and appears as a result of an internal resonance between the first sloshing mode, ω_1, and that corresponding to the second modal frequency, ω_2. Such resonances can occur when two or more modal frequencies of a certain nonlinear system are nearly commensurate, i.e., multiple integers of each other ($\omega_2 \approx 2\omega_1$), and lead to nonlinear modal interactions wherein energy is exchanged among the commensurate modes resulting in large-amplitude responses over a wide range of frequencies [38]. As shown in Fig. 2.5 (a), this has the influence of broadening the steady-state voltage-frequency response curves, further enhancing the broadband characteristics of this ferrofluid based harvester.

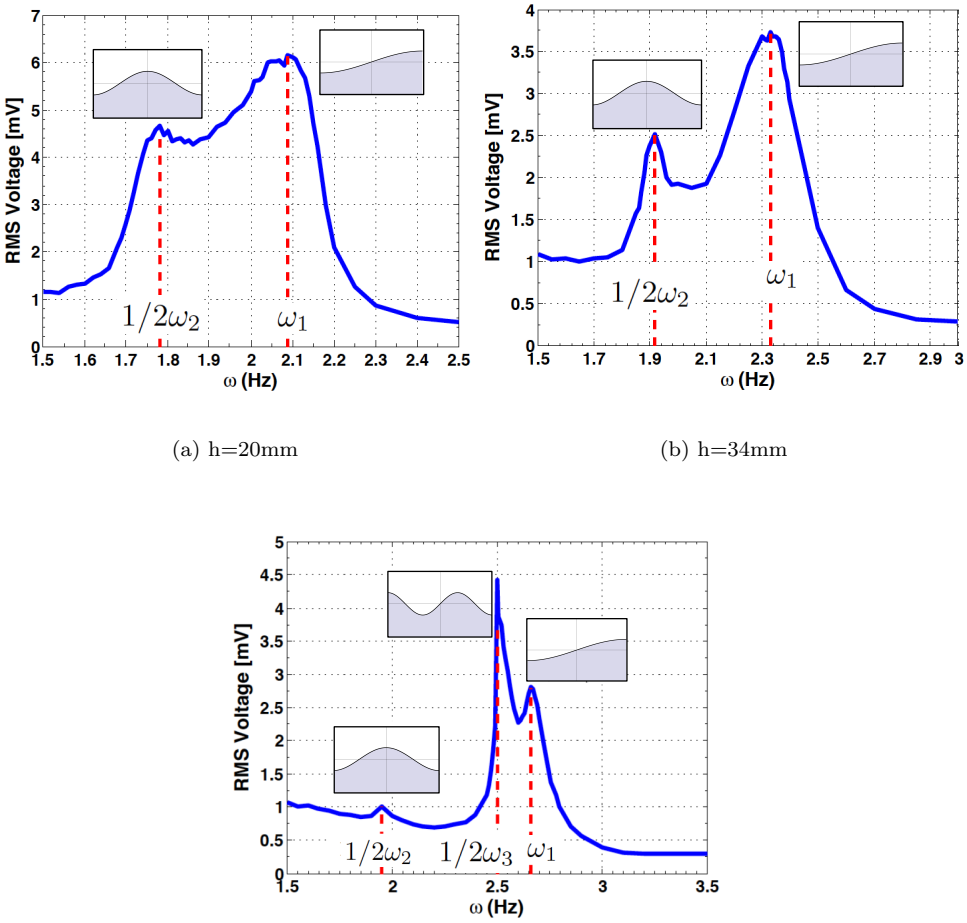

(a) h=20mm

(b) h=34mm

(c) h=50 mm

Figure 2.5: Frequency response of the voltage output for different liquid height. Results are obtained at a fixed base acceleration of 0.3 g under an equivalent load, $R = 254$ Ohms.

To further confirm that an internal nonlinear energy pump has infact been activated, the Fast Fourier Transform (FFT) of the time history is generated for different excitation frequencies. Typically, unless a nonlinear energy transfer mechanism is activated, most of the response energy is trapped at the excitation frequency. This can be clearly observed in the FFT shown in Fig. 2.7 which was obtained away from the internal resonance, specifically, for an excitation frequency of 1.5 Hz. Clearly, the FFT shows a large peak at the excitation frequency. However, when the excitation frequency is increased towards the internal resonance region, i.e., 1.78 Hz, most of the energy is pumped to twice the excitation frequency due to a two-to-one internal resonance between

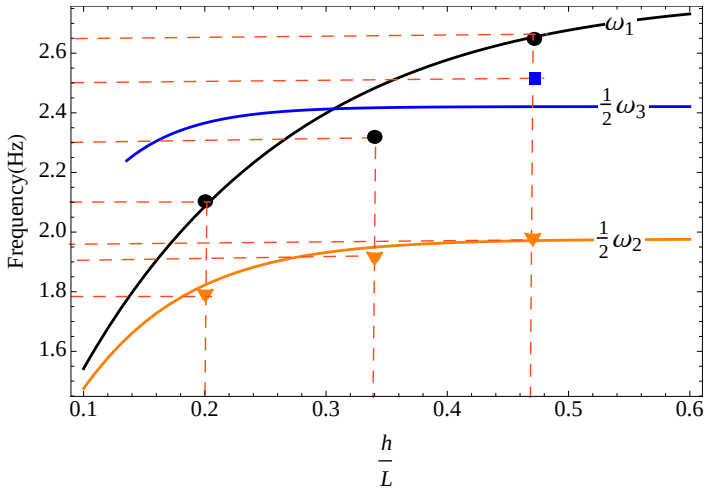

Figure 2.6: Variation of the modal frequencies of the fluid column with h/L. Asterisks represent experimental data. Circles for ω_1, square for $\frac{1}{2}\omega_3$, and triangles for $\frac{1}{2}\omega_2$

.

the nearly commensurate modes. As such, a large peak now appears in the FFT near 3.56 Hz. As the excitation frequency is increased further to 2.5 Hz, the efficacy of the energy pump decreases and only a smaller portion of the energy appears near 5 Hz.

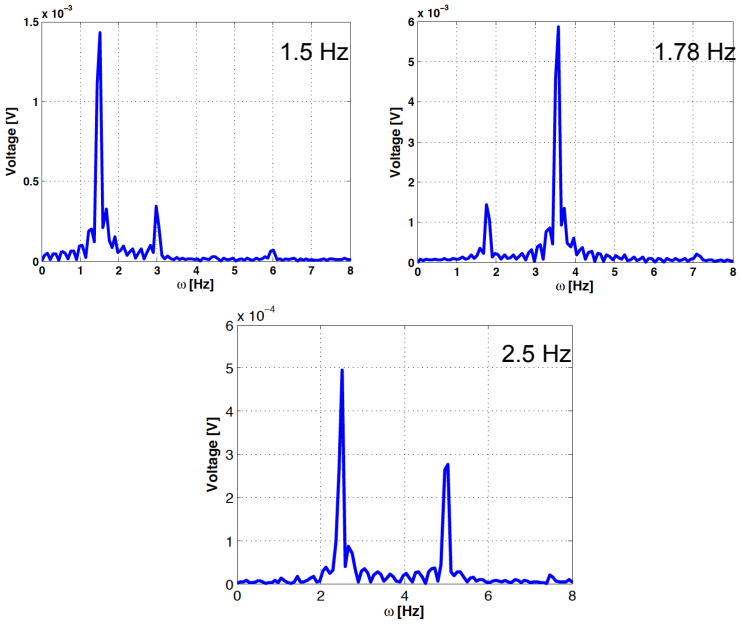

Figure 2.7: Fast Fourier Transform of the signal obtained at different excitation frequencies.

As the liquid height is increased to $h = 34$ mm, the influence of the internal energy pump

associated with the two nearly-commensurate sloshing modes, i.e. ω_2 and ω_1 can still be seen and the two response peaks are now more prevalent. However, on average, the output voltage decreases when compared to the previous case. This is because each liquid height has its own optimal magnetic field strength, whereas, in these experimental runs, we used the same magnetic field distribution for all liquid heights.

As the height is increased further to $h = 50$ mm, the peak voltage remains almost the same but a third voltage peak appears in the response. The lowest peak, which occurs near $\frac{1}{2}\omega_2$, results from the nonlinear energy exchange between ω_2 and ω_1. The amplitude of this peak is now very small because ω_2 shifted further away from ω_1, thereby reducing the effectiveness of the energy pump. The third peak now corresponds to ω_1 while the second peak corresponds to the two-mode response resulting from the energy exchange between the first mode and that corresponding to the third mode, ω_3.

Next, we study the influence of the magnetic field strength on the output voltage. Figure 2.8 depicts the voltage frequency-response curves for eight different magnet placements. The 0 cm case represents the magnets being placed right at the container sidewalls while the 10 cm represents the case where the magnets are placed furthest from the walls. We note the presence of an optimal magnetic field strength corresponding to the 2 cm distance where, on average, the output voltage is maximized. Below this distance the magnetic field becomes too strong restricting the bulk motion of the fluid in the container as well as the individual dipole rotation which, in turn, decreases the output voltage. Increasing the magnetic field also increases the viscosity of the fluid which serves to increase the effective damping in the system.

Beyond the 2 cm distance, the magnetic field becomes too weak to magnetize all the suspended dipoles in the fluid. As such, the net flux and its variation become too small to induce enough current in the coil causing the voltage to drop. It is worth reiterating that the optimal magnetic field changes depending on the height of the fluid column in the container.

The influence of the base acceleration on the output voltage is depicted in Fig. 2.9 for h =20 mm. Quiet interestingly, the peak resulting from the modal interaction, or the two-mode solution, starts to vanish as the base acceleration is increased and merges completely with the original peak at a base acceleration of $1g$ m/s^2. This is not typical of the frequency response of systems undergoing a two-to-one internal resonance since the peaks usually increase in size and become more prevalent as the forcing level increases. We theorize that, at higher acceleration levels, the surface waves become

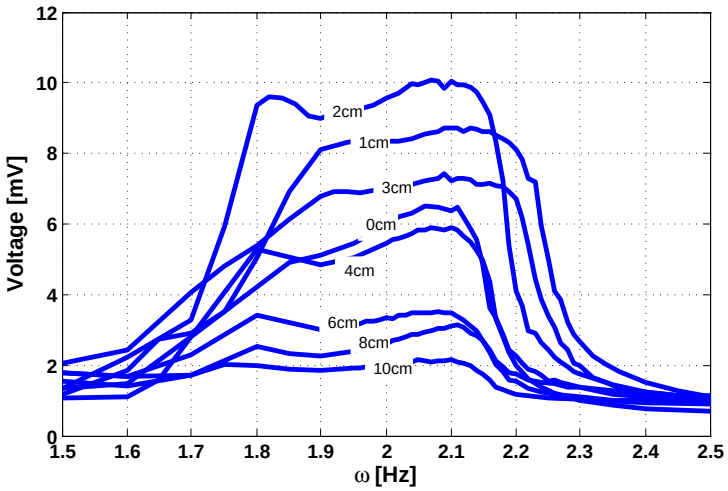

Figure 2.8: RMS voltage output for different magnetic fields. Results are obtained at a fixed base acceleration of 0.3 g m/s^2, a fluid column height, $h = 20$ mm, and for an equivalent load, $R = 254$ Ohms

too large and the magneto-hydro-electro-mechanical dynamics becomes more complex and cannot be captured by the simplified two-mode understanding discussed here.

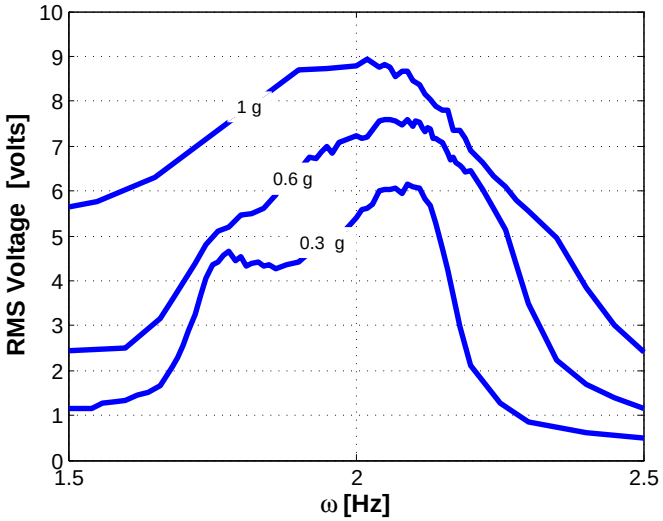

Figure 2.9: Variation of the output voltage with the frequency at different base accelerations. Results are obtained for $h = 20$ mm and an equivalent load, $R = 254$ Ohms.

Finally, we investigate the output power and optimal load of the device. To that end, the power resistance curve is generated for a 2.2 Hz excitation frequency. Similar to other electromag-

netic energy harvesters, the power increases initially and exhibits a peak at an optimal load of approximately 210 Ohms at which the device produces 80 mW per g. Typically, when neglecting the inductance of the coil, the optimal load can be obtained using impedance matching, i.e., when the resistance of the coil is equal to the resistance of the load. In this study, the resistance of the coil was measured at 250 Ohms which is quite close to the optimal load.

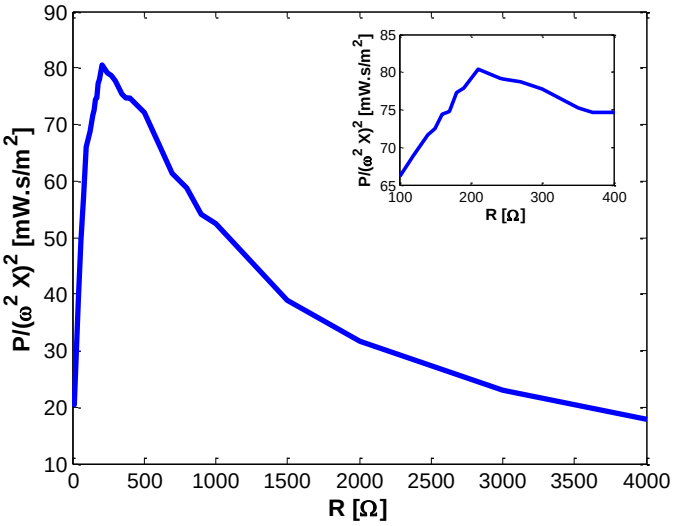

Figure 2.10: Variation of the output power with the load resistance. Results are obtained for $h = 20mm$, an excitation frequency of 2.2 Hz, and a fixed base acceleration of $0.3g$.

Chapter 3

Response to Direct Primary Resonance Excitations

This chapter formulates an analytical model which describes the electro-magneto-hydrodynamics of the system (Section 3.1). The model is able to capture, with reasonable accuracy, *i*) the magneto-hydrodynamic behavior which deals with the motion of the magnetized fluid in the container, and *ii*) the electromagnetic induction which deals with characterizing how the fluid motion is induced into electrical energy. The harvester is made of a rectangular container with specific dimensions and fluid heights that make the modal frequencies of the fluid column nearly commensurate. This serves to activate a nonlinear energy transfer mechanism between the commensurate modes further improving the steady-state bandwidth of the harvester. By linearizing the dynamics assuming small surface waves, we investigate variation of the modal frequencies with the height-to-width ratio and identify the regions where internal resonances can be activated (Section 3.2). Using the method of multiple scales, we obtain an approximate analytical solution of the harvester's response to a primary resonance excitation of the first mode (Section 3.3). We use the resulting solution to study the displacement and voltage responses of the harvester at different fluid heights (Section 3.4), and (Section 3.5), respectively. We construct an experimental set up and use it to validate the resulting model (Section 3.6).

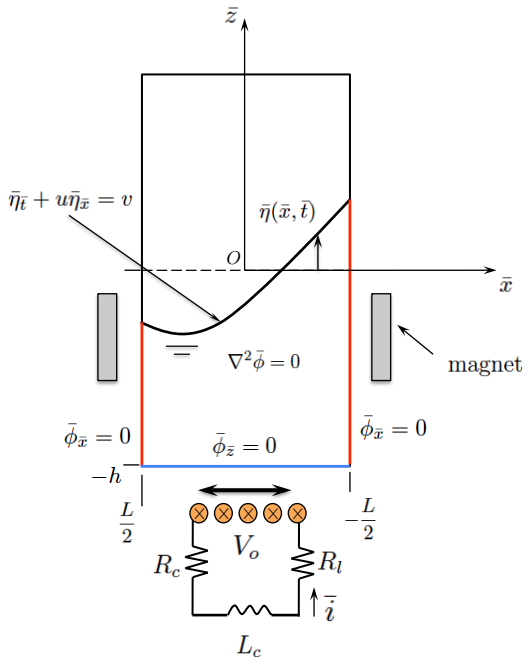

Figure 3.1: A schematic of the fluid sloshing in a rectangular container

3.1 Mathematical Modeling

We consider the two-dimensional finite-amplitude sloshing dynamics of an irrotational, incompressible ferrofluid in a rectangular container of width L. The ferrofluid whose density is denoted by ρ is assumed to be of height h. Our goal is to characterize the dependence of the output voltage of the harvester on the design parameters. To this end, we consider the system shown in Fig. 3.1 with a rotating coordinate $(\bar{x},\bar{z})$ located at point O. As the fluid starts to move due to external perturbations, surface waves of height, $\bar{\eta}(\bar{x},\bar{t})$, arise. The equations and associated boundary conditions governing the two-dimensional motion of the ferrofluid can be written as:

$$\mathbf{u}(\bar{x},\bar{z},\bar{t}) = u\mathbf{i} + v\mathbf{j} = \nabla\bar{\phi}, \tag{3.1a}$$

$$\nabla^2\bar{\phi} = 0, \qquad -\frac{L}{2} \le \bar{x} \le \frac{L}{2}, \qquad -h \le \bar{z} \le \bar{\eta}(\bar{x},\bar{t}), \tag{3.1b}$$

$$\bar{\phi}_{\bar{x}} = 0 \quad \text{on} \quad \bar{x} = \pm\frac{L}{2}, \qquad \bar{\phi}_{\bar{z}} = 0 \quad \text{on} \quad \bar{z} = -h, \tag{3.1c}$$

$$\bar{\eta}_{\bar{t}} + u\bar{\eta}_{\bar{x}} = v, \quad \text{on} \quad \bar{z} = \bar{\eta}(\bar{x}, \bar{t}), \tag{3.1d}$$

$$\bar{\phi}_{\bar{t}} + \frac{u^2 + v^2}{2} + g\bar{\eta} - \frac{\sigma}{\rho}\frac{\bar{\eta}_{\bar{x}\bar{x}}}{[1 + \bar{\eta}_{\bar{x}}^2]^{3/2}} - \bar{x}X_0\omega^2\sin(\omega\bar{t}) - \frac{\mu_0}{\rho}\int_0^{\bar{H}} \bar{M}d\bar{H} = \bar{C}. \quad \text{on} \quad \bar{z} = \bar{\eta}(\bar{x}, \bar{t}), \tag{3.1e}$$

Here, the subscripts denote partial derivatives with respect to the independent variables. Equation (3.1) (a) states the irrationality of the velocity field by expressing the two-dimensional velocity field, $\mathbf{u}$, as the gradient of a scalar potential, $\bar{\phi}$. Equation (3.1) (b) is a consequence of the incompressibility assumption for which the continuity equation requires the Laplacian of the velocity potential to vanish. Equation (3.1) (c) states that the velocity normal to the sidewalls and bottom wall vanishes. Equation (3.1) (d) is the kinematic boundary condition at the surface which states that the velocity of a fluid particle on the surface must be equal to the velocity of the surface itself. Finally, Equation (3.1) (e) represents the dynamic boundary condition at the surface obtained by enforcing the unsteady Bernoulli equation.

In Equation (3.1)(e), the first term accounts for the unsteadiness in the velocity field; the second term represents the kinetic energy of the fluid; the third term accounts for the potential energy; the fourth term represents the force due to surface tension where σ represents the surface tension coefficient; and the fifth term represents forces exerted on the surface due to a harmonic base acceleration in the $\bar{x}$ direction. Here, X_0 and ω are the amplitude and frequency of excitation, respectively. Finally, the sixth term represents the magnetic moment exerted on the surface, where $\bar{M}$ and $\bar{H}$ are the magnetization and magnetic field, respectively; μ_0 represents the permeability of vacuum, and $\bar{C}$ is a constant.

It is worth mentioning that, since the influence of surface tension on the nonlinear sloshing waves is considered, a contact angle should be enforced at the sidewalls. However, it has been shown that, unless the contact angle is significantly different from 90°, i.e., horizontal surface, the contact angle has a very little influence on the dynamics of the surface. As such, to facilitate the analytical

analysis, it is assumed that the contact angle is 90° and that the contact line is free to slip on the container's surface.

In this study, the applied magnetic field will be static and will vary along the $\bar{x}$-axis only, i.e., $\bar{H}(\bar{x},\bar{y},\bar{z},\bar{t}) = \bar{H}(\bar{x})$. The magnetic field is assumed to have a linear relationship with the magnetization, $\bar{M}(\bar{x}) = \chi_m \bar{H}(\bar{x})$, that is,

$$\int_0^{\bar{H}} \bar{M}(\bar{x}) d\bar{H} = \frac{\chi_m}{2} \bar{H}^2(\bar{x}). \tag{3.2}$$

Equation (4.1) can be further non-dimensionalized by introducing the following dimensionless quantities:

$$\begin{aligned} &x = \frac{\bar{x}}{L}, \qquad z = \frac{\bar{z}}{L}, \qquad \eta = \frac{\bar{\eta}}{L} \qquad t = \omega_0 \bar{t}, \qquad \phi = \frac{\bar{\phi}}{L^2 \omega_0}, \qquad \bar{C} = \frac{C}{L^2 \omega_0^2}, \\ &x_0 = \frac{X_0}{L}, \qquad \Omega = \frac{\omega}{\omega_0}, \qquad H = \frac{\bar{H}}{H_0}, \end{aligned} \tag{3.3}$$

where $\omega_0 = \sqrt{\frac{\pi g}{L}\delta_1}$ is the first modal frequency of the fluid column in the absence of surface tension and magnetic field, $\delta_1 = \tanh(\pi h/L)$, and $H_0 = L\omega_0\sqrt{\frac{2\rho}{\mu_0}}$. This yields the following non-dimensional equations:

$$\nabla^2 \phi = 0, \qquad -\frac{1}{2} \le x \le \frac{1}{2}, \qquad -h/L \le z \le \eta(x,t), \tag{3.4a}$$

$$\phi_x = 0 \quad \text{on} \quad x = \pm\frac{1}{2}, \qquad \phi_z = 0 \quad \text{on} \quad z = -h/L, \tag{3.4b}$$

$$\eta_t + \phi_x \eta_x = \phi_z, \quad \text{on} \quad z = \eta(x,t), \tag{3.4c}$$

$$\phi_t + \frac{\phi_x^2 + \phi_z^2}{2} + \frac{1}{\pi\delta_1}\eta - \frac{\beta}{\pi\delta_1}\frac{\eta_{xx}}{[1+\eta_x^2]^{3/2}} - x x_0 \Omega^2 \sin\Omega t - \chi_m H^2 = C \quad \text{on } z = \eta(x,t), \tag{3.4d}$$

where $\beta = \sigma/(\rho g L^2)$, also known as the inverse of the bond number, is the ratio between surface tension and gravitational forces.

3.2 Modal Frequencies

Since maximum energy transfer from the base excitation to the fluid occurs near one of the modal frequencies of the fluid column, it is important to characterize variation of the modal frequencies with the design parameters. To this end, we obtain the modal frequencies of the response by solving the linear unforced eigenvalue problem. This is achieved by linearizing Equations (3.4) (c,d) about $\eta(x,t) = 0$ to obtain

$$\phi_t + \frac{1}{\pi\delta_1}(\eta - \beta\eta_{xx}) + \chi_m H^2(x) = 0, \tag{3.5a}$$

$$\eta_t - \phi_z = 0, \tag{3.5b}$$

Differentiating Equation (3.5a) once with respect to time and substituting Equation (3.5b) in the resulting equation yields

$$\phi_{tt} + \frac{1}{\pi\delta_1}(\phi_z + \beta\phi_{zzz}) = 0, \tag{3.6}$$

Note that influence of the magnetic field disappears since it is time invariant and applied only along the x-axis. Equation (3.6) in conjunction with Equation (3.4(b) admit a solution of the form

$$\begin{aligned}\phi(x,y,z,t) = &\sum_{k=1,odd}^{\infty} a_k \sin k\pi x \frac{\cosh k\pi(z+h/L)}{\cosh k\pi(h/L)} e^{i\omega_k t} \\ &+ \sum_{k=2,even}^{\infty} a_k \cos k\pi x \frac{\cosh k\pi(z+h/L)}{\cosh k\pi(h/L)} e^{i\omega_k t} + cc\end{aligned} \tag{3.7a}$$

$$\eta(x,t) = \sum_{k=1,odd}^{\infty} b_k \sin k\pi x e^{i\omega_k t} + \sum_{k=2,even}^{\infty} b_k \cos k\pi x e^{i\omega_k t} + cc, \tag{3.7b}$$

where $\omega_k = \sqrt{\frac{\delta_k}{\pi\delta_1}(\beta k^3\pi^3 + k\pi)}$ are the modal frequencies of the odd (k odd) and even (k even) sloshing modes, respectively, cc represents the complex conjugates of the preceding terms, and $\delta_k = \tanh(k\pi h/L)$.

Figure 3.2 depicts variation of the first five modal frequencies with the liquid height-to-width ratio, h/L. To generate this figure a container of width $L = 10$ cm is considered assuming a ferrofluid which has a surface tension coefficient, $\sigma = 0.03N/m$, and density $\rho = 1420kg/m^3$. It is evident

that the modal frequencies are closely-spaced in the parameters space. As such, the bandwidth of frequencies where the harvester cannot respond to the external excitation is very narrow resulting in wideband behavior.

In addition to illustrating the loci of the modal frequencies in the h/L space, the figure also depicts variation of some multiple integers of the lowest three modal frequencies with h/L. Thus, these diagrams allow us to find the values of h/L for which the modal frequencies are commensurate. In the vicinity of these points, the sloshing conditions are such that nonlinear interactions among the modes possessing commensurate frequencies can be activated resulting in energy exchange. Consequently, when the n^{th} mode is directly excited via a primary resonance and that mode is in internal resonance with another mode, say the m^{th}, the response will exhibit contributions from both modes even when the m^{th} mode is not directly excited.

Figure 3.2 illustrates that nonlinear modal interactions are possible at several values of h/L. For instance, when $h/L \approx 0.02$; $\omega_2 = 2\omega_1$, $\omega_3 = 3\omega_1$, and $\omega_4 = 2\omega_2$. Furthermore, when $h/L \approx 0.14$, $\omega_4 = 3\omega_1$, and when $h/L \approx 0.2$, $\omega_5 = 3\omega_1$. It is worth noting however that, such conditions are necessary but not sufficient; that is, two modes can be commensurate but not interacting. For instance, we have shown previously in [39] that, internal resonances of the two-to-one type can only occur when $\omega_m \approx 2\omega_n$ and $m = 2n$. In other words, even when the condition $\omega_3 = 2\omega_1$ is satisfied when $h/L \approx 0.32$, it does lead to a two-to-one internal resonance between the first and third modes.

3.3 Nonlinear Response

Equation (3.4) (a) subject to the static boundary conditions admits a general solution of the form:

$$\begin{aligned}\phi(x,y,z,t) = a_0(t) + \sum_{k=1,odd}^{\infty} a_k(t) \sin k\pi x \frac{\cosh k\pi(z+h/L)}{\cosh k\pi(h/L)} \\ + \sum_{k=2,even}^{\infty} a_k(t) \cos k\pi x \frac{\cosh k\pi(z+h/L)}{\cosh k\pi(h/L)},\end{aligned} \tag{3.8a}$$

$$\eta(x,t) = \sum_{k=1,odd}^{\infty} b_k(t) \sin k\pi x + \sum_{k=2,even}^{\infty} b_k(t) \cos k\pi x, \tag{3.8b}$$

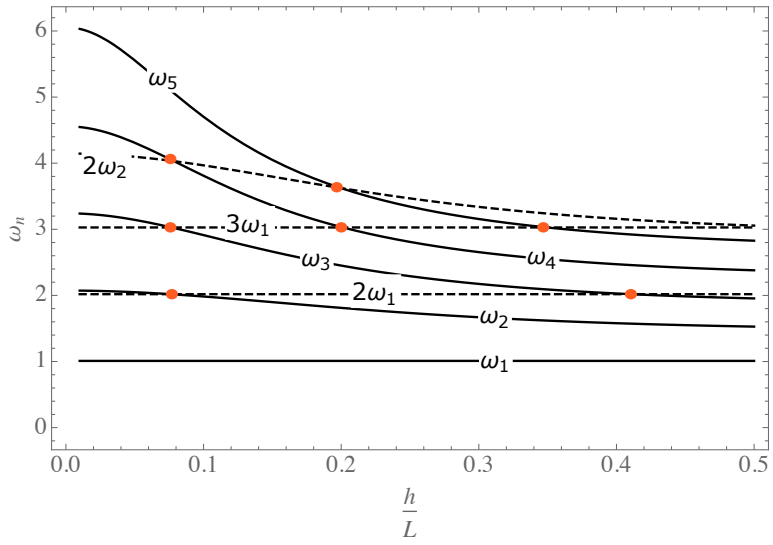

Figure 3.2: Variation of the sloshing modal frequencies with the height to length ratio, h/L for $\beta = 2.25 \times 10^{-4}$.

where $a_0(t)$, $a_k(t)$, $b_k(t)$, $b_m(t)$, are unknown functions of time that can be determined by enforcing the kinematic and dynamic boundary conditions at the surface, i.e., Equations (3.4) (c) and (d).

Since Equations (3.4) (c) and (d) are nonlinear due to the advection term $\phi_x \eta_x$ in Equation (3.4) (d) as well as the kinetic energy and surface tension terms in Equation (3.4) (e), an exact solution cannot be easily found. To overcome this issue, an approximate analytical solution of the equations is obtained using the method of multiple scales [40]. To this end, the time dependence in the equation is expanded into multiple time scales in the form

$$T_k = \varepsilon^k t, \qquad k = 0, 1, 2 \ldots \tag{3.9}$$

where ε is a bookkeeping parameter. Based on the definition of the new time scales, the time derivatives can be expressed as

$$\frac{d}{dt} = D_0 + \varepsilon D_1 + \varepsilon^2 D_2 + O(\varepsilon^3), \tag{3.10}$$

where $D_k = \frac{\partial}{\partial T_k}$.

The dependent variables ϕ, and η, as well as the unknown constant, C are also expanded in

the following forms:

$$\begin{aligned}\phi(x,z,t,\varepsilon) &= \varepsilon\phi_1(x,z,T_0,T_1,T_2) + \varepsilon^2\phi_2(x,z,T_0,T_1,T_2) + O(\varepsilon^3)\\ \eta(x,t,\varepsilon) &= \varepsilon\eta_1(x,T_0,T_1,T_2) + \varepsilon^2\eta_2(x,T_0,T_1,T_2) + O(\varepsilon^3),\\ C &= \varepsilon^2 C_2 + O(\varepsilon^3).\end{aligned} \tag{3.11}$$

To implement the method of multiple scales, the base acceleration and magnetization are scaled to appear at the same order of the perturbation problem such that $x_0 = \varepsilon^2 x_0$, and $\chi_m = \varepsilon^2\chi_m$. Furthermore, the frequency of acceleration, Ω, is assumed to be close to the fundamental frequency $\Omega = \omega_1 + \epsilon\sigma_1$, where σ_1 is a small frequency detuning parameter. Since the dynamic and kinematic boundary conditions are evaluated at the surface $\eta(x,t)$, which is still unknown, the dependence of ϕ on η is expanded in a Taylor series around $\eta = 0$. In other words, we let $\phi(\eta) \approx \phi(0) + \varepsilon\phi_z(0)\eta + \varepsilon^2/2\phi_{zz}(0)\eta^2 + O(\varepsilon^3)$. Note that this assumption is accurate as long as the surface waves are finite but sufficiently small.

Upon substituting Equations (3.9-3.11) into Equation (3.4) (c) and (d), and collecting terms of like powers of ε, we obtain the following cascade of linear partial differential equations:

$O(\varepsilon^1)$:

$$D_0\phi_1 + \frac{1}{\pi\delta_1}(\eta_1 - \beta\eta_{1xx}) = 0, \tag{3.12a}$$

$$D_0\eta_1 - \phi_{1z} = 0, \tag{3.12b}$$

$O(\varepsilon^2)$:

$$\begin{aligned}D_0\phi_2 + \frac{1}{\pi\delta_1}(\eta_2 - \beta\eta_{2xx}) = -\frac{1}{2}(\phi_{1z}^2 + \phi_{1x}^2) - D_1\phi_1 + \eta_1 D_0\phi_{1x}\\ +\chi_m H(x)^2 C_2 + x_0\Omega^2\sin(\Omega T_0)\end{aligned} \tag{3.13a}$$

$$D_0\eta_2 - \phi_{2z} = -D_1\eta_1 + \eta_1\phi_{1zz} - \eta_{1x}\phi_{1x}, \tag{3.13b}$$

In this chapter, we investigate the response behavior when that first mode is in a two-to-one internal resonance with the second mode. According to Fig. 3.2, a wide range of h/L values may lead to

such a condition. In such a case, the solution of Equation (4.8a) and (4.8b) can be expressed in the form

$$\phi_1 = \frac{1}{\pi\delta_1}\left(A_1(T_1,T_2)e^{i\omega_1 T_0}\mathrm{S}_1(x)\mathrm{Ch}_1(z) + A_2(T_1,T_2)e^{i\omega_2 T_0}\mathrm{C}_2(x)\mathrm{Ch}_2(z)\right) + cc, \tag{3.14a}$$

$$\eta_1 = \int \phi_{1z}(x,0,T_0,T_1,T_2)dT_0, \tag{3.14b}$$

where $\mathrm{C}_k(x) = \cos(k\pi x)$, $\mathrm{S}_k(x) = \sin(k\pi x)$, $\mathrm{Ch}_k(z) = \frac{\cosh k\pi(z+h/L)}{\cosh k\pi(h/L)}$, $A_k(T_1,T_2)$ is a complex-valued functions that will be obtained by enforcing the solvability conditions at the second stage of the perturbation analysis, and $\bar{A}_k(T_1,T_2)$ is its complex conjugate. Substituting Equation (3.14) into Equation (3.13a) yields

$$\begin{aligned}
&D_0^2\phi_2 + \frac{1}{\pi\delta_1}(D_0\eta_2 - \beta D_0\eta_{2xx}) = \\
&h_{11}D_1A_1\mathrm{S}_1(x)e^{i\omega_1T_0} + h_{12}D_1A_2\mathrm{C}_2(x)e^{i\omega_2T_0} + (h_{21}+h_{31}\mathrm{C}_2(x))A_1^2e^{2i\omega_1T_0} \\
&+ (h_{22}+h_{32}\mathrm{C}_4(x))A_2^2e^{2i\omega_2T_0} - (h_{112}\mathrm{S}_1(x)+h_{212}\mathrm{S}_3(x))A_1A_2e^{i(\omega_1+\omega_2)T_0} \\
&- (\bar{h}_{112}\mathrm{S}_1(x)+\bar{h}_{212}\mathrm{S}_3(x))\bar{A}_1A_2e^{i(\omega_2-\omega_1)T_0} + cc,
\end{aligned} \tag{3.15}$$

where the constants are given as

$$\begin{aligned}
h_{11} &= i\frac{2\omega_1}{\pi\delta_1}, \qquad h_{12} = i\frac{2\omega_2}{\pi\delta_1}, \qquad h_{21} = i\frac{\omega_1(1+3\delta_1^2)}{2\delta_1^2}, \qquad h_{22} = i\frac{\omega_2(2+3\delta_2^2)}{2\delta_1^2}, \\
h_{31} &= i\frac{\omega_2^2\delta_1 + (1-3\delta_1^2)\omega_1^2\delta_2}{2\delta_1^2\delta_2\omega_1} \qquad h_{32} = i\frac{-4\omega_4^2\delta_2 + \omega_2^2\delta_4(-4+5\delta_2^2)}{2\delta_4\delta_1^2\omega_2}, \\
h_{112} &= -i\frac{2\delta_2\omega_1^3(1+\delta_1^2) + 3\delta_1^2\delta_2\omega_1^2\omega_2 + 2\delta_1(1+\delta_1\delta_2)\omega_1\omega_2^2 + \delta_1^2\delta_2\omega_2^3}{2\delta_1^3\omega_1\omega_2}, \\
\bar{h}_{112} &= -i\frac{2\delta_2\omega_1^3(1+\delta_1^2) - 3\delta_1^2\delta_2\omega_1^2\omega_2 + 2\delta_1(1+\delta_1\delta_2)\omega_1\omega_2^2 - \delta_1^2\delta_2\omega_2^3}{2\delta_1^3\omega_1\omega_2}, \\
h_{212} &= i\frac{\delta_3(\omega_1+\omega_2)(\delta_1\delta_2(2\omega_1^2+\omega_1\omega_2+\omega_2^2) - 2\omega_1\omega_2) - 2(\delta_2\omega_1+\delta_1\omega_2)\omega_3^2}{2\delta_1^2\delta_3\omega_1\omega_2}, \\
\bar{h}_{212} &= i\frac{\delta_3(\omega_1-\omega_2)(\delta_1\delta_2(2\omega_1^2+\omega_1\omega_2+\omega_2^2) + 2\omega_1\omega_2) - 2(-\delta_2\omega_1+\delta_1\omega_2)\omega_3^2}{2\delta_1^2\delta_3\omega_1\omega_2}.
\end{aligned}$$

To express the nearness of ω_2 to twice ω_1, we let $\omega_2 = 2\omega_1 + \epsilon\sigma_2$, where σ_2 is a small frequency detuning parameter. The secular terms are then eliminated by enforcing the right-hand side of Equations (3.15) to be orthogonal to the homogeneous solution, i.e., Equation (3.14), which

yields

$$D_1 A_1 - r\bar{h}o_{12}\bar{A}_1 A_2 e^{i\sigma_2 T_2} = 0, \qquad D_2 A_2 - \rho_{11} A_1^2 e^{-i\sigma_2 T_2} - \frac{x_0 \Omega^2 \delta_1}{\pi^2} e^{i\sigma_1 T_2} = 0. \tag{3.16}$$

where $\rho_{12} = -\frac{\bar{h}_{112}}{h_{11}}$, and $\rho_{11} = -\frac{h_{31}}{h_{12}}$.

3.3.1 Steady-State Response

To solve Equation (3.16), we express the unknown complex functions in the polar form $A_k = 1/2 a_k e^{i\beta_k}$, $\bar{A}_k = 1/2 a_k e^{-i\beta_k}$ and separate the real and imaginary parts to obtain

$$\dot{a}_1 = -2\mu_1 a_1 - \frac{\rho_{12}}{2} a_1 a_2 \cos\gamma_1 - F_0 \sin\gamma_2, \tag{3.17a}$$

$$a_1 \dot{\gamma}_1 = \sigma_1 a_1 + \frac{\Gamma_{12}}{2} a_1 a_2 \sin\gamma_1 + F_0 \cos\gamma_2, \tag{3.17b}$$

$$\dot{a}_2 = -2\mu_2 a_2 - \frac{\rho_{11}}{2} a_1^2 \cos\gamma_1, \tag{3.17c}$$

$$a_2(\dot{\gamma}_1 - 2\dot{\gamma}_2) = a_2(\sigma_2 - 2\sigma_1) + \frac{\Gamma_{11}}{2} a_1^2 \sin\gamma_1 \tag{3.17d}$$

where $\gamma_1 = \sigma_2 t + \beta_2 - 2\beta_1$, $\gamma_2 = \sigma_1 t - \beta_1$, $F_0 = \frac{2x_0\delta_1\Omega^2}{\pi^2}$ and μ_1, μ_2 are modal damping added to represent viscous damping effects in the fluid. These terms were obtained experimentally by fitting the linear frequency response to the experimental findings under low excitation levels.

To obtain the steady-state solutions, we set the time derivatives in Equation (4.17a) to zero and solve the resulting algebraic system of equations analytically for the steady-state amplitude, (a_{10}, a_{20}) and phase $(\gamma_{10}, \gamma_{20})$ of the two-mode response. The stability of the resulting solutions is then assessed by finding the eigenvalues associated with the Jacobian of Equation (4.17a) evaluated

at the steady-state roots. To first order, the steady-state solution can be written as

$$\begin{aligned}\phi(x,z,t) = &\frac{1}{\pi\delta_1}(a_{10}\cos(\Omega t-\gamma_{20})\mathrm{S}_1(x)\mathrm{Ch}_1(z)\\ &+a_{20}\cos(2\Omega t-2\gamma_{20}+\gamma_{20})\mathrm{C}_2(x)\mathrm{Ch}_2(z)),\\ \eta(x,t) = &\frac{1}{\Omega}\left(a_{10}\sin(\Omega t-\gamma_{20})\mathrm{S}_1(x)+a_{20}\frac{\delta_2}{\delta_1}\sin(2\Omega t-2\gamma_{20}+\gamma_{10})\mathrm{C}_2(x)\right),\end{aligned} \tag{3.18}$$

where

$$\begin{aligned}\frac{\rho_{11}^2\rho_{12}^2}{16}a_{10}^6+\frac{\rho_{11}\rho_{12}}{2}(-2\mu_1\mu_2+\sigma_1(2\sigma_1-\sigma_2))a_{10}^4+R(4\mu_1^2+\sigma_1^2)a_{10}^2-RF_0^2=0.\\ a_{20}=-\frac{\rho_{11}}{2}\frac{a_{10}^2}{\sqrt{4\mu_2^2+(\sigma_2-2\sigma_1)^2}}.\end{aligned} \tag{3.19}$$

and $R=4\mu_2^2+(\sigma_2-2\sigma_1)^2$.

3.4 Numerical Results

We use the resulting analytical solution, i.e., Equation (3.18) to study the displacement frequency response curves for two different height-to-width ratios, namely, $h/L=0.2$ and $h/L=0.3$. Figure 3.3 depicts variation of the surface wave amplitude measured at approximately 1 cm from the wall with the excitation frequency for a base acceleration of 0.3 m/s^2. When $h/L=0.2$, the frequency-response curve exhibits two distinct peaks occurring at approximately 1.7 Hz and 2.25 Hz. The first peak, associated with the lower magnitude, occurs near half the second modal frequency; whereas the second peak with the higher magnitude occurs near the fundamental frequency. While the appearance of the second peak is expected and can be attributed to the primary resonance behavior, the appearance of the first peak near half the second modal frequency of the sloshing fluid is due to the aforementioned two-to-one internal resonance between the first and second modes. Such internal resonance occurs because the second mode is nearly twice the first mode when $h/L=0.2$. This results in nonlinear energy exchange between the interacting modes.

The two-to-one internal resonance can also be confirmed by inspecting the velocity streamlines and surface profile near 1.7 Hz as depicted in Fig. 3.4. The figure, which depicts the velocity streamlines and the surface wave height during one complete cycle of oscillation, illustrates that, due to the contribution of the second mode, there is a large vertical velocity component at the midpoint

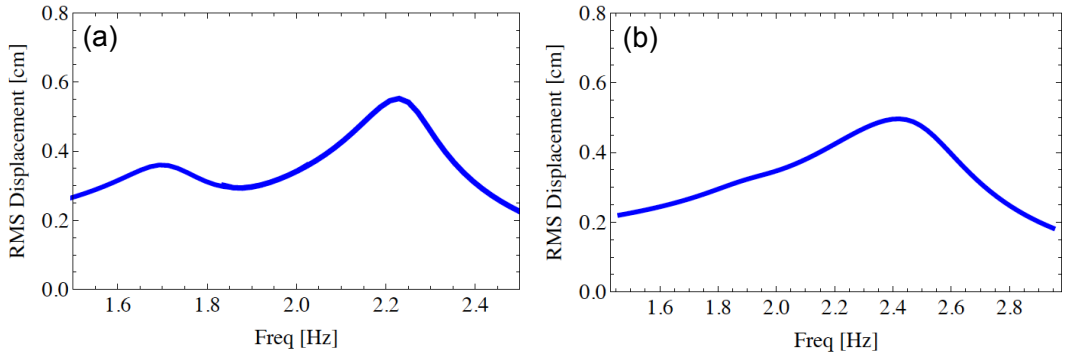

Figure 3.3: Frequency response curves under harmonic base acceleration of 0.3 m/s^2. Results are obtained for (a) $h/L = 0.2$, (b) $h/L = 0.3$, μ_1=0.04, and $\mu_2 = 0.054$.

of the surface. In the absence of the second mode contribution, the sloshing wave is such that the surface has zero velocity at the midpoint of the surface.

As shown in Fig. 3.5, when the excitation frequency is shifted towards 2.57 Hz which is slightly above the first modal frequency, the velocity streamlines, for the most part, illustrate symmetric motions around the midpoint of the surface. This is typical of the first mode response and indicates that the contribution of the second mode diminishes as the excitation frequency deviates from half the second modal frequency.

Figure 3.3 (b) depicts the frequency-response curves when $h/L = 0.3$. For this value of h/L, the nonlinear interaction is negligible since, as shown earlier in Fig. 3.2, the second modal frequency deviates significantly from twice the fundamental frequency. As a result, the frequency response only includes one dominant peak near 2.4 Hz. Due to the diminishing nonlinear interaction between the first and second modes, a barely noticeable hump can also be seen near 1.9 Hz.

3.5 Output Voltage

To obtain the voltage induced in one coil, V_o, Faraday's law is applied. For a rectangular tank, with coils wound in the vertical direction and magnetic field applied along the $\bar{x}$-axis, the voltage output per unit width of the harvester can be written

$$V_o = -\frac{d}{d\bar{t}} \iint_{\Sigma(\bar{t})} \mathbf{B}(\bar{x}) d\mathbf{A}, \tag{3.20}$$

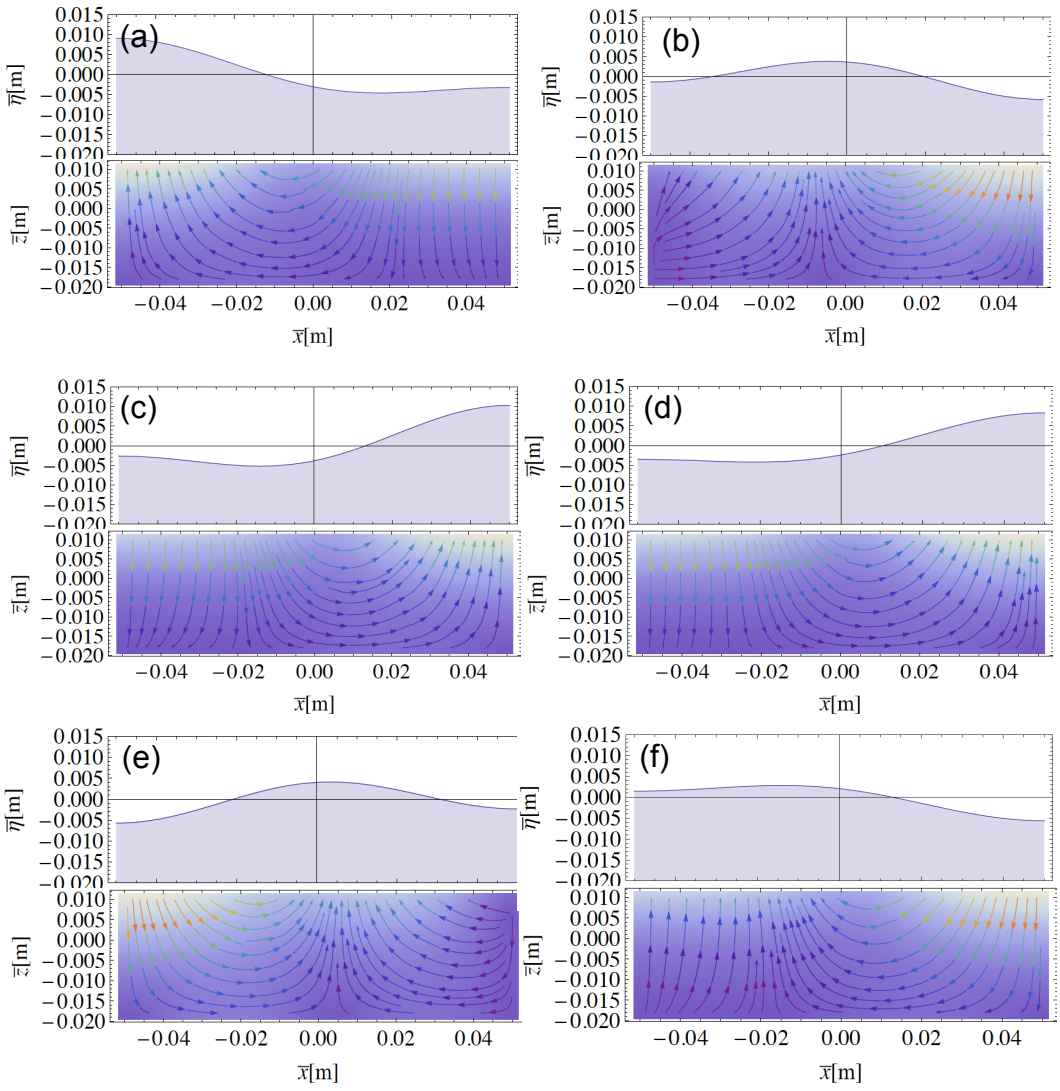

Figure 3.4: Surface wave height and velocity streamlines of the sloshing ferrofluid during one cycle of steady-state oscillation for $h/L = 0.2$, a base acceleration of 0.3 m/s^2, and an excitation frequency $\omega = 1.755$ Hz. (a) $\bar{t} = 0.073$s, (b) $\bar{t} = 2 \times 0.073$s, (c) $\bar{t} = 3 \times 0.073$s, (d) $\bar{t} = 4 \times 0.073$s, (e) $\bar{t} = 5 \times 0.073$s, and (f) $\bar{t} = 6 \times 0.073$s.

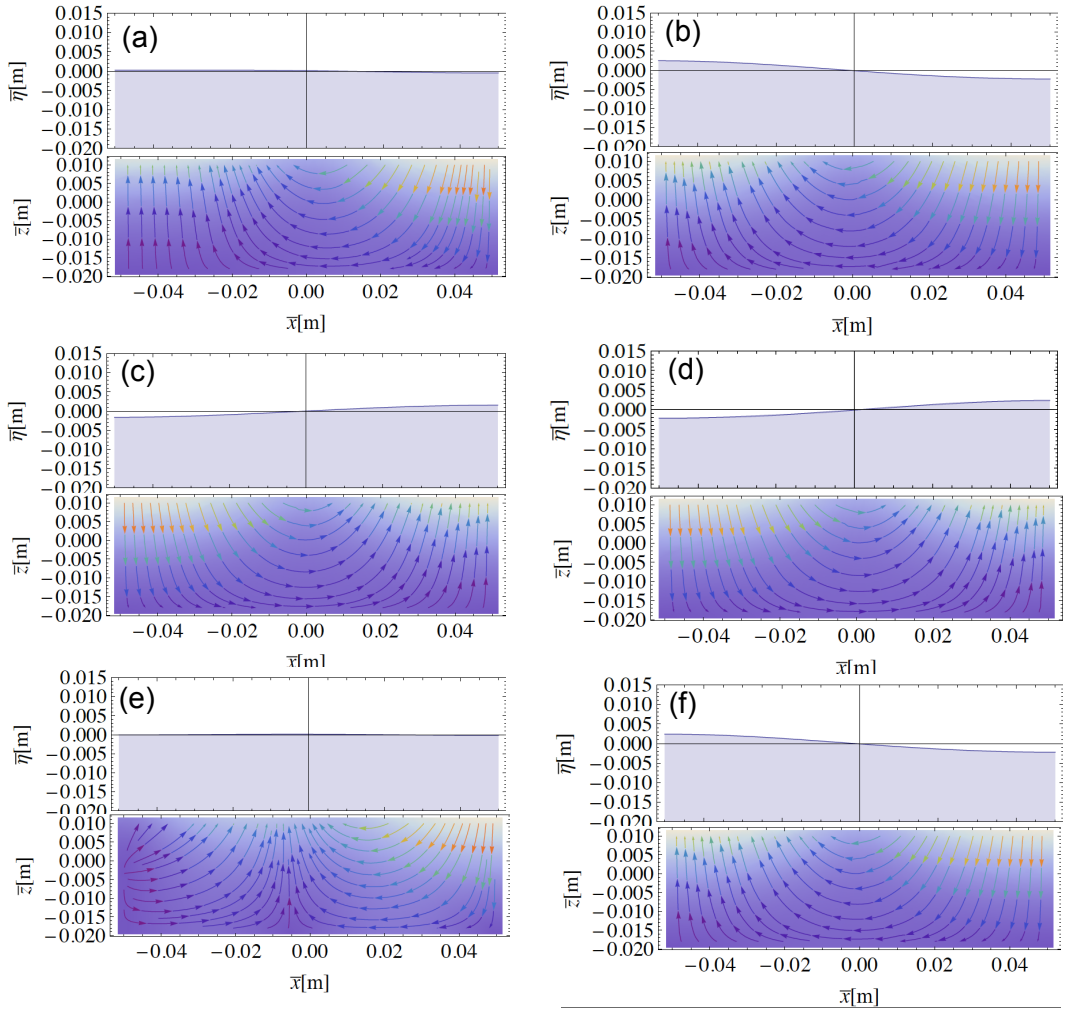

Figure 3.5: Surface wave height and velocity streamlines of the sloshing ferrofluid during one cycle of steady-state oscillation for $h/L = 0.2$, a base acceleration of 0.3 m/s^2, and an excitation frequency $\omega = 2.57$ Hz. (a) $\bar{t} = 0.073$s, (b) $\bar{t} = 2\times0.073$s, (c) $\bar{t} = 3\times0.073$s, (d) $\bar{t} = 4\times0.073$s, (e) $\bar{t} = 5\times0.073$s, and (f) $\bar{t} = 6 \times 0.073$s.

where $d\mathbf{A}$ is an element on the moving surface $\Sigma(\bar{t})$, and $\mathbf{B}$ is the vector of magnetic flux density. For the problem at hand, and assuming small surface waves, the previous equation can be written as

$$V_o = -\frac{d}{d\bar{t}} \int_{-b}^{b} \int_{-h}^{\bar{\eta}(\bar{t})} B(\bar{x}) d\bar{y} d\bar{z}, \tag{3.21}$$

where $2b$ is the depth of the container.

The magnetic flux density, B, can be further related to the applied field via $B(\bar{x}) = \mu_0(1 + \chi_m)\bar{H}(\bar{x})$, which upon substitution into Equation (3.20) and carrying out the integration yields

$$V_o = -2bh\mu_o(1 + \chi_m)\bar{H}(\bar{x})\frac{d\bar{\eta}}{d\bar{t}}. \tag{3.22}$$

To determine the average output voltage generated in the total number of coils, N, we multiply Equation (3.22) by the number of coils, N, and average the results over the width of the container, L. This yields

$$V_o = \alpha_c \int_{-L/2}^{L/2} \bar{H}(\bar{x})\frac{d\bar{\eta}}{d\bar{t}} d\bar{x}, \tag{3.23}$$

where $\alpha_c = -2Nb\frac{h}{L}\mu_o(1 + \chi_m)$.

To determine the current in the coil, we apply Kirchhoff's Law and obtain

$$L_c\frac{d\bar{i}}{d\bar{t}} + (R_c + R_l)\bar{i} = \alpha_c \int_{-L/2}^{L/2} \frac{d\bar{H}(\bar{x})}{d\bar{x}}\frac{d\bar{\phi}}{d\bar{x}} d\bar{x}, \tag{3.24}$$

where $\bar{i}$ is the induced current, R_l is the load resistance, R_c and L_c are, respectively, the resistance and inductance of the collecting coil.

3.6 Experimental Results

To investigate the validity of the theoretical model and analytical solution, the experimental setup depicted in Fig. 3.6 is constructed. A plastic cubic container carrying the ferrofluid with each side measuring at 10.16 cm is placed inside a pick-up coil. The coil is wound around a ferrite core and the whole setup is mounted on an electrodynamic shaker table. The external magnetization is applied using permanent magnets with maximum magnetic field intensity of 92 mT. The intensity and the spatial distribution of the magnetization are varied by changing the external permanent magnets placement. A dSpace system is used for the purpose of controlling the shaker and for data

acquisition. The harvested voltage is measured across a resistive load connected in parallel to the pick-up coil. The physical properties of the ferrofluid and the harvester are listed in Table 3.1.

Table 3.1: Harvester's properties and specifications.

Property	SI Units
Ferrofluid Flash Point	92°
Ferrofluid Initial Magnetic Susceptibility	3.52
Ferrofluid Viscosity at 27°	12 mPa.s
Ferrofluid Density at 25°	1420 kg/m^3
Number of Coil Turns	1500
Inductance of Coil Turns	1.55 H
Coil Resistance	254 Ohms

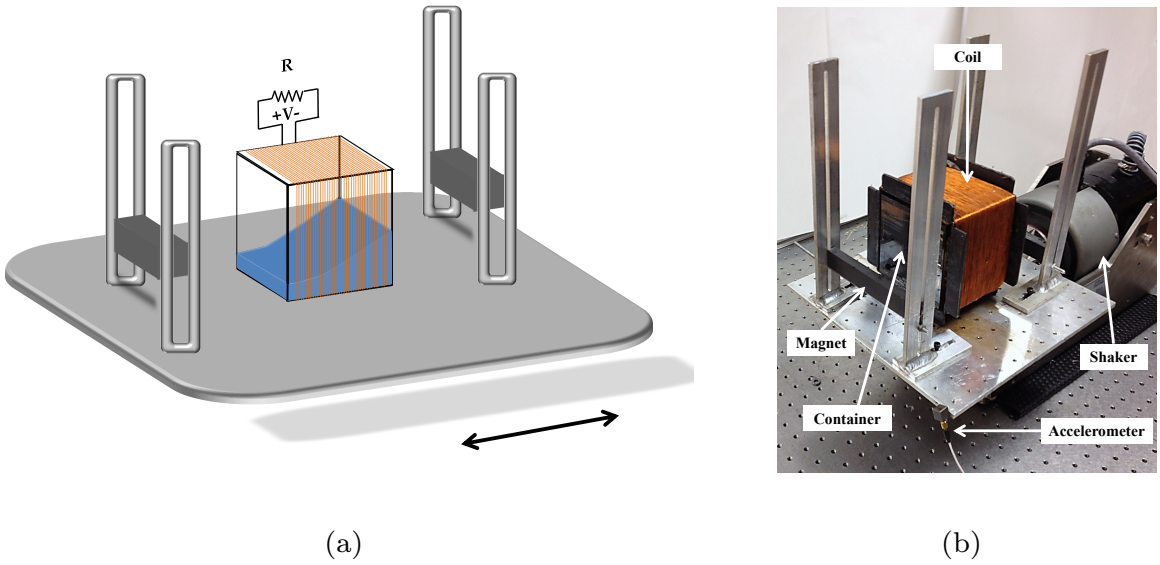

(a) (b)

Figure 3.6: (a) Schematic and (b) picture of the setup used in the experiments.

The height of the surface wave is measured at the corner of the container using a laser vibrometer. Since ferrofluids absorb the laser beam, a thin layer of superhydrophobic coating is sprayed over the ferrofluid surface. To reflect the laser beam, an additional thin layer of a high gloss yellow paint is then sprayed over the hydrophobic coating. Two cases are analyzed, namely $h/L = 0.2$, and $h/L = 0.3$. In both cases, the steady-state amplitude of the surface wave at approximately 1 cm from the wall is measured. The magnitude of the output voltage across an optimal load of 254 Ohms is also recorded under a base acceleration of 0.3 m/s^2 and a frequency

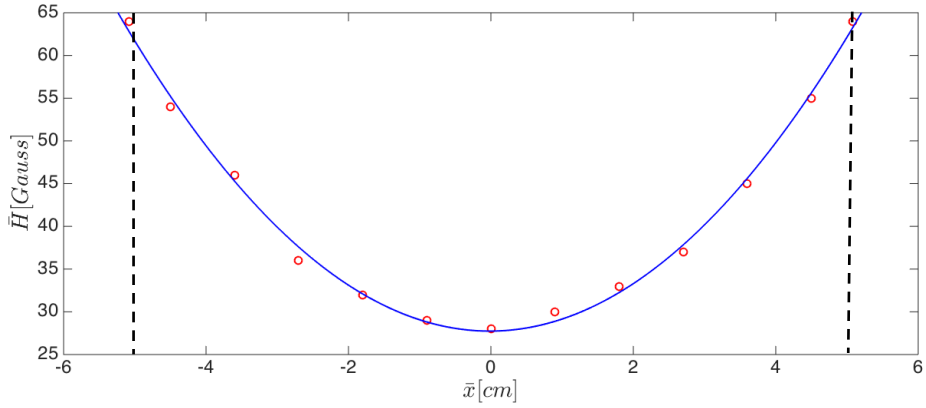

Figure 3.7: Variation of the magnetic field across the container's width.

bandwidth around the first modal frequency. In the experiment, the frequency of motion of the shaker head is varied from a value well below resonance to a value well above resonance and vise versa. At each frequency step, the steady-state is allowed to develop. The magnetic field $\bar{H}(\bar{x})$ is applied using static permanent magnets with opposite polarities placed at a small distance from the container walls. The resulting field across the container is measured using a Gaussmeter and recorded then fitted into a quadratic curve as shown in Fig. 3.7.

First, the displacement frequency response curves as obtained experimentally and using the analytical model are compared in Fig. 3.8 for (a) $h/L = 0.2$ and (b) $h/L = 0.3$. A good qualitative agreement between the model and the experiment is observed. For $h/L = 0.2$, both of the theory and experiment predict the presence of two distinct peaks in the response. However, the theoretical model over predicts the location of the larger peak associated with the first mode. This could be due to an error in the experimental measurement of the height of the fluid column due to surface tension effects.

Similarly, when $h/L = 0.3$, both of the theory and experiment agree qualitatively in predicting the presence of only one distinct peak in the frequency response. However, the theoretical results again over predict the response magnitude over most of the frequency range considered.

Next, we compare the voltage response curves in both cases as depicted in Fig. 3.9. Good qualitative agreement between the theoretical and experimental results is observed. In both cases, the theoretical results under predict the experimental findings near the first modal frequency and slightly over-predict them near half the second modal frequency. When $h/L = 0.2$ larger voltage output is produced as compared to the case involving $h/L = 0.3$. Moreover, quite interestingly, even

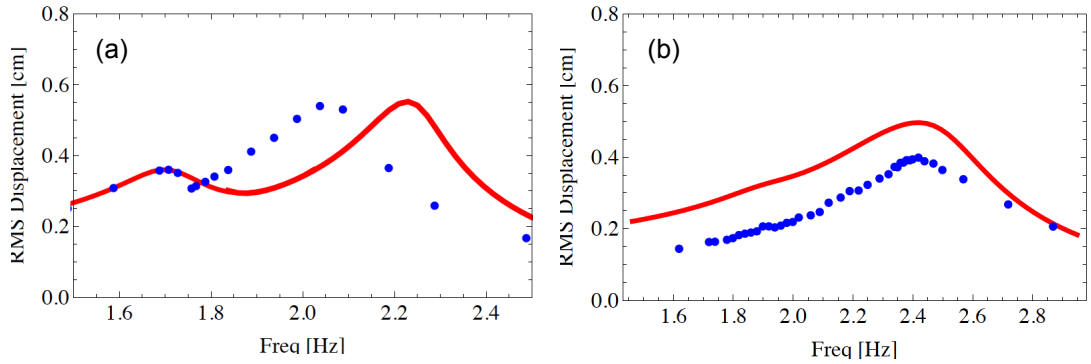

Figure 3.8: Frequency response curve under harmonic base acceleration of 0.3 m/s^2. Results are obtained for (a) $h/L = 0.2$, (b) $h/L = 0.3$, μ_1=0.04, and μ_2=0.054. Solid lines represent theoretical results while asterisk represent experimental findings.

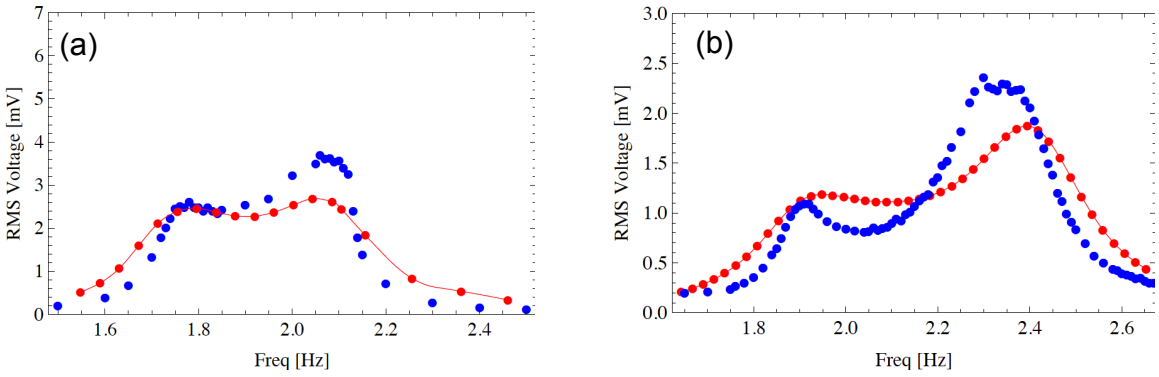

Figure 3.9: Voltage response curves under a harmonic base acceleration of 0.3 m/s^2. Results are obtained for (a) $h/L = 0.2$, (b) $h/L = 0.3$, μ_1=0.04, and μ_2=0.054. Joined circles represent theoretical results.

though the displacement response curve did not exhibit a clear peak near half the second modal frequency when $h/L = 0.3$, both of the theoretical and experimental voltage responses exhibit clear response peaks near this frequency. This signifies that the high-frequency small-magnitude motions occurring at twice the excitation frequency contribute significantly to the output voltage.

For further model verification purposes, we repeated the experiment with $h/L = 0.2$ using a different applied field, $\bar{H}$. This time we inverted one of the magnets such that the two magnets have similar polarity. This resulted in the magnetic field profile shown in Fig. 3.10 (a). The theoretical results presented in Fig. 3.10 (b) again show good qualitative agreement with the experimental findings. Quite interestingly, both of the theory and experiment predict significant amplification in the output voltage resulting from changing the magnetic field. This highlights the clear influence of

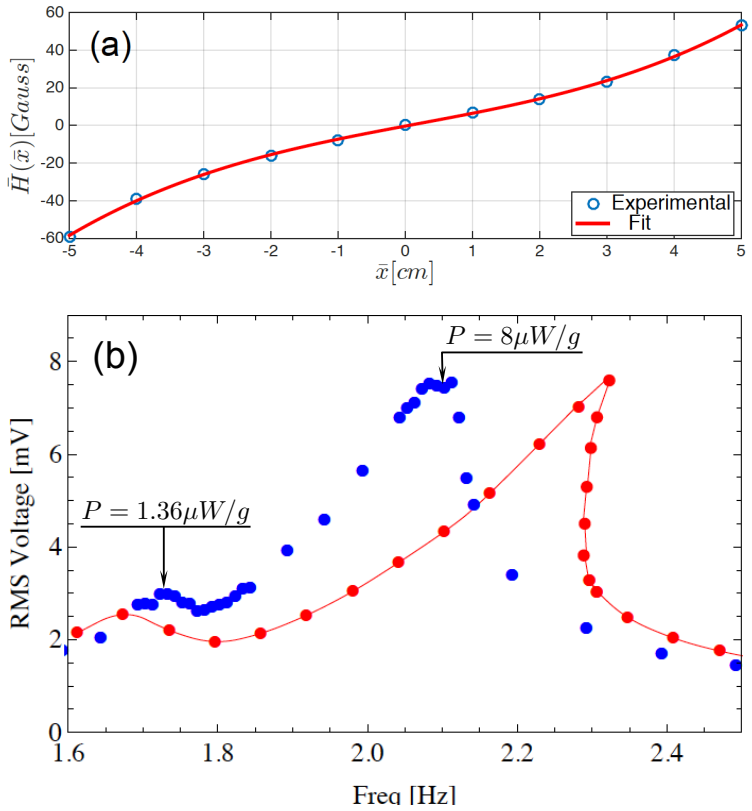

Figure 3.10: Voltage response under a harmonic base acceleration of 0.3 m/s^2. Results are obtained for $h/L = 0.2$, and μ_1=0.04, μ_2=0.054. Joined circles represent theoretical results.

the magnetic field distribution on the performance of the harvester.

Chapter 4

Response to Parametric Excitations

4.1 Motivations

This chapter evaluates the efficiency of harvesting energy from Faraday's surface waves. Faraday's waves can be excited when a fluid-carrying container is subjected to harmonic base excitations in a direction parallel to the container's height with a frequency close to twice one of the infinite modal frequencies of the fluid column. The phenomenon was first observed by Faraday in 1861 who noted that the waves developing on the free surface of a liquid resting upon a vertically vibrating support complete one cycle of vibration for every two cycles of excitation [41]. Twenty eight years later, the same concept was explored further by Melde using a vertically-excited pendulum and then by the famous paper of Strutt and Lord Rayleigh on the crispation of fluid resting upon a vibrating support [42].

The development of surface waves in the container follows the same exact principle that a child on a swing intuitively learns to adapt in order to pump up the amplitude of the swing oscillation. By lowering the center of gravity of his body when he swings down and raising it when he swings up, the child is essentially exciting the swing at twice its fundamental frequency in a phenomenon known as principle parametric resonance.

4.2 Experimental Setup

To evaluate the proposed idea, we designed and constructed the setup shown in Fig. 4.1. The setup consists of a plastic rectangular container of height 15.24 cm, width 15.24 cm, and depth 7.62 cm. The container is mounted on the top of an electrodynamic shaker as shown in Fig. 4.1 and filled with the ferrofluid for the purpose of energy generation. To create a net magnetization in the fluid, two static magnets are mounted at either side of the container. The location of the magnets can be changed vertically and horizontally to evaluate the influence of the magnetic field on the harvester's performance. The electric field generated as a result of the change in magnetic flux induced by the motion of the fluid is collected using a brass coil (gauge 12) wound around the container as shown in the figure.

The magnitude and frequency of the parametric base acceleration generated using the electrodynamic shaker are controlled via a closed-loop controller which measures the acceleration using an accelerometer mounted on the shaker's base and minimizes the error between the measured and desired value.

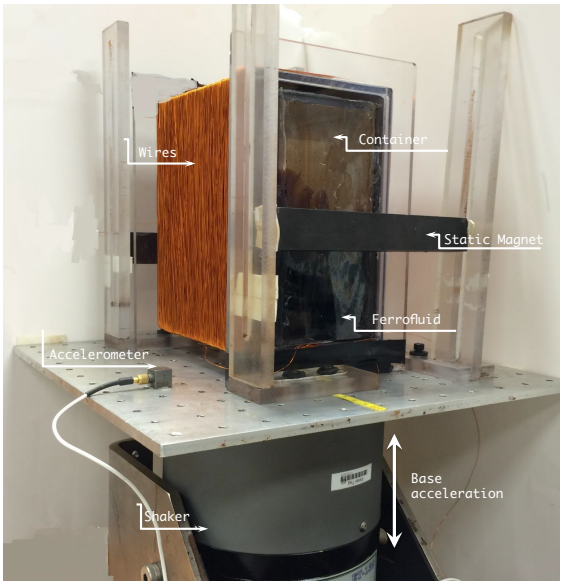

Figure 4.1: A depiction of the parametric excitation setup used in the experiments.

4.3 Experimental Investigation

To draw a general picture of the response, the container is first subjected to parametric excitations with a fixed acceleration magnitude of 2 m/sec^2. The frequency is varied linearly using a chirp signal at a rate of 0.0025 Hz/sec and covers a large frequency bandwidth which spans the region between 2 and 15 Hz. At each frequency step, the output voltage is recorded across a resistive load of $R_L = 137$ Ohms which was chosen to match the resistance of the coil. This results in favorable conditions for power flow. The initial fluid height was fixed at 46 mm and the center of the static magnets is placed at a distance of 2 cm from the side of the container and at 2 cm above the fluid surface. The magnets are oriented to have opposite polarities resulting in the magnetic field distribution, (MFD2) shown in Fig. 4.2.

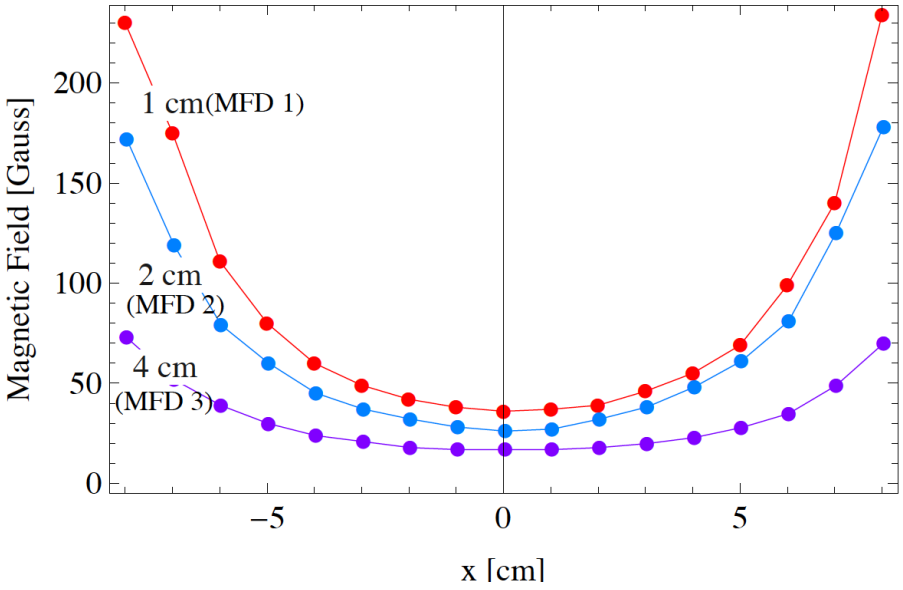

Figure 4.2: Variation of the magnetic field across the width of the container. MFD stands for the Magnetic Field Distribution and the number refers to the horizontal distance from the center of the magnet to the container's wall.

Figure 4.3 depicts the voltage-frequency sweep which illustrates several pronounced peaks in the frequency response. These peaks occur near twice one of the modal frequencies of the fluid column, and, except for the first mode, are more pronounced near twice the modal frequencies of the even modes. The experimentally-observed peaks occur at frequencies that are slightly lower than the theoretical values. For instance, as shown in Table 4.1, the first modal frequency obtained theoretically for a height of 46 mm is 3.89 Hz, while that obtained experimentally is around 3.5

Hz. This trend in frequency reduction appears for all modal frequencies revealing that the magnetic field has a softening influence on the dynamics of the surface waves. We believe that, when the magnets are placed slightly above the container, as in this case, they serve to pull the fluid towards the walls and reduce the fluid resistance to motion, thereby reducing the effective stiffness of the fluid. In other words, the magnetic field seems to produce a negative restoring force influence on the dynamics. Figure 4.4 illustrates how the placement of the magnets along the vertical axis has a tremendous influence on the static surface shape.

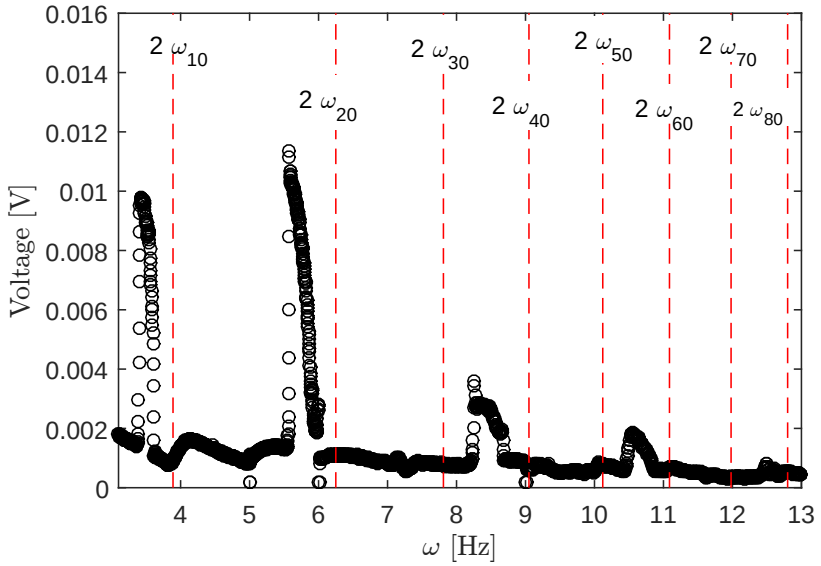

Figure 4.3: Variation of the output voltage with the frequency as obtained for MFD (MFD2) using a chirp frequency input.

Table 4.1: Experimental and theoretical modal frequencies for an initial fluid height $h = 46$ mm, and magnets with opposite polarity placed at a height of 2 cm above the surface and a distance of 2 cm from the walls.

Modal frequency	Theoretical [Hz]	Experimental [Hz]
$2\omega_{10}$	3.89	3.50
$2\omega_{20}$	6.26	5.8
$2\omega_{30}$	7.81	7.40
$2\omega_{40}$	9.05	8.42

The influence of the magnetic field on the first modal frequency is further studied by changing the location of the magnets with respect of the surface. Table 4.2 demonstrates the influence of the

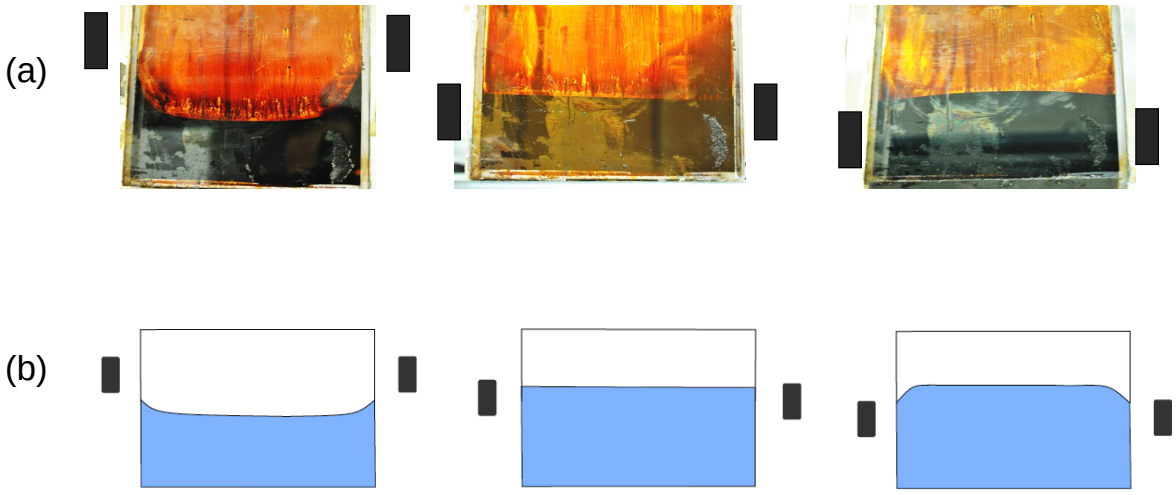

Figure 4.4: Effect of the magnetic field placement on the static surface profile. (a) Experiments, and (b) schematic

vertical distance on the first modal frequency while keeping the horizontal distance from the walls constant at 2 cm. It is clear that the softening influence of the magnetic field is increased by placing the magnets either above or below the surface. The softening influence is larger when the magnets are placed above the surface.

Table 4.2: Experimental and theoretical values of the first modal frequency for a fluid height $h = 46$ mm, and magnets with opposite polarity placed at different height from the surface and a distance of 2 cm from the walls.

z_0 [cm]	$2\omega_{10,Th}$ [Hz]	$2\omega_{10,exp}$ [Hz]	error [%]
-2	3.89	3.44	11.5
0	3.89	3.5	10.2
2	3.89	3.28	15.7

Table 4.3 shows the influence of the horizontal distance on the first modal frequency while keeping the vertical distance constant at 2 cm above the liquid surface. It is shown that the softening influence of the magnetic field is increased as the magnets placed closer toward the container walls, as a result of the increase is the magnetic field applied on the ferrofluid.

Table 4.3: Experimental and theoretical values of the first modal frequency for a fluid height $h = 46$ mm, and magnets with opposite polarity placed at different distances from the walls and a height of 2 cm above the surface.

x_0 [cm]	$2\omega_{10,Th}$ [Hz]	$2\omega_{10,exp}$ [Hz]	error (%)
1	3.89	3.56	8.5 %
2	3.89	3.66	5.9 %
3	3.89	3.82	1.8 %

4.3.1 Principle Parametric Resonance of the Second Sloshing Mode:

Since, as shown in Fig. 4.3, maximum peak voltage is generated near twice the second modal frequency, we study the voltage behavior in more details and for different acceleration levels as depicted in Fig. 4.5. For a base acceleration of 1.5 m/sec^2, the response exhibits a softening-type nonlinear behavior where large-amplitude responses occur at frequencies that are lower than twice the modal frequency of the response. Due to the hysteretic nature of the nonlinear response, the harvester exhibits a larger bandwidth in the backward sweep (dots), as compared to the forward sweep (rectangles). The maximum voltage recorded is 0.0105 Volts across a resistive load of 137 Ohms.

As the base acceleration is increased to 2 m/sec^2, the effective bandwidth of the harvester increases in both directions of the frequency sweep. In the backward sweep, the bandwidth increases to approximately 0.6 Hz; while in the forward sweep, it increases to approximately 0.5 Hz. The maximum voltage recorded does not increase appreciably and stays at around 0.011 Volts. The reason behind the very small increase in the voltage is not very clear. Nonetheless, in the author's opinion, it could stem from a saturation in the voltage occurring as the amplitude of the surface waves increases. This is indicated by the abrupt change in the slope of the voltage-frequency curve as shown in Fig. 4.5 (b). The abrupt change in slope is even more pronounced in the case involving the 3 m/sec^2 base acceleration as shown in Fig. 4.5 (c). During the experiments, visual inspection of the response revealed that, at the point when the slope of the voltage-response curve changes, the surface waves become so large that they almost reach the top of the container.

As the base acceleration is increased further to 3 m/sec^2, the effective bandwidth of the harvester increases in both directions of the frequency sweep. In the backward sweep, the bandwidth increases to approximately 0.7 Hz; while in the forward sweep, it increases to approximately 0.6 Hz, which are both almost double the bandwidth at a base acceleration of 1.5 m/sec^2. The maximum

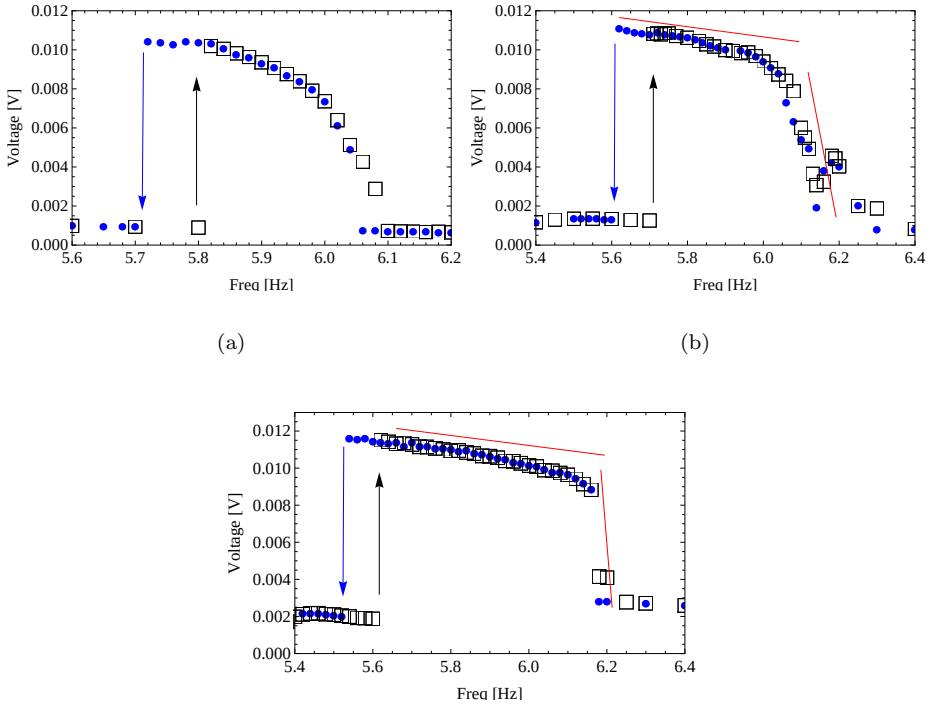

Figure 4.5: Variation of the output voltage across a resistive load $R_L = 137$ Ohms with the excitation frequency. Results are obtained for the magnetic field distribution MFD2 shown in Fig. 4.2 and a base acceleration magnitude of (a) 1.5 m/sec^2, (b) 2 m/sec^2, and (c) 3 m/sec^2. Dots represent a backward sweep while rectangles represent a forward sweep.

voltage amplitude increases slightly to reach approximately 0.012 Volts.

Next, the influence of the magnetic field strength on the output voltage is investigated as depicted in Fig. 4.6. To this end, two magnets of opposite polarity and equal strength were placed on either side of the container's walls such that their centers are at a distance of 2 cm above the surface of the fluid. The horizontal distance between the walls and the center of the magnets was then changed incrementally. The resulting MFD at the surface of the fluid was measured using a Gauss meter and recorded as depicted in Fig. 4.2. In the three cases, the MFD exhibits a quadratic dependence on the distance with the closest magnet producing higher fields over the whole range considered.

Results shown in Fig. 4.6 demonstrate that the output voltage increase with the strength of the magnetic field. As such, when the magnets are placed closer to the container walls, larger output voltages are obtained. It can also be noted that the frequency bandwidth wherein the parametric

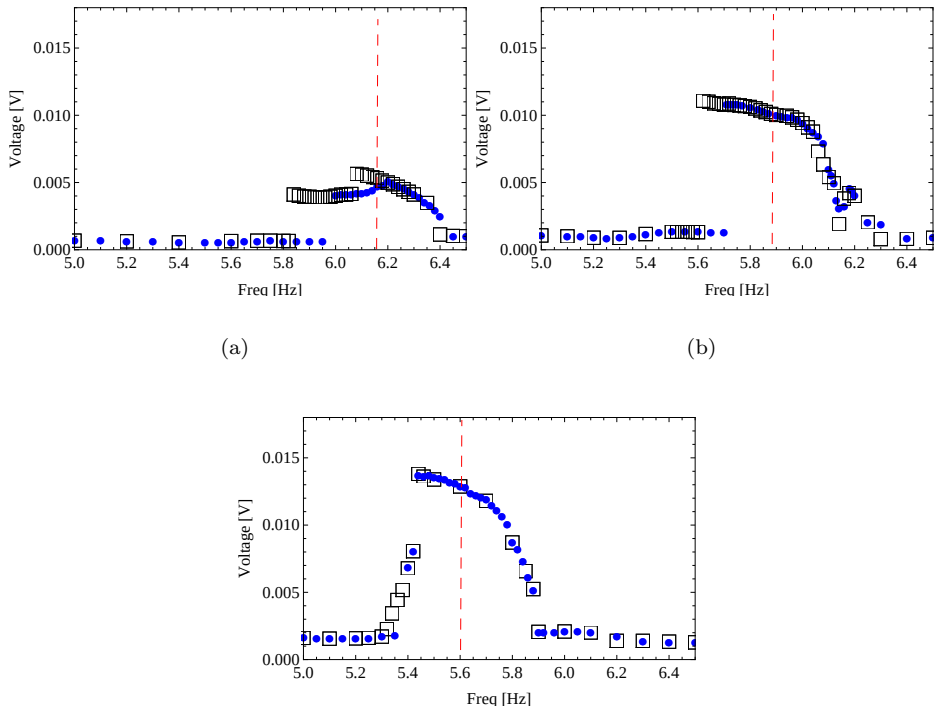

Figure 4.6: Variation of the output voltage with the excitation frequency measured across $R_L = 137$ Ohm for the different magnetic field distributions shown in Fig. 4.2. Results are obtained for a base acceleration of 2 m/sec^2, a fluid height of 46 mm, and (a) MFD1, (b) MFD2, (c) MFD3. Rectangles represent a backward sweep while dots represent a forward sweep.

resonance can be activated shifts towards lower frequencies when the magnetic field is increased. As described earlier, this is due to the softening influence of the magnetic field when the magnets are placed above the surface.

In addition to the frequency response curves, we also investigate the forced response of the harvester for the three different magnetic field distributions shown in Fig 4.2. In each case, the base acceleration is increased from 0 to 4 m/s^2 and the output voltage is recorded at a single frequency corresponding to twice the second modal frequency of the fluid column. In the first case shown in Fig. 4.7 (a), corresponding to the lowest magnetic field strength, MFD3, the output voltage remains negligible up to a threshold base acceleration of 1.1 m/s^2 beyond which the harvester starts to produce measurable output. Subsequently, the output voltage increases monotonically with the acceleration level until it saturates near 0.006 Volts. The transition of the voltage from zero to large values is smooth without hysteresis.

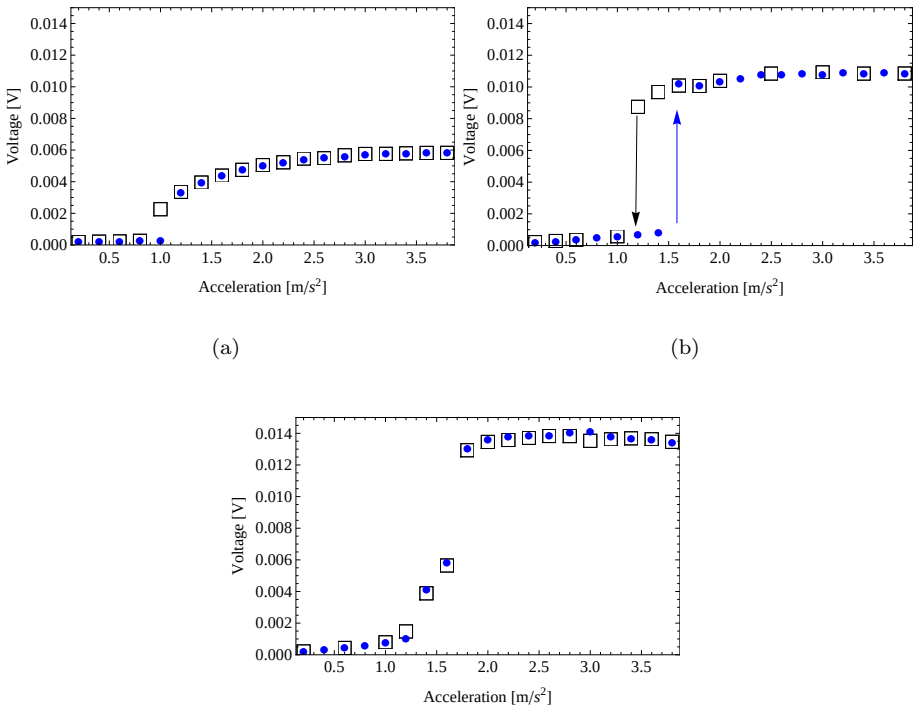

Figure 4.7: Variation of the output voltage with the excitation magnitude measured across $R_L = 137$ Ohm for the different magnetic field distributions shown in Fig. 4.2. Results are obtained for a base acceleration of 2 m/sec^2, a fluid height of 46 mm, and (a) MFD3, (b) MFD2, (c) MFD1. Rectangles represent a backward sweep while dots represent a forward sweep.

For the case involving the medium magnetic field, MFD2, Fig. 4.7 (b), the threshold base acceleration required to initiate measurable responses increases to 1.4 m/s^2 followed by a sudden jump to large amplitude voltages. The maximum voltage level achieved in this case is approximately 0.01 Volts which is much larger than that achieved for the lower magnetic field. A clear hysteretic behavior due to a subcritical bifurcation can also be seen. The hysteresis happens because the jump to large-amplitude voltages in the forward sweep occurs at a higher value when compared to the jump from the large amplitude voltages in the backward sweep.

For the case involving the highest magnetic field values, Fig. 4.7 (b), the threshold acceleration level is not very clear since there is no clear transition from zero voltage output to measurable values. Nonetheless, the harvester can now produce higher acceleration levels around 0.014 Volts under high base accelerations.

The output power of the harvester as a function of the load resistance is depicted in Fig.

4.8. Results, which were obtained for a base acceleration of 2 m/sec^2, an excitation frequency of 5.84 Hz, demonstrate a typical power-resistance curve with maximum power occurring at an optimal load resistance that is very close to the coil resistance of 137 Ohm.

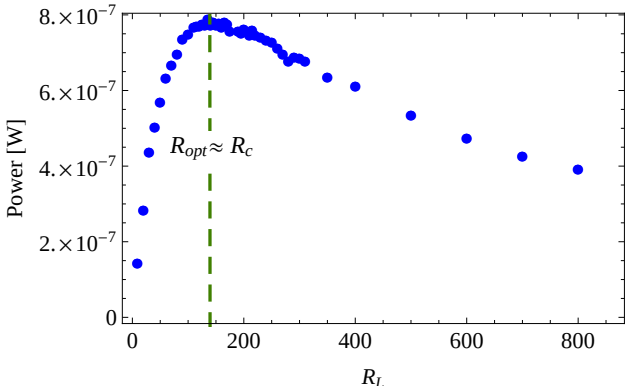

Figure 4.8: Variation of the output power with the load resistance. Results are obtained for a fluid height of 46 mm, a base acceleration of 2 m/sec^2, an excitation frequency of 5.84 Hz, and the magnetic field distribution MFD2 shown in Fig. 4.2

4.3.2 Principle Parametric Resonance of The First Mode:

Next, we compare the voltage about obtained near the first and second modes for the same excitation level of 2 m/sec^2 and the magnetic field distribution, MFD2. As shown in Fig. 4.9, for the magnetic field distribution considered, exciting the harvester near twice its second modal frequency produces four times the voltage level and three times the response bandwidth when compared to exciting it near twice its first modal frequency. The reason behind the improved output near the second mode is not very clear. Nonetheless, in the author's opinion, it must be related to the modal shapes of the surface waves in conjunction with the magnetic field distribution across the width of the container.

To further investigate this fact, we reversed the polarity of one of the magnets such that the MFD is now cubic in nature as shown in Fig. 4.10. The experiment is then repeated while keeping all other conditions the same. The results associated with the first mode are depicted in Fig. 4.11 where Fig. 4.11 (a) presents the results for opposite polarity; i.e. "even" quadratic MFD (EMFD), while Fig. 4.11 (b) presents the results for the same polarity which results in an "odd" cubic MFD (OMFD). It is evident that, the output voltage associated with the OMFD is almost four times that obtained using the EMFD. This points to a direct relationship between the output voltage and a

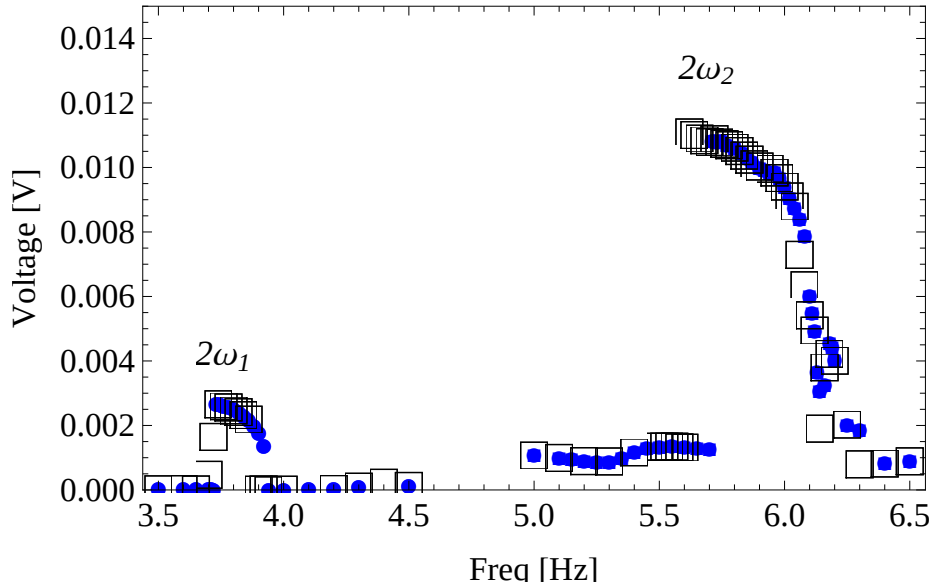

Figure 4.9: Variation of the output voltage with the excitation frequency across $R_L = 137$ Ohm resistor. Results are obtained for a fluid height of 46 mm, a base acceleration of 2 m/sec^2, and the magnetic field distribution MFD2 shown in Fig. 4.2. Dots represents a forward sweep while squares represents a backward sweep

weighted orthogonality between the mode shape of the response and the MFD. Note that the first mode shape is odd in nature while the second mode shape is even.

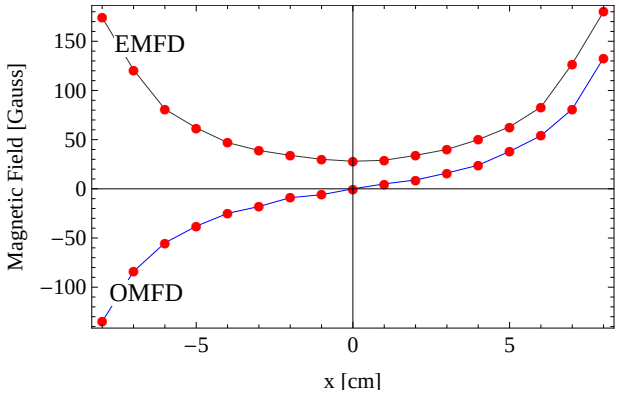

Figure 4.10: Variation of the magnetic field across the width of the container. EMFD stands for the "even" magnetic field distribution and OMFD stands for the "odd" magnetic field distribution.

To further confirm this observation, we repeated the experiment for excitation frequencies near the second "even" mode as depicted in Fig. 4.12. As predicted, for the same polarity, where the MFD is odd, the harvester does not produce any measurable voltage levels as shown in Fig. 4.12 (b). On the other hand, when the MFD is even similar to the modal shape of the response, the

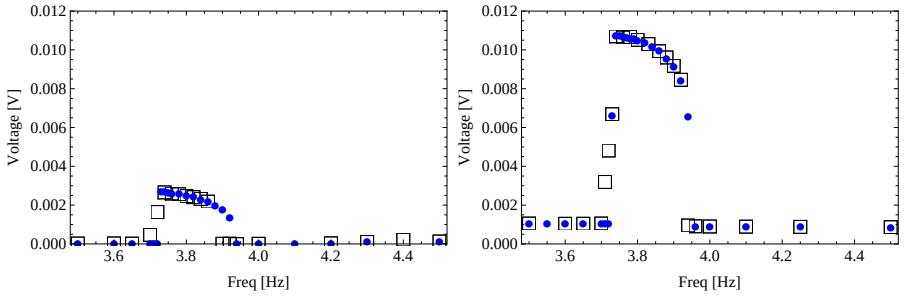

(a) (b)

Figure 4.11: Variation of the output voltage with the excitation frequency across $R_L = 137$ Ohm resistor. Results are obtained for a fluid height of 46 mm, a base acceleration of 2 m/sec^2, and (a) the magnetic field distribution EMFD, (b) the magnetic field distribution OMFD. Dots represents a forward sweep while squares represents a backward sweep.

harvester produces large voltage outputs.

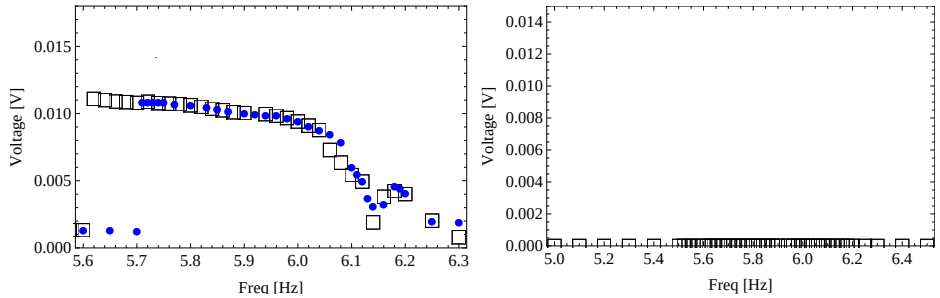

(a) (b)

Figure 4.12: Variation of the output voltage with the excitation frequency across $R_L = 137$ Ohm resistor. Results are obtained for a fluid height of 46 mm, a base acceleration of 2 m/sec^2, and (a) the magnetic field distribution EMFD, (b) the magnetic field distribution OMFD. Dots represents a forward sweep while squares represents a backward sweep.

4.4 Mathematical Model

In this section, we obtain a mathematical model to capture the dynamics of the harvester. To this end, we consider the two-dimensional finite-amplitude sloshing dynamics of an irrotational, incompressible fluid in a rectangular container of width L. The fluid whose mass density is denoted by ρ is assumed to be of height h as shown in Fig. 4.13. As the fluid starts to move due to

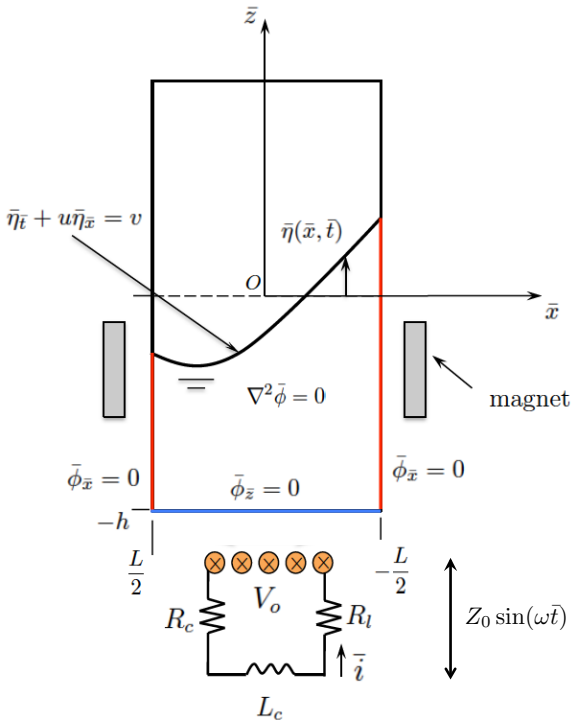

Figure 4.13: A schematic of the fluid sloshing in a rectangular container as a result of a parametric excitation.

external perturbations, surface waves of height $\bar{\eta}(\bar{x},\bar{t})$ arise. The equations and associated boundary conditions governing the two-dimensional motion of the fluid can be written as:

$$\mathbf{u}(\bar{x},\bar{z},\bar{t}) = u\mathbf{i} + v\mathbf{j} = \nabla\bar{\phi}, \tag{4.1a}$$

$$\nabla^2\bar{\phi} = 0, \qquad -\frac{L}{2} \le \bar{x} \le \frac{L}{2}, \qquad -h \le \bar{z} \le \bar{\eta}(\bar{x},\bar{t}), \tag{4.1b}$$

$$\bar{\phi}_{\bar{x}} = 0 \quad \text{on} \quad \bar{x} = \pm\frac{L}{2}, \qquad \bar{\phi}_{\bar{z}} = 0 \quad \text{on} \quad \bar{z} = -h, \tag{4.1c}$$

$$\bar{\eta}_{\bar{t}} + u\bar{\eta}_{\bar{x}} = v, \quad \text{on} \quad \bar{z} = \bar{\eta}(\bar{x},\bar{t}), \tag{4.1d}$$

$$\bar{\phi}_{\bar{t}} + \frac{u^2+v^2}{2} + g\bar{\eta} - \bar{\eta} Z_0 \omega^2 \sin(\omega \bar{t}) - \frac{\mu_0}{\rho} \int_0^{\bar{H}} \bar{M} d\bar{H} = \bar{C}. \quad \text{on} \quad \bar{z} = \bar{\eta}(\bar{x}, \bar{t}), \tag{4.1e}$$

Here, the subscripts denote partial derivatives with respect to the independent variables. Equation (4.1) (a) states the irrationality of the velocity field by expressing the two-dimensional velocity field, $\mathbf{u}$, as the gradient of a scalar potential, $\bar{\phi}$. Equation (4.1) (b) is a consequence of the incompressibility assumption for which the continuity equation requires the Laplacian of the velocity potential to vanish. Equation (4.1) (c) states that the velocity normal to the sidewalls and bottom wall vanishes. Equation (4.1) (d) is the kinematic boundary condition at the surface which states that the velocity of a fluid particle on the surface must be equal to the velocity of the surface itself. Finally, Equation (4.1) (e) represents the dynamic boundary condition at the surface obtained by enforcing the unsteady Bernoulli equation.

In Equation (4.1)(e), the first term accounts for the unsteadiness in the velocity field; the second term represents the kinetic energy of the fluid; the third term accounts for the potential energy; and the fifth term represents forces exerted on the surface due to a harmonic base acceleration in the $\bar{x}$ direction. Here, Z_0 and ω are the amplitude and frequency of the parametric excitation, respectively. Finally, the sixth term represents the magnetic moment exerted on the surface, where $\bar{M}$ and $\bar{H}$ are the magnetization and magnetic field, respectively; μ_0 represents the permeability of vacuum, and $\bar{C}$ is a constant.

In this study, the applied magnetic field will be static and will vary along the x-axis only, i.e., $\bar{H}(\bar{x}, \bar{y}, \bar{z}, \bar{t}) = \bar{H}(\bar{x})$. The magnetic field is assumed to have a linear relationship with the magnetization, $\bar{M}(\bar{x}) = \chi_m \bar{H}(\bar{x})$, that is,

$$\int_0^{\bar{H}} \bar{M}(\bar{x}) d\bar{H} = \frac{\chi_m}{2} \bar{H}^2(\bar{x}). \tag{4.2}$$

Equation (4.1) can be further non-dimensionalized by introducing the following dimensionless quan-

tities:

$$x = \frac{\bar{x}}{L}, \qquad z = \frac{\bar{z}}{L}, \qquad \eta = \frac{\bar{\eta}}{L} \qquad t = \omega_0 \bar{t}, \qquad \phi = \frac{\bar{\phi}}{L^2 \omega_0}, \qquad \bar{C} = \frac{C}{L^2 \omega_0^2},$$
$$z_0 = \frac{Z_0}{L}, \qquad \Omega = \frac{\omega}{\omega_0}, \qquad H = \frac{\bar{H}}{H_0}, \tag{4.3}$$

where $\omega_0 = \sqrt{\frac{\pi g}{L}\delta_1}$ is the first modal frequency of the fluid column in the absence of surface tension and magnetic field, $\delta_1 = \tanh(\pi h/L)$, and $H_0 = L\omega_0\sqrt{\frac{2\rho}{\mu_0}}$. This yields the following non-dimensional equations:

$$\nabla^2 \phi = 0, \qquad -\frac{1}{2} \leq x \leq \frac{1}{2}, \qquad -h/L \leq z \leq \eta(x,t), \tag{4.4a}$$

$$\phi_x = 0 \quad \text{on} \quad x = \pm\frac{1}{2}, \qquad \phi_z = 0 \quad \text{on} \quad z = -h/L, \tag{4.4b}$$

$$\eta_t + \phi_x \eta_x = \phi_z, \quad \text{on} \quad z = \eta(x,t), \tag{4.4c}$$

$$\phi_t + \frac{\phi_x^2 + \phi_z^2}{2} + \frac{1}{\pi\delta_1}\eta - \eta z_0 \Omega^2 \sin\Omega t - \chi_m H^2 = C \qquad \text{on } z = \eta(x,t), \tag{4.4d}$$

4.5 Single-Mode Response

Away from any internal resonances, a single-mode solution is sufficient to capture the dynamics of the sloshing waves. Since Equations (4.4)(c) and (4.4)(d) are nonlinear, an exact solution cannot be found. To overcome this issue, we obtain an approximate analytical solution of the equations using the method of multiple scales. To this end, we expand the time dependence in the equation into multiple time scales in the form:

$$T_k = \varepsilon^k t, \qquad k = 0, 1, 2 \ldots \tag{4.5}$$

where ε is a bookkeeping parameter. The time derivatives can be further expressed as

$$\frac{d}{dt} = D_0 + \varepsilon D_1 + \varepsilon^2 D_2 + O(\varepsilon^3), \tag{4.6}$$

where $D_k = \frac{\partial}{\partial T_k}$. Furthermore, we expand ϕ, η, and C in the following forms:

$$\begin{aligned}
\phi(x,z,t,\varepsilon) &= \varepsilon\phi_1(x,z,T_0,T_1,T_2) + \varepsilon^2\phi_2(x,z,T_0,T_1,T_2) + \varepsilon^3\phi_3(x,z,T_0,T_1,T_2) + O(\varepsilon^4) \\
\eta(x,t,\varepsilon) &= \varepsilon\eta_1(x,T_0,T_1,T_2) + \varepsilon^2\eta_2(x,T_0,T_1,T_2) + \varepsilon^3\eta_3(x,T_0,T_1,T_2) + O(\varepsilon^4), \\
C &= \varepsilon^2 C_2 + \varepsilon^3 C_3 + O(\varepsilon^4).
\end{aligned} \tag{4.7}$$

To express the nearness of the excitation frequency to twice the modal frequency of a given sloshing mode, we let $\Omega = 2\omega_k + \varepsilon^2\sigma$, where σ is a small detuning parameter. Furthermore, we treat only soft excitations for which z_0 is very small and can be scaled at order ε^2.

Since the dynamic and kinematic boundary conditions are evaluated at the surface $\eta(x,t)$, which is still unknown, we expand the dependence of ϕ on η in a Taylor series around $\eta = 0$. In other words, we let $\phi(\eta) \approx \phi(0) + \varepsilon\phi_z(0)\eta + \varepsilon^2/2\phi_{zz}(0)\eta^2 + O(\varepsilon^3)$. Note that this assumption is accurate as long as the surface waves are finite but sufficiently small.

Upon substituting Equations (4.5-4.7) into Equation (4.4) (d), and (4.4) (e), then collecting terms of like powers of ε, we obtain the following cascade of linear partial differential equations:

$O(\varepsilon^1)$:

$$D_0\phi_1 + \frac{1}{\pi\delta_1}(\eta_1) = 0, \tag{4.8a}$$

$$D_0\eta_1 - \phi_{1z} = 0, \tag{4.8b}$$

$O(\varepsilon^2)$:

$$D_0\phi_2 + \frac{1}{\pi\delta_1}(\eta_2) = -\frac{1}{2}(\phi_{1z}^2 + \phi_{1x}^2) - D_1\phi_1 + \eta_1 D_0\phi_{1z} + C_2, \tag{4.9a}$$

$$D_0\eta_2 - \phi_{2z} = -D_1\eta_1 + \eta_1\phi_{1zz} - \eta_{1x}\phi_{1x}, \tag{4.9b}$$

$O(\varepsilon^3)$:

$$\begin{aligned} D_0\phi_3 + \frac{1}{\pi\delta_1}(\eta_3) = &- \phi_{1z}\phi_{2z} - \eta_1\phi_{1z}\phi_{1zz} - \phi_{1x}\phi_{2x} \\ &- \eta_1\phi_{1x}\phi_{1xz} - D_2\phi_1 - D_1\phi_2 - \eta_2 D_1\phi_{1z} \\ &+ \eta_1 D_0\phi_{2z} - \frac{1}{2}\eta_1^2 D_0\phi_{1zz} + 4z_0\omega_k^2\eta_1\sin(2\omega_k T_0) + C_3, \end{aligned} \tag{4.10a}$$

$$\begin{aligned} D_0\eta_3 - \phi_{3z} = &- D_2\eta_1 - D_1\eta_2 + \eta_2\phi_{1zz} + \eta_1\phi_{2zz} + \frac{1}{2}\eta_1^2\phi_{1zzz} \\ &- \eta_{2x}\phi_{1x} - \eta_{1x}\phi_{2x} - \eta_1\eta_{1x}\phi_{1xz}. \end{aligned} \tag{4.10b}$$

In the absence of internal resonances between the sloshing modes, a single-mode response is sufficient to describe the dynamics of the system when that mode is being excited parametrically near twice one of its modal frequencies. As such, the solution of the first-order problem can be written as:

$$\begin{aligned} \phi_1^e(x,z,T_0,T_1,T_2) &= \frac{1}{\pi\delta_k}\Big(A_k(T_1,T_2)e^{i\omega_k T_0} + cc\Big)\mathrm{C}_k(x)\mathrm{Ch}_k(z), \\ \phi_1^o(x,z,T_0,T_1,T_2) &= \frac{1}{\pi\delta_k}\Big(A_k(T_1,T_2)e^{i\omega_k T_0} + cc\Big)\mathrm{S}_k(x)\mathrm{Ch}_k(z), \end{aligned} \tag{4.11a}$$

$$\begin{aligned} \eta_1^e(x,z,T_0,T_1,T_2) &= -i\frac{k}{\omega_k}\Big(A_k(T_1,T_2)e^{i\omega_k T_0} + cc\Big)\mathrm{C}_k(x), \\ \eta_1^o(x,z,T_0,T_1,T_2) &= -i\frac{k}{\omega_k}\Big(A_k(T_1,T_2)e^{i\omega_k T_0} + cc\Big)\mathrm{S}_k(x). \end{aligned} \tag{4.11b}$$

where $\omega_k = \sqrt{k\delta_k/\delta_1}$, $A_k(T_1,T_2)$ is a complex-valued functions that will be obtained by enforcing the solvability conditions at a later stage in the analysis and $\bar{A_k}(T_1,T_2)$ is its complex conjugate. Here, the superscripts represent the type of mode (e: even and o: odd), $\mathrm{C}_k(x) = \cos(k\pi x)$, $\mathrm{S}_k(x) = \sin(k\pi x)$, $\mathrm{Ch}_k(z) = \frac{\cosh(k\pi(z+h/L))}{\cosh(k\pi(h/L))}$.

Substituting Equation (4.11) into the second-order problem, Equation (4.9a) and (4.9b), and enforcing the solvability conditions, wherein the right-hand side of Equation (4.9a) is forced to be orthogonal to every solution of the adjoint homogeneous problem, i.e., orthogonal to Equation (4.11), we obtain $D_1A_k = D_1\bar{A}_k = 0$. Upon enforcing the solvability conditions, the particular

solution can be written as:

$$\begin{aligned}\phi_2^e(x,z,T_0,T_1,T_2) &= i\frac{k^2}{8\delta_k^2\omega_k}\Big[\alpha_k \mathrm{S}_{2k}(x)\mathrm{Ch}_{2k}(z) + (1+3\delta_k^2)\Big]A_k^2(T_2)\mathrm{C}_k(x)e^{2i\omega_k T_0} + cc \\ \phi_2^o(x,z,T_0,T_1,T_2) &= i\frac{k^2}{8\delta_k^2\omega_k}\Big[-\alpha_k \mathrm{C}_{2k}(x)\mathrm{Ch}_{2k}(z) + (1+3\delta_k^2)\Big]A_k^2(T_2)\mathrm{C}_k(x)e^{2i\omega_k T_0} + cc\end{aligned} \tag{4.12}$$

where $\mathrm{C}_{2k}(x) = \cos(2k\pi x)$, $\mathrm{S}_{2k}(x) = \sin(2k\pi x)$, $\mathrm{Ch}_{2k}(z) = \frac{\cosh(2k\pi(z+h/L))}{\cosh(2k\pi(h/L))}$,

$$\alpha_k = \frac{4}{(\omega_{2k}^2 - 4\omega_k^2)}\left(\frac{\omega_{2k}^2}{2}(1+\delta_k^2) + (1-3\delta_k^2)\omega_k^2\right), \tag{4.13}$$

$\omega_{2k} = \sqrt{2k\delta_{2k}/\delta_1}$, and the coefficient C_2 is determined by forcing $\int_{-1/2}^{1/2}\eta_2 dx$ to vanish to preserve continuity.

Next, we substitute Equation (4.11) and (4.12) into Equation (4.10a) and (4.10b), then eliminate the secular terms by enforcing the solvability conditions at the third order; this yields:

$$iD_2A_k + N_{eff}A_k^2(T_2)\bar{A}_k(T_2) + F_k\bar{A}_k(T_2)e^{i\sigma T_2} = 0, \tag{4.14}$$

and,

$$F_k = \pi z_0 \omega_k^3 \delta_1. \tag{4.15}$$

where N_{eff} is the effective nonlinearity coefficient. This coefficient represents an average nonlinear stiffness expression which captures the nature of the nonlinear response of the finite-amplitude sloshing modes, and is given by

$$N_{eff} = \frac{k^4\pi^2 p_1(\delta_k)}{16\delta_k^5}. \tag{4.16}$$

The solution of Equation (4.14) is obtained by expressing the unknown complex-valued function A_k in the polar form $A_k = 1/2a_k e^{i\beta_k}$, $\bar{A}_k = 1/2a_k e^{-i\beta_k}$. Upon substituting the polar transformation into Equation (4.14) and separating the real and imaginary parts, we obtain the following equations which govern the dynamic modulation of the system:

$$a_k' = 2\mu_{1k}\frac{\omega_k}{\omega_1}a_k - 2\mu_2\frac{\omega_k^2}{\omega_1^2}a_k^2 - F_k a_k \sin\gamma_k, \tag{4.17a}$$

$$a_k\gamma_k' = 2\sigma a_k - \frac{N_{eff}}{4} - F_k a_k \cos\gamma_k, \tag{4.17b}$$

where the prime represents a derivative with respect to T_2, $\gamma_k = \sigma T_2 - 2\beta_k$, μ_{1k} and μ_{2k} are respectively, a linear and a nonlinear modal damping coefficients added to capture the damping influence in the fluid.

Equation (4.17a), also known as the amplitude equation, captures the slow modulation of the response amplitude; while Equation (4.17b), known as the phase equation, captures the slow modulation in the response phase.

To obtain the long time behavior of the system, we set the time derivatives in Equation (4.17a) and Equation (4.17b) to zero, then square and add the outcome to obtain

$$a_{0k}^2\left[\left(2\mu_{1k}\frac{\omega_k}{\omega_1} + 2\mu_2\frac{\omega_k^2}{\omega_1^2}a_{0k}\right)^2 + \left(2\sigma - \frac{N_{eff}}{4}a_{0k}^2\right)^2 - F_k^2\right] = 0, \tag{4.18}$$

where a_{0k} is the steady-state modal amplitude. Equation (4.18), known as the nonlinear parametric frequency-response equation, exhibits six different roots, two of which are always zero indicating that zero steady-state amplitude is always a possible response of the harvester. The fourth other solutions are non-trivial but can sometimes take negative or complex values which are not physically realizable.

The stability of the resulting steady-state solutions can be assessed by finding the eigenvalues of the Jacobian matrix associated with Equations (4.17a) and (4.17b) and evaluating it at the steady-state roots. If at least one of the eigenvalues of the Jacobian matrix has a positive real part, then the associated steady-state solution is unstable, and, hence physically unrealizable.

Upon obtaining the steady-state roots a_{0k}, the steady-state velocity field and surface amplitude can be written as

$$\begin{aligned}
\phi^e(x,z,t) &= \frac{a_{k0}}{\pi\delta_k}\left(\cos\left(\frac{\Omega}{2}t - \frac{\gamma_{0k}}{2}\right)\right)\mathrm{C}_k(x)\mathrm{Ch}_k(z),\\
\phi^o(x,z,t) &= \frac{a_{k0}}{\pi\delta_k}\left(\cos\left(\frac{\Omega}{2}t - \frac{\gamma_{0k}}{2}\right)\right)\mathrm{S}_k(x)\mathrm{Ch}_k(z),
\end{aligned} \tag{4.19}$$

$$\eta^e(x,z,t) = -i\frac{ka_{k0}}{\omega_k}\left(\cos\left(\frac{\Omega}{2}t - \frac{\gamma_{0k}}{2}\right)\right)\mathrm{C}_k(x),$$
$$\eta^o(x,z,t) = -i\frac{ka_{k0}}{\omega_k}\left(\cos\left(\frac{\Omega}{2}t - \frac{\gamma_{0k}}{2}\right)\right)\mathrm{S}_k(x). \tag{4.20}$$

4.6 Basic Understanding

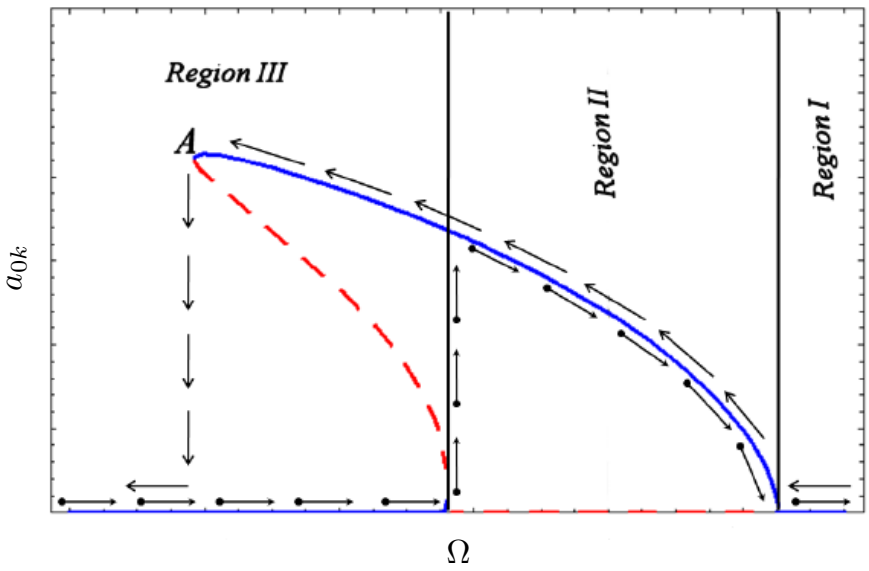

Figure 4.14: A sample parametric frequency-response curve.

To better understand the parametric resonance and the response behavior near the parametric instability, we use Equation (4.18), to generate a typical frequency response curve of a parametrically-excited system near the principle parametric resonance, i.e. $\Omega \approx 2\omega_k$ as shown in Fig. 4.14. The figure can be divided into three regions. In *Region I*, no energy can be harvested because $a_{0k} = 0$ (the trivial solution) is the only real solution of Equation (4.18). As such, the output voltage is also equal to zero. In *Region II*, there are two solutions, the first is the trivial solution (dashed lines) which is unstable, and, hence physically unrealizable. The second is a stable nontrivial solution (solid line). Since the nontrivial nonzero solution is the only stable solution, *Region II* represents a band of frequencies wherein energy can always be harvested regardless of the initial conditions.

In *Region III*, there are two stable solutions and one unstable solution. The two stable

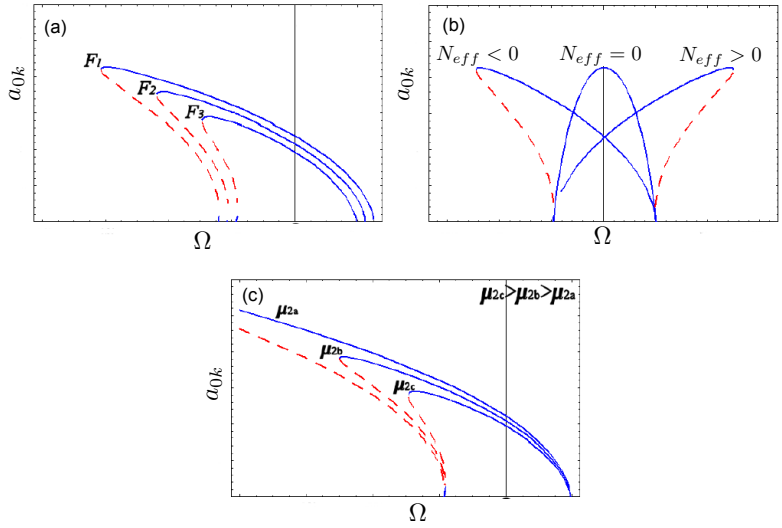

Figure 4.15: Influence of (a) the forcing amplitude, (b) the effective nonlinearity, and (c) the nonlinear quadratic damping on the parametric resonance curve.

solutions are the trivial solution (zero voltage) and the large-amplitude nontrivial solution. As a result, depending on the initial conditions and the basin of attraction of the competing solutions, the harvester can either be scavenging a large amount of energy from the environment or no energy.

For a deeper understanding of the harvesters response, it would be insightful to consider a case when the excitation frequency is in *Region I* and is slowly decreasing towards *Region II*. At the boundary between the two regions, the trivial solution loses stability through a *transcritical* (TC) bifurcation and gives way to a stable nontrivial solution where the harvester starts to scavenge energy from the environment. When decreasing the excitation frequency further, the amplitude of the response a_{0k} increases and more energy gets pumped from the source to the load. This trend continues until the voltage amplitude reaches point A, where a jump to the trivial solution occurs due to a *cyclic-fold* (CF) bifurcation. Beyond this point no energy can be harvested.

Approaching from the left by slowly increasing the excitation frequency, no energy can be harvested until the frequency crosses the boundary between *Region III* and *Region II*. At that point, the amplitude of the output voltage starts to increase due to another TC bifurcation. The resulting nontrivial solution quickly disappears due to another CF bifurcation causing a sudden jump to a large-amplitude response. Increasing the excitation frequency further causes the voltage to decrease until it reaches the boundary between *Region II* and *Region I*. Beyond this point no

energy can be harvested.

By virtue of the preceding discussion, we can conclude the following two critical concepts:

1. To realize effective energy harvesting via parametric excitations, it is essential to guarantee that the harvester is operating on the stable branch of nontrivial solutions as the frequency of excitation is varied. This is always guaranteed in *Region II*, but depends on the initial conditions in *Region III*.

2. To enhance the broadband characteristics of the harvester, the region of nontrivial solutions, i.e. *Region II* and *III*, should be extended over a wide range of the excitation frequency.

To demonstrate how the region of nontrivial solutions could be extended, it is necessary to understand the effect of the design parameters on the frequency-response curve. We will address the effect of the following four parameters:

1. The amplitude of the base acceleration embedded within, F_k. As the amplitude of base acceleration is increased, see Fig. 4.15 (a), the branch of nontrivial solutions, and hence, the region wherein energy could be harvested, extends over a wider range of frequencies. Moreover, the bandwidth of frequencies wherein the trivial solution is unstable, *RegionII*, extends further as the magnitude of excitation is increased. Nonetheless, the magnitude of external excitation is a factor that cannot be controlled by the designer and is solely controlled by the energy source.

2. The effective nonlinearity of the harvester, N_{eff}. The effective nonlinearity determines whether the frequency-response curves bend to the left or to the right and the degree by which these curves bend. As shown in Fig. 4.15 (b), when $N_{eff} = 0$, the voltage-frequency curve is symmetric around $\Omega = 2\omega_k$. The voltage response curves bend to the left when N_{eff} is less than zero and to the right when N_{eff} is greater than zero. The degree by which the curves bend depends on the magnitude of N_{eff}. The effective nonlinearity coefficient is a function of many system parameters. For instance, the effective nonlinearity of a fluid sloshing in a container depends on the fluid depth and the mode being excited.

3. The linear viscous damping effect, μ_{1k}. The linear viscous damping has the opposite influence of the excitation magnitude. When the linear damping increases the bandwidth and amplitude of the response decrease.

4. The nonlinear damping effect, μ_{2k}. As the effective quadratic damping decreases, the stable nontrivial branch of solutions extends over a wider range of the excitation frequency, Fig. 4.15 (c). On the other hand, the bandwidth of *RegionII* is not at all affected by the nonlinear damping.

4.7 Output Voltage

To obtain the voltage induced in one coil, V_o, Faraday's law is applied. For a rectangular tank, with coils wound in the vertical direction and magnetic field applied along the $\bar{x}$-axis, the voltage output per unit width of the harvester can be written

$$V_o = -\frac{d}{d\bar{t}} \iint_{\Sigma(\bar{t})} \mathbf{B}(\bar{x}) d\mathbf{A}, \tag{4.21}$$

where $d\mathbf{A}$ is an element on the moving surface $\Sigma(\bar{t})$, and $\mathbf{B}$ is the vector of magnetic flux density. For the problem at hand, the previous equation can be written as

$$V_o = -\frac{d}{d\bar{t}} \int_{-b}^{b} \int_{-h}^{\bar{\eta}(\bar{t})} B(\bar{x}) d\bar{y} d\bar{z}, \tag{4.22}$$

where $2b$ is the depth of the container. The magnetic flux density, B, can be further related to the applied field via $B(\bar{x}) = \mu_0(1+\chi_m)\bar{H}(\bar{x})$, which upon substitution into Equation (4.21) and carrying out the integration yields

$$V_o = -2bh\mu_o(1+\chi_m)\bar{H}(\bar{x})\frac{d\bar{\eta}}{d\bar{t}}. \tag{4.23}$$

To determine the average output voltage generated in the total number of coils, N, we multiply Equation (4.23) by the number of coils, N, and average the results over the width of the container, L. This yields

$$V_o = \alpha_c \int_{-L/2}^{L/2} \bar{H}(\bar{x}) \frac{d\bar{\eta}}{d\bar{t}} d\bar{x}, \tag{4.24}$$

where $\alpha_c = -2Nb\frac{h}{L}\mu_o(1+\chi_m)$. Note that when $\bar{H}(\bar{x})$ is orthogonal to $\frac{d\bar{\eta}}{d\bar{t}}$ along the $\bar{x}$-axis, the voltage V_o approaches zero.

To determine the current in the induced coil, we apply Kirchhoff's Law and obtain

$$L_c \frac{d\bar{i}}{d\bar{t}} + (R_c + R_L)\bar{i} = \alpha_c \int_{-L/2}^{L/2} \bar{H}(\bar{x}) \frac{d\bar{\eta}}{d\bar{t}} d\bar{x}, \tag{4.25}$$

where $\bar{i}$ is the induced current, R_L is the load resistance, R_c, and L_c are, respectively, the resistance and inductance of the collecting coil.

4.8 Model Validation

In this section, we evaluate the ability of the model developed in the previous section to capture the qualitative behavior of the harvester under different conditions. We start by investigating the response near the principle parametric resonance of the second mode for the MFD (MFD 2) and two different acceleration levels as shown in Fig. 4.16.

For the lower acceleration level of 1.5 m/sec^2, there is a good quantitative agreement between the theory and the experiment for most of the frequency sweep. The bandwidth and magnitude of the voltage are both in good agreement with the experimental data. To match the experimental modal frequency, we had to use an effective fluid height $h_{eff} = 31$ mm as compared to 46 mm height in the absence of the magnetic field. As discussed earlier, the effective height was used to capture the influence of the magnetic field on the modal frequencies.

For the higher acceleration level of 2 m/sec^2, there still is good quantitative agreement between the theory and the experiment especially in terms of the harvester's bandwidth. However, the theoretical response over-predicts the theoretical data especially near the higher end of frequencies. As described earlier, this can be attributed to the saturation of the experimental voltage when the surface waves become very large.

As shown in Fig. 4.17, when the magnetic field strength is increased to MFD1, the theoretical model still predicts the experimental findings in terms of bandwidth and magnitude with relatively good accuracy.

The theoretical forced response was also compared to experimental findings near the second mode as depicted in Fig. 4.18. Two cases were considered using the MFD (MFD3) and (MFD2). For the case involving the lower magnetic field, MFD3, Fig. 4.18 (a), the theoretical model correctly predicts lower voltage magnitudes and non-hysteretic transition between the trivial and non-trivial

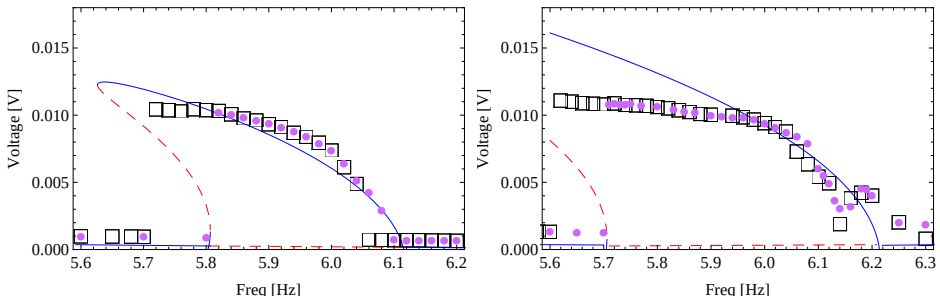

(a) (b)

Figure 4.16: Variation of the voltage with the excitation frequency for the magnetic field distributions MFD2 shown in Fig. 4.2. Results are obtained for a fluid height of 46 mm, and a base acceleration of (a) 1.5 m/sec^2, (b) 2 m/sec^2. Theoretical results are obtained using $\mu_{12} = 0.013$, $\mu_{22} = 0.025$, and h_{eff}=31 mm. Rectangles represent a backward experimental sweep while dots represent a forward sweep. Dashed line represent unstable theoretical response.

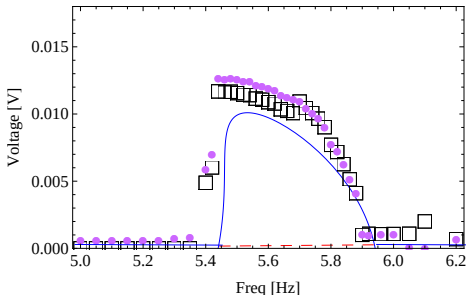

Figure 4.17: Variation of the voltage with the excitation frequency for the magnetic field distributions MFD1 shown in Fig. 4.2. Results are obtained for a fluid height of 46 mm, and a base acceleration of (a) 1.5 m/sec^2, (b) 2 m/sec^2. Theoretical results are obtained using $\mu_{12} = 0.013$, $\mu_{22} = 0.025$, and h_{eff}=31 mm. Rectangles represent a backward experimental sweep while dots represent a forward sweep. Dashed line represent unstable theoretical response.

solutions.

For the higher MFD (MFD2), the theoretical model also correctly predicts the qualitative nature of the response. Specifically, it predicts the presence of the CF and TC bifurcations observed in the experiments. However, due to the saturation effect of the voltage, the theoretical model over-estimates the experimental results at large base accelerations.

The output power of the harvester is also well-predicted experimentally as shown in Fig. 4.19. Both of the theory and experiment agree in predicting that the peak voltage occurs near a load resistance, $R_L = 137$ Ohm, which is equal to the measured coil resistance. However, due to model uncertainties, the theory over-predicts the experimental data over the whole range of electric

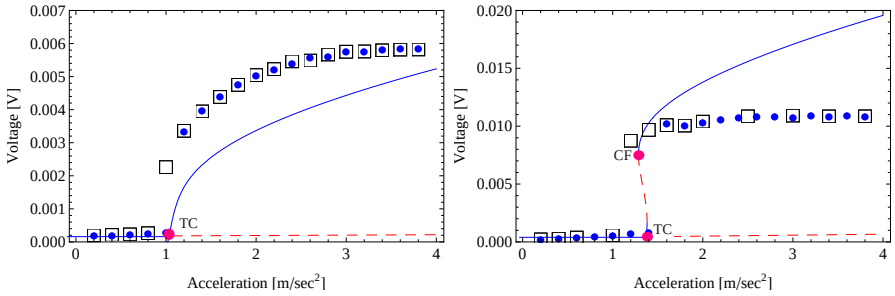

(a) (b)

Figure 4.18: Variation of the voltage with the base acceleration. Results are obtained for a fluid height of 46 mm, and (a) frequency 6.2 Hz, MFD3, (b) 5.84 Hz, MFD1. Theoretical results are obtained using $\mu_{11} = 0.013$ and $\mu_{21} = 0.025$, and (a) h_{eff}=44 mm, (b) h_{eff}=31 mm. Rectangles represent a backward experimental sweep while dots represent a forward sweep. Dashed line represent unstable theoretical response.

loads considered. Note that any discrepancies between the theoretical and experimental voltage measurements propagate significantly in the power calculation since the power is proportional to the square of the voltage.

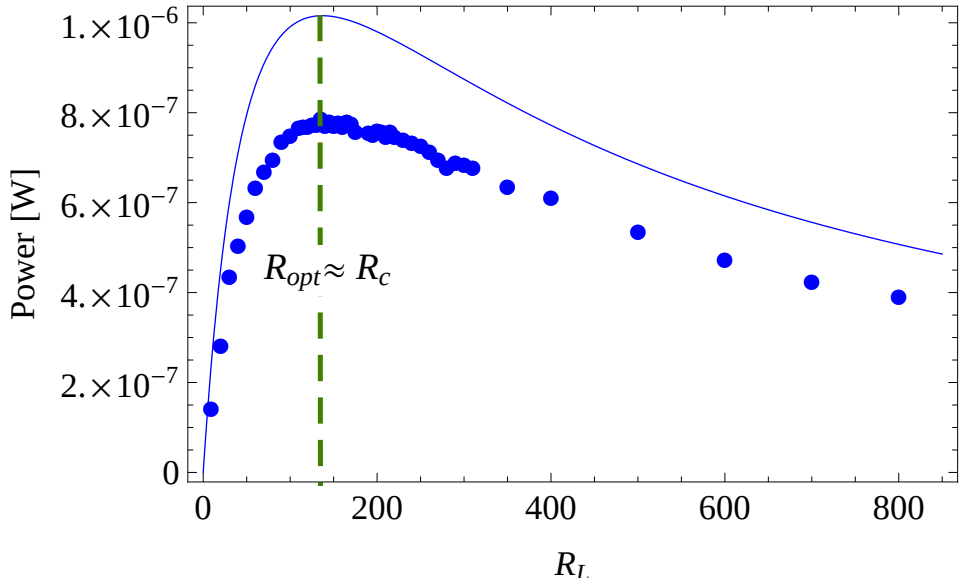

Figure 4.19: Variation of the power with the load resistance. Results are obtained for an initial fluid height of 46 mm, a base acceleration of 2 m/sec^2, and the magnetic field distribution MFD2 shown in Fig. 4.2. Theoretical results are obtained using $\mu_{12} = 0.013$ and $\mu_{22} = 0.025$, h_{eff}=31 mm.

Finally, we evaluate the ability of the model in predicting the influence of the MFD distri-

bution on the response near the principle parametric resonance of the first and second modes. As aforementioned in the experimental section and explained in the theoretical model, the harvester produces much lower power levels when the modal shape of the surface wave is nearly orthogonal to the magnetic field distribution; i.e. when $\int_{-L/2}^{L/2} \bar{H}(\bar{x}) \frac{d\bar{\eta}}{d\bar{t}} d\bar{x} \approx 0$. The theoretical results shown in Fig. 4.20 (a) and (b) confirm this finding since they show that the harvester produces much lower voltages when excited near twice the first "odd" mode while using an "even" magnetic field distribution (EMFD). Similarly, theoretical results presented in Fig. 4.21 illustrates that the second "even" mode produces orders of magnitude lower voltages when excited while using an "odd" magnetic field distribution (OMFD).

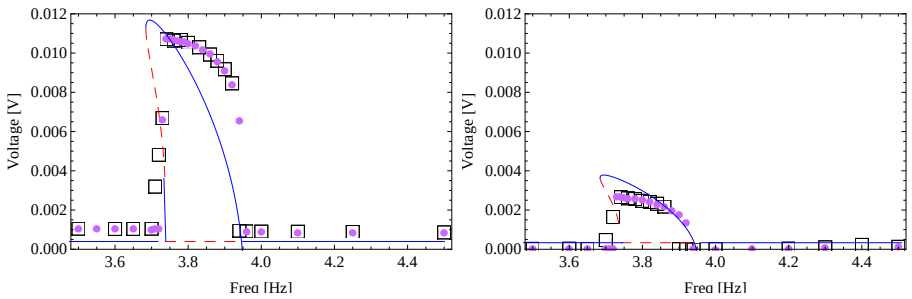

(a) (b)

Figure 4.20: Variation of the voltage with the frequency of excitation. Experimental results are obtained for a fluid height of 46 mm, a load resistance $R_L = 137$ Ohms, and (a) even magnetic field (EMFD), (b) odd magnetic field (OMFD). Theoretical results are obtained using $\mu_{11} = 0.013$ and $\mu_{21} = 0.025$, and h_{eff}=44 mm. Rectangles represent a backward experimental sweep while dots represent a forward sweep. Dashed line represent unstable theoretical response.

4.9 Direct and Parametric Excitation Comparison

Next, we compare the performance of the harvester for a wide range of frequencies under both direct and parametric excitations, using different magnetic field polarity and a liquid height of 46 mm as depicted in Fig. 4.22. The frequency is varied linearly using a chirp signal at a rate of 0.0025 Hz/sec and covering a large frequency bandwidth which spans the region between 3 and 13 Hz. At each frequency step, the output voltage is recorded across a resistive load of $R_L = 137$ Ohms and the center of the static magnets is placed at a distance of 2 cm from the side of the container and at 2 cm above the fluid surface. For both excitation directions, the magnets are

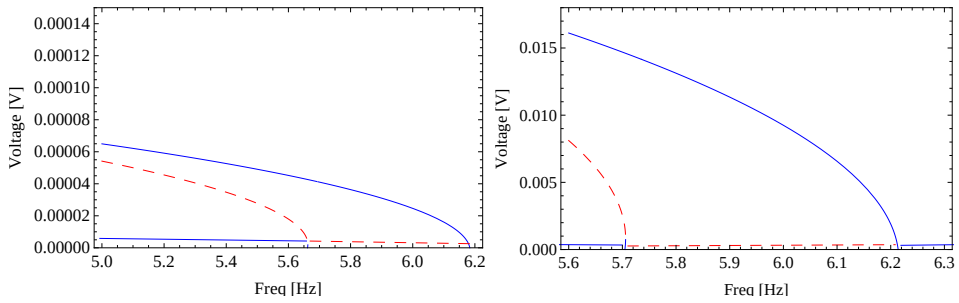

(a) (b)

Figure 4.21: Variation of the voltage with the frequency of excitation. Theoretical results are obtained using $\mu_{21} = 0.013$ and $\mu_{22} = 0.025$, h_{eff}=44 mm, and (a) even magnetic field (EMFD), (b) odd magnetic field (OMFD). Dashed line represent unstable theoretical response.

initially oriented to have opposite polarity, then one magnet was reversed to produce similar polarity. This results, respectively, in the magnetic field distributions EMFD and OMFD as shown in Fig. 4.10. By inspecting Fig. 4.22(a), it evident that, except near the first mode, when using the EMFD, the harvester is able to produce higher voltage peaks near the (even) modal frequencies, while it does not produce any measurable voltage near the (odd) modal frequencies. On the other hand, as Fig. 4.22(b), for the OMFD, the harvester can only produce a measurable output voltage near the odd modal frequencies, while the output voltage is negligible near the even modal frequencies. This further emphasises the relationship between the output voltage and a weighted orthogonality between the mode shape of the response and the MFD.

When the harvester is excited directly and regardless of the MFD, measurable voltage level can be produces near the first and third modal frequencies (odd) as shown in Fig. 4.22 (c), and (d). This is because the excitation is orthogonal to the even mode shapes of the sloshing liquid column and hence only odd modes can be directly excited regardless of the direction MFD.

In order to fairly compare the performance of the harvester, the variation of the output power per unit acceleration with the frequency for both direct and parametric excitation is investigated as depicted in Fig. 4.23. Figure 4.23 (a) shows the output power per unit acceleration for the harvester under parametric excitation around twice the first modal frequency, while Fig. 4.23 (b), depict the output power per unit acceleration for the harvester under direct excitation around the first modal frequency. It is evident that, the output power associated with the parametric excitation is four times larger than the output power generated under direct excitation. This proves that, as

long as the threshold for the activation of the parametric resonance is achieved, the harvester under parametric excitation can deliver a better performance than the direct excitation.

Another key advantage of the parametric excitation is the ability to activate different modes of the harvester by simply changing the applied MFD, while its restricted only around the first modal frequency for the direct excitation. On the other hand, direct excitation does not require a threshold acceleration level to start producing power, and it perform better under small acceleration levels.

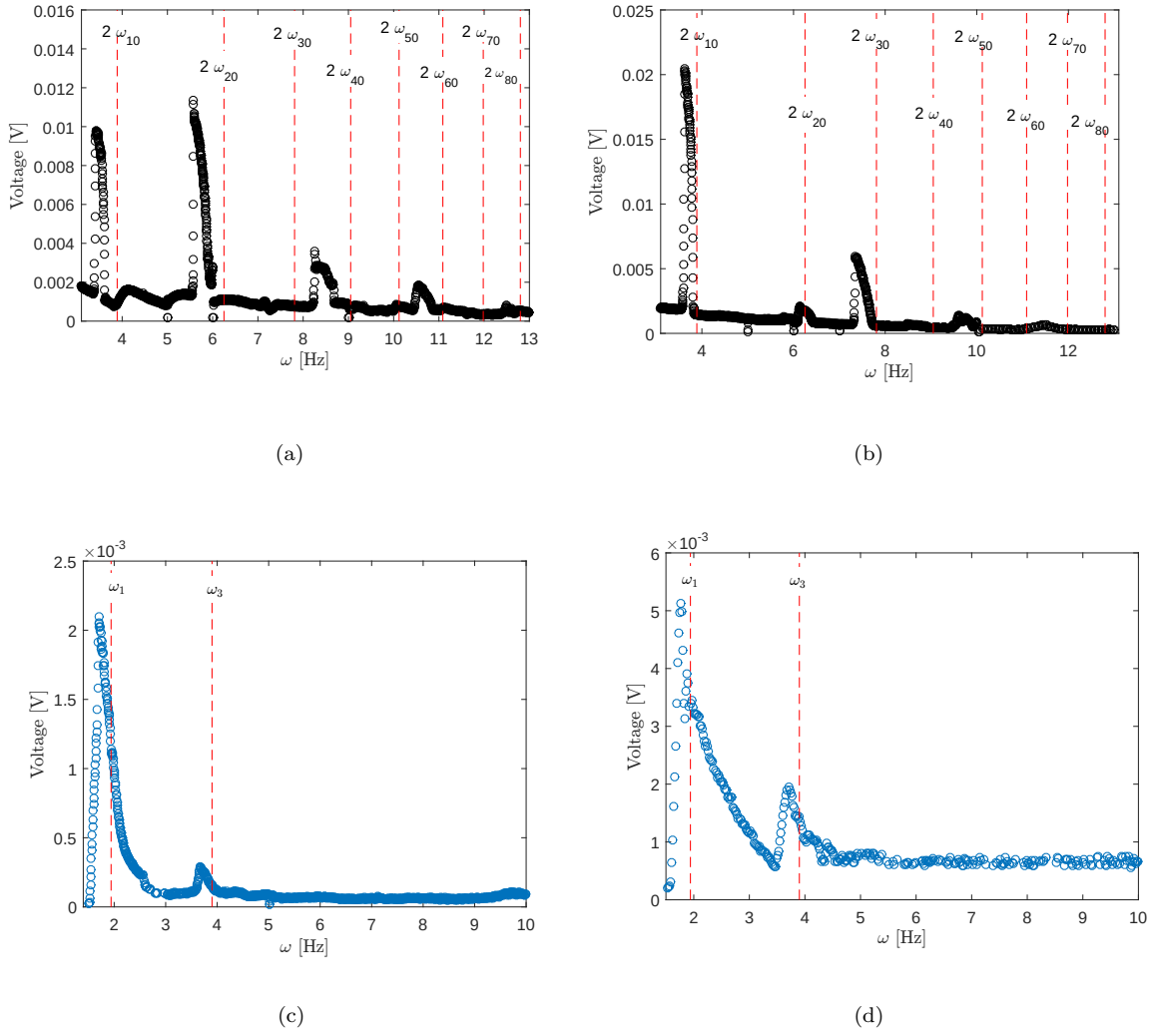

Figure 4.22: Variation of the output voltage with the frequency using a chirp frequency input. Results are obtained for fluid height of 46 mm, a base acceleration of 0.35 m/sec^2 (a) EMFD under parametric excitation, (b) OMFD under parametric excitation, (c) EMFD under direct excitation, and (d) OMFD under direct excitation

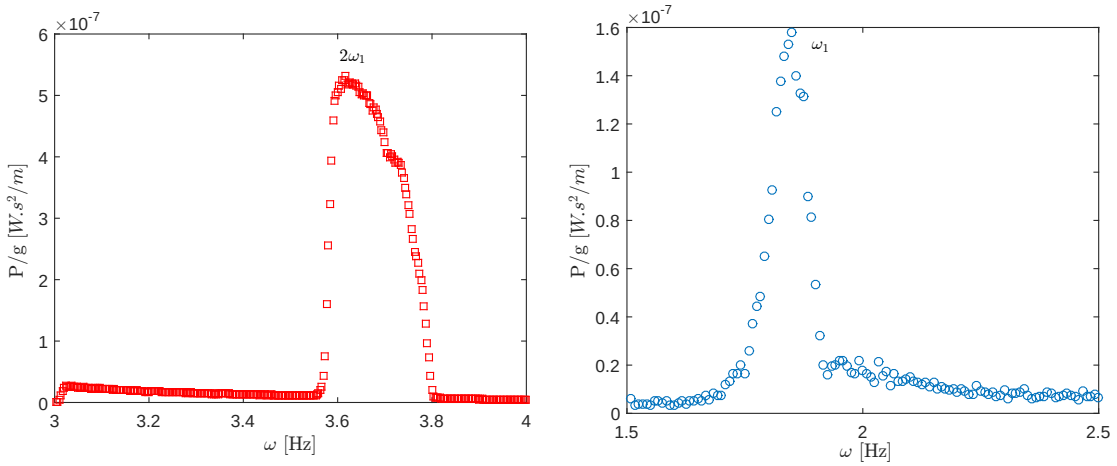

(a) (b)

Figure 4.23: Variation of the output power per unit acceleration with the frequency as obtained for the MFD (MFD3) shown in Fig. 4.2. (a) Parametric excitation, and (b) direct excitation.

Chapter 5

Exploratory Component: Experimental Investigation of Hybrid Energy Harvesting and Vibration Absorption Using Ferrofluids

This chapter explores the idea of utilizing ferrofluids for concurrent vibration absorption and energy harvesting. To this end, we propose to incorporate a pick-up coil in the design of traditional tuned magnetic-fluid dampers to allow for simultaneous electric power extraction and vibration mitigation. The extracted electric energy can be used to power wireless sensors and other low-power consumption devices for structural health monitoring applications.

5.1 Introduction

Failure caused by excessive vibrations remains one of the major concerns in the industrial and civil engineering communities. Vibrations can cause severe damage in machinery and structures

especially those with low damping properties. In machinery, excessive vibrations can result from a number of conditions, acting alone or in combination, such as imbalances, misalignments, looseness, and wear. Similarly, structures in general, are subjected to dynamic loads resulting from dynamic flow fields, earthquakes, traffic loads, etc. For instance, vortex induced vibrations is one of the most detrimental phenomena which cause large amplitude oscillations in bridges, offshore structures, smoke stacks, marine cables, towers, pipelines. The infamous Tacoma bridge collapse, Fig. 5.1, is just one example of how excessive oscillations can result in structural failure. This has motivated researchers to explore efficient and economical techniques to reduce vibrations in order to increase comfort, safety, performance, and reliability.

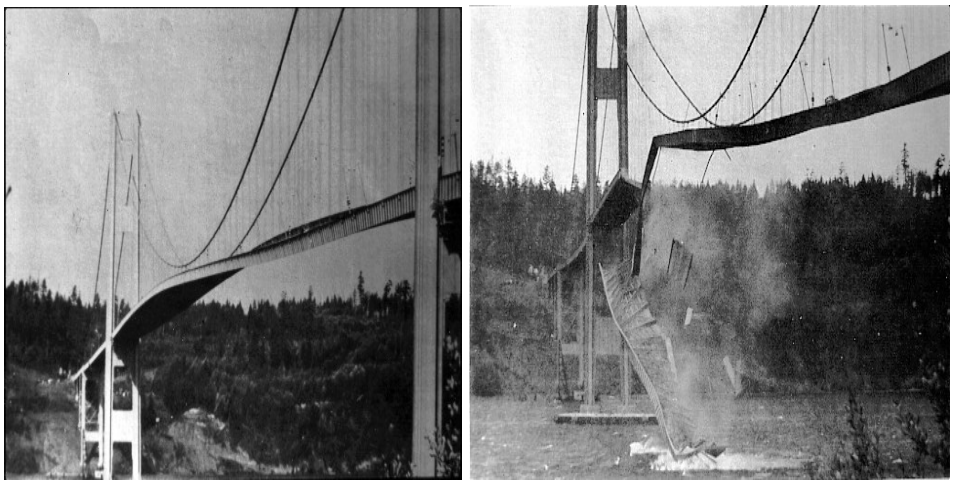

Figure 5.1: Tacoma Narrow Bridge, USA, Washington State, 1940

5.1.1 Current Approaches for Structural Vibration Suppression

Researchers proposed various techniques to mitigate structural vibrations. Some of the proposed techniques require modifications of the structural design by incorporating base isolation, structural bracing, viscoelastic dampers, or by adding damping or stiffness devices [43, 44, 45]. Those techniques, however, have there own restrictions such as cost, periodic maintenance, and tuning difficulty.

Other proposed techniques depend on the design of auxiliary subsystems, also known as vibration absorbers, which are mounted on the structure of interest to channel energy from the structure to the auxiliary subsystem where energy is then dissipated. For structural vibration

mitigation, three types of vibration absorbers are most widely utilized. In what follows, we provide a brief description of these absorbers.

5.1.2 Tuned-Mass-Damper (TMD) Vibration Absorber

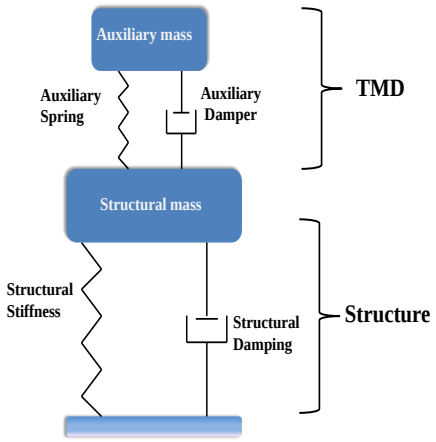

Figure 5.2: A schematic of a tuned mass damper (TMD) absorber.

TMDs are passive mechanical absorbers that use an auxiliary mass-spring-damper system to increase the damping capacity of a given structure as shown in Fig. 5.2. When the structure starts to move due to external excitations, the TMD is excited through the mechanical coupling between the structure and the absorber. This channels a portion of the input energy from the main structure to the TMD, where it is dissipated by viscous dampers [46, 47, 48, 49, 50]. In order to achieve maximum energy transfer from the structure to the TMD, the natural frequency of the TMD is tuned to be equal to the natural frequency of the structure itself such that linear resonance is activated.

Figure 5.3(a) depicts the typical response of a tuned TMD system and the associated structure. The figure demonstrates that the response at the peak frequency of the main system can be reduced significantly upon mounting the TMD. One major disadvantage of the TMD however, lies in the fact that it is not always easy to tune its fundamental frequency to that of the main structure. Any small variations in the fundamental frequency of the TMD around the modal frequency of the structure can result in significant drop in performance. For instance, if the natural frequency of the main structure is shifted by 15%, the performance of the TMD drops significantly as shown in

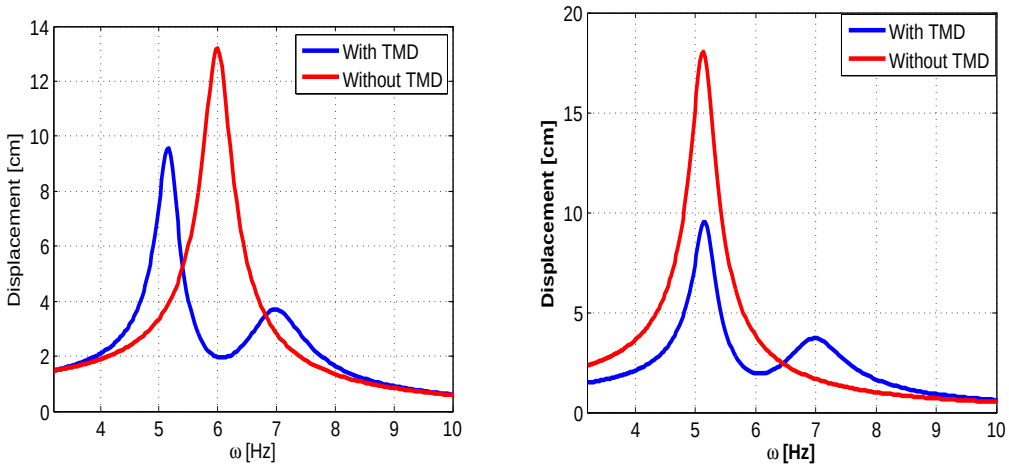

(a) (b)

Figure 5.3: Frequency response of the main structure for (a) perfect tuning, and (b) 15 % shift between the fundamental frequencies of the main structure and the TMD.

Fig. 5.3(b). In such a scenario, re-tuning the TMD to the fundamental frequency of the structure, the mass ratio has to be changed from 5% to 3.66%. This means that a typical TMD mass of 300,000 kg should be replaced by a 219,600 kg mass. This difficulty in re-tuning, motivated researchers to find other effective techniques with a higher retuning flexibility .

5.1.3 Tuned Liquid Damper (TLD) Vibration Absorber

Researchers introduced tuned-liquid dampers TLDs in 1979 [51]. As shown in Fig. 5.4, TLDs are fluid-filled containers that are mounted on the structure of interest to reduce the amplitude of its oscillation when subjected to external excitations. The geometric and material properties of the fluid are specifically chosen such that the frequency of the fundamental sloshing mode of the TLD is very close to the first modal frequency of the structure. As shown in Fig. 5.5, when the structure starts to oscillate due to external loads, the motion of the sloshing fluid in the tank acts as a vibration absorber channelling energy from the structure to the moving fluid and reducing the amplitude and settling time of the structural oscillations.

Shallow and deep water TLDs as well as single and multiple liquid dampers have been developed and analyzed to study their damping characteristics [52, 53, 54, 55, 56, 57, 58, 59]. The key advantage remains that, regardless of its design, the natural frequency of the TLD can be easily

Figure 5.4: One Rincon Hill building, San Francisco 590 ft skyscraper, CA, USA.

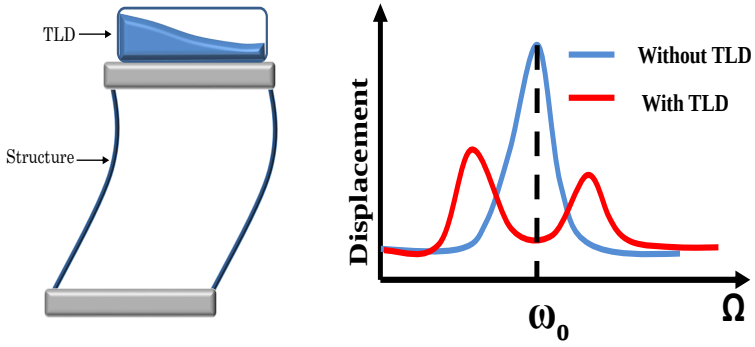

Figure 5.5: A schematic of tuned-liquid damper and its typical frequency response.

adjusted by changing the height of the fluid in the tank. This can be easily achieved by pumping or removing fluid from the tank. Figure 5.6 shows variation of the fundamental frequency of the TLD with respect to the liquid height in a rectangular container of dimensions ??. When compared to the traditional TMD, the TLD is much easier to re-tune. For instance, as shown in Fig. 5.6, for a 15 % frequency shift in the first modal frequency of the TLD, a change in liquid height from 106.4 mm to 73.76 mm is required.

Due to this desirable characteristic, TLDs have been effectively implemented to reduce structural vibrations on different types of structures [60, 61, 62, 63, 64, 65]. One Rincon Hill building in San Francisco, CA represents one infamous example wherein a TLD has been used to reduce structural oscillations, Fig. 5.4. Additionally, TLDs have also been used to reduce vibrations in satellite systems, marine vessels, towers, tall buildings, steel structures, and cable bridges [66, 67,

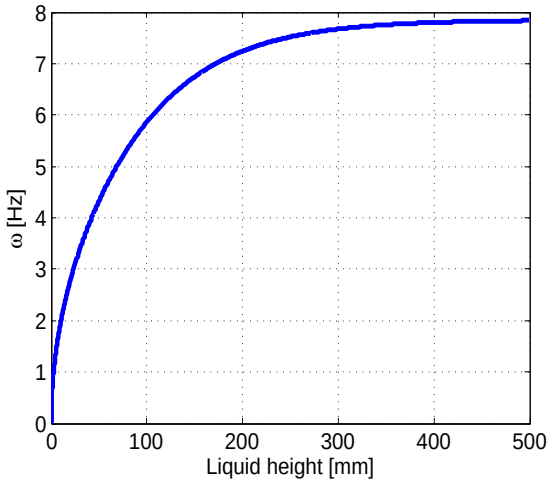

Figure 5.6: Variation of the first modal frequency of the fluid column with the liquid height for a rectangular tank.

68, 69, 70, 71, 72].

5.1.4 Tuned Magnetic Fluid Damper (TMFD) Vibration Absorber

While passive TLDs have been effectively utilized to reduce structural vibrations, changing their natural frequency to match the oscillation frequency of the structure cannot happen in real time. To overcome this problem, various researchers proposed the use of active tuned-magnetic-Fluid dampers (TMFDs) which essentially incorporate magnetic fluids or ferrofluids as the sloshing element as depicted in Fig. 5.7. Such vibration absorbers have the key advantage of allowing real time variation of their sloshing natural frequency by applying an external magnetic field. Specifically, since ferrofluids are composed of nanoscale ferromagnetic particles suspended in a carrier fluid; when an external magnetic field is applied, the average direction of the fluid magnetization becomes parallel to the external field and the ferrofluid particles become harder to rotate when subjected to external excitation. This has the influence of increasing the fluid's viscosity and, with that, its natural frequency.

Multiple researchers examined the influence of applying a tangential magnetic field on the modal frequencies of the sloshing magnetic fluid [73, 74, 75, 76, 77, 78, 79]. It was observed that, when applying an external magnetic field, the modal frequency can be increased in real time providing a new approach for active vibration absorption.

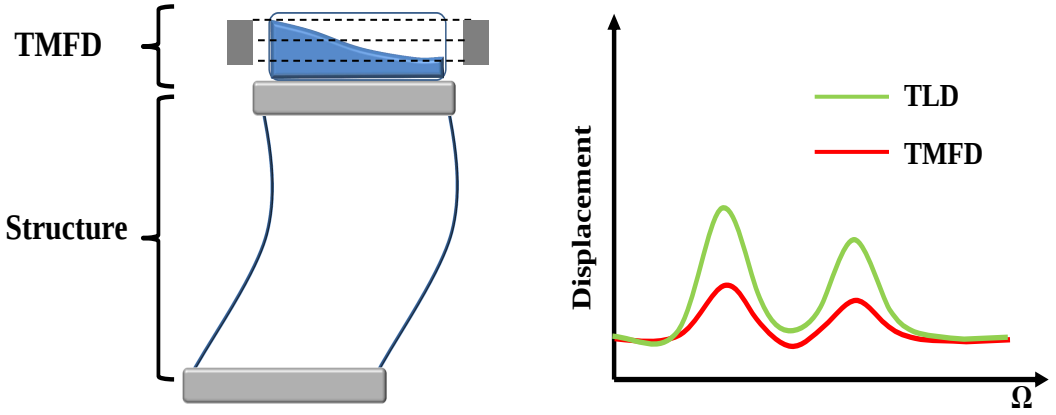

(a) (b)

Figure 5.7: Tuned-magnetic-fluid damper, TMFD. (a) Schematic, and (b) typical response as compared with the TLD.

Figure 5.7(b) shows the response of a structure after installing a TLD and a TMFD auxiliary absorbers. The liquid height inside the TLD, and TMFD containers is chosen such that the first modal frequency of the sloshing liquid is equal to the fundamental frequency of the structure. Furthermore, the magnetic intensity, polarity, and the location of the magnets of the TMFD are tuned such that the TMFD achieves optimal suppression capabilities. As shown in Figure 5.7(b), vibration suppression can be enhanced significantly upon incorporating a TMFD into the structure while actively tuning the magnet field.

Based on the previous discussion, it becomes evident that, by employing ferrofluids in the design of vibration absorbers, significant improvements in the performance is realized via both internal passive tuning of the liquid height and external active tuning of the magnetic field.

5.2 Experiment Investigation

To investigate the feasibility of the proposed concept, the experimental setup shown in Fig. 5.8 is constructed. The Aluminum structure represents a prototype of a single story building. The prototype, which consists of four beams clamped at one end to a base support and on the other end to the four corners of an end mass, has a length of 30.5 cm and a total mass of 3.54 kg. The

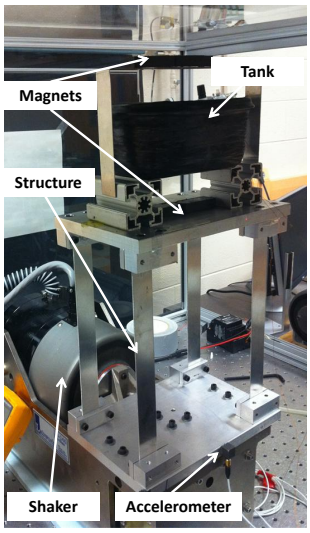

Figure 5.8: Experiment setup.

total mass also includes the mass of the empty container mounted at the top, the magnets used for magnetization purposes, and the coil used to harvest energy. The whole structure is mounted on electrodynamic shaker which exerts harmonic acceleration of $0.07g$ m/s ^{2} at the base. Using a harmonic frequency sweep, the first modal frequency of the structure (without the fluid) is found to be 2.04 Hz, and the structural damping ratio is obtained at 1.15%.

5.3 Vibration Suppression Using TLD

First, we investigate the effectiveness of using the TLD for vibration suppression. Both water and ferrofluid with zero magnetization are utilized. The ferrofluid used is a light hydrocarbon-based 15% by volume concentration of ne magnetite particles, Fe3O4. Its density, saturation magnetization, and magnetic susceptibility are given as ρ =1.21 g/cm3, ms =440 Gauss, and χ= 2.64, respectively. A rectangular container with a length of 13.7 cm, width 9.7 cm and a height of 6.6 cm, is used to carry the liquid material. For effective vibration suppression, the first modal frequency of the sloshing liquid is matched to the natural frequency of the structure. It was found that a liquid height of approximately 17.55 mm is necessary to produce a sloshing frequency of 2.04 Hz.

Figure 5.9 depicts variation of the deflection's amplitude, X_s, of the end mass with the frequency of excitation using an empty container, and with water-based and ferrofluid-based (no magnetization) TLDs. A maximum deflection amplitude of 1.97 cm is recorded at the resonance

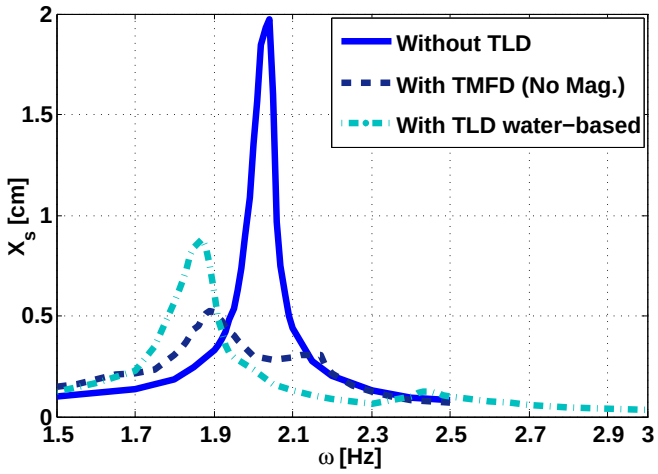

Figure 5.9: Frequency response of the structure with/without TLD

frequency for the structure with the empty tank. Upon installing the water-based TLD, the amplitude of the displacement dropped by 90 % near the resonant frequency of the structure. Due to the second degree-of-freedom introduced by the sloshing liquid, two peaks appear on either side of the resonance frequency of the structure. The larger of the two peaks is still around 55% smaller than the maximum value obtained at resonance with the empty tank. The ferrofluid-based TLD produces a similar response behavior to the water-based TLD but with a better suppression capabilities as clearly shown in Fig. 5.9. This is due to the higher effective mass of the ferrofluid as reported by Fujino et al. [63]. The two peaks appearing in the frequency response of structure when using the ferrofluid-based TLD are also closer to each other due to the higher viscosity of the ferrofluid.

5.4 Vibration Suppression Using TMFD

In this section, the influence of the fluid magnetization on the frequency response of the structure is investigated. To that end, an external magnetic field is generated in the fluid using four vertically-magnetized permanent magnets that have a magnetic flux of 92 mT at their surface. The magnetic field in the fluid is altered by changing the distance between the magnets and the lower and upper surfaces of the container as shown in Table. 5.1.

It is clearly evident in Fig. 5.10 that, when the magnets are far away from the tank as in configurations 1 and 2, the magnetic field has a very little influence on the sloshing behavior of the

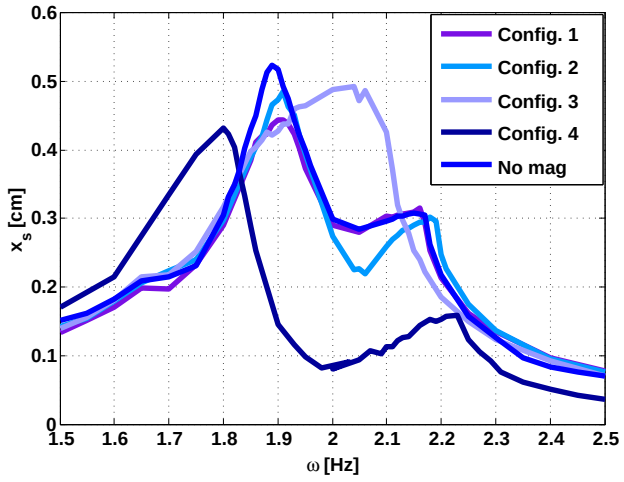

Figure 5.10: Frequency response of the structure with TMFD at different magnetic fields

Table 5.1: Configurations of the permanent magnets of TMFD.

Configuration	Top Magnet [cm]	Bottom Magnet [cm]
1	1.25	2.5
2	1.25	1.25
3	0	1.25
4	0	2.5
5	0	0

liquid with very little additional energy being absorbed by the sloshing liquid as compared to the no magnetization case. In such a scenario, the magnetic field is too small to alter the natural frequency of the sloshing column. However, the magnetic field is still capable of orienting the magnetic dipoles in its direction, because a net voltage can now be measured across the load resistance as evident in Fig. 5.11. When the magnetic field is increased further as in configuration 3, only one clear peak appears in the frequency response. In this case, the viscosity of the fluid, and, thereby, its stiffness increases resulting in the two peaks merging into one which reduces the vibration suppression capabilities of the TMFD. On the other hand, since the magnetic field is stronger, more magnetic dipoles are now oriented in the direction of the field which increases the electromechanical coupling and, hence, the output voltage as can be seen in Fig. 5.11. As shown in Fig. 5.12, when the magnetic field is increased even further as in configuration 5, the viscosity of the ferrofluid increases significantly to the extent where it acts like an added mass. As a result, the TMFD loses its suppression capabilities

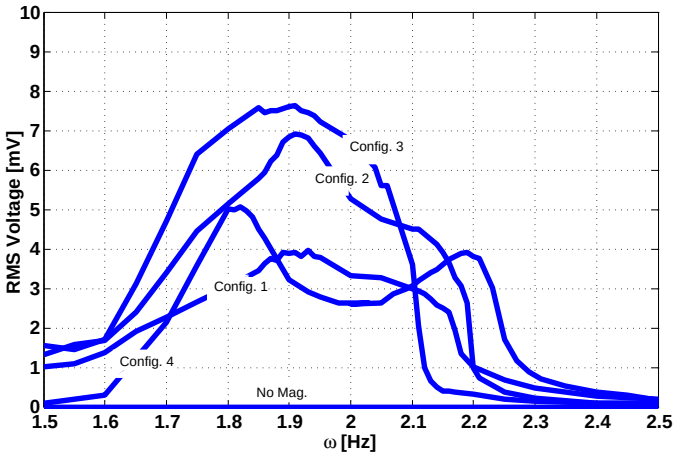

Figure 5.11: RMS voltage output at different magnetic fields

producing only a shift in the resonant frequency towards lower values.

The best vibration suppression capabilities of the TMFD around the resonance frequency occurs when the magnets are placed in configuration 4. This configuration produces a magnetic field in the fluid that is greater than configuration 2 but less than configuration 3. However, the increased suppression capabilities are not accompanied by an increase in the output voltage clearly indicating that the optimal conditions for vibration suppression are different than those necessary for maximum energy generation.

In terms of settling time, which is an important performance characteristic of structural vibration absorbers, the energy harvesting TMFD (configuration 4) results in the fastest settling time as compared to the water-based TLD and all other TMFD configurations, Figs. 5.13(a) and 5.13(b). To calculate the settling time in the experiment, the end mass is subjected to a 2.5 cm initial displacement and the time required for the mass to settle within 10% of the initial displacement is recorded. Based on these calculations, the settling time of the structure without TLD is approximately 333 sec. After installing the water-based TLD, the settling time is reduced to 42 sec, and to 24 sec after installing the ferro-fluid based TLD without magnetization. A very small improvement in the settling time is achieved after using the TMFD (configuration 4) as the settling time is reduced to 23 sec.

To evaluate the energy harvesting capabilities of the harvester, the root mean square (RMS)

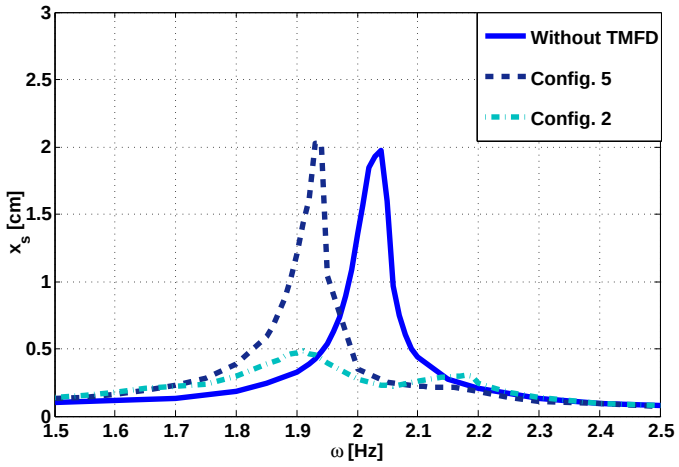

Figure 5.12: Frequency response of the structure with TMFD at high magnetic field

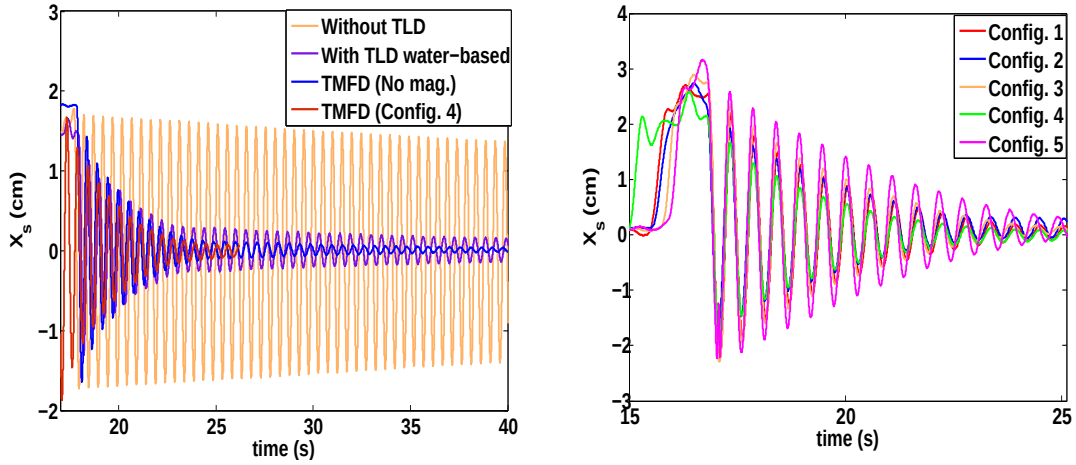

(a) (b)

Figure 5.13: Time response of the structure (a) with, with out TLD, and with TMFD, (b) with TMFD at different magnetic fields.

power per unit acceleration of the harvester is recorded across different resistances as shown in Fig. 5.14. The TMFD with the fourth magnet configuration is used for that purpose and the voltage is recorded at the resonance frequency of the structure (2.04 Hz). It is observed that, in the fourth configuration, the TMFD can produce a maximum power of 0.6 mW/g at a load resistance close to 190 Ω. This load resistance is above the coil resistance which is measured at 160 Ω.

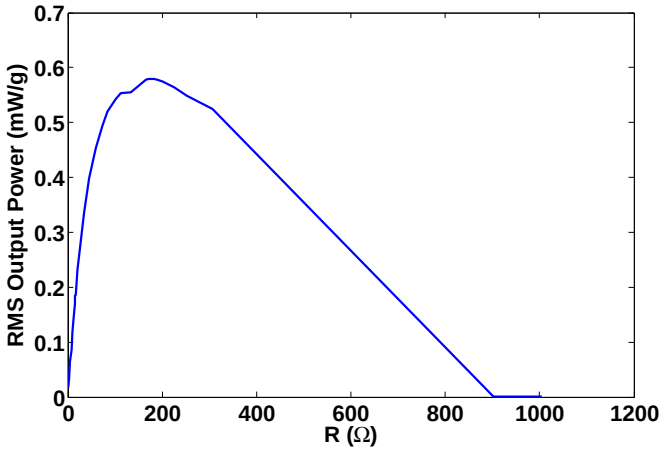

Figure 5.14: Power resistance curve using configuration 4

Chapter 6

Conclusions

This chapter presents the important conclusions of this dissertation. In general, the research presented is focused on investigating the potential of harvesting energy from the sloshing motion of ferrofluids under harmonic base excitations. To achieve the dissertation objectives, two different types of excitations are considered, namely direct and parametric. The following sections summarize the important findings.

6.1 Ferrouid-based energy harvester under direct excitation

The design and performance analysis of a vibratory energy harvester which incorporates a liquid-state transduction element was investigated. The harvester consists of a base excited container carrying a magnetized ferrofluid. The sloshing of the ferrofluid column generates a change in magnetic flux which, in turn, induces a current in an adjacent closed-loop conductor. The height of the sloshing fluid column and the dimensions of the container are specifically chosen such that some of the modal frequencies of the sloshing column are nearly commensurate. It is shown that this choice of parameters activates a two-to-one internal energy pump between the commensurate modes resulting in two response peaks and large amplitude voltages over a wide range of frequencies, thereby improving the steady-state bandwidth of the harvester. The influence of the fluid column height, the magnetic field strength, and the base acceleration on the two-mode voltage response is investigated. It is shown that, for each liquid height, there exists an optimal magnetic field beyond which the magnitude of the output voltage starts to drop. It is also illustrated that as the accelera-

tion level is increased, the two peaks of the response merge into a single peak. For a column height of 20 mm, and magnetic field of 150 Gauss at the center of the container, the harvester was able to produce 80 mW per g at the optimal load.

A theoretical nonlinear model which governs the electro-magneto-hydrodynamics of a ferrofluid based energy harvester was developed. An approximate analytical solution of the model is obtained using the method of multiple scales for a case involving a two-to-one internal resonance between the first two sloshing modes. The results of the theoretical model are compared to experimental findings for several design parameters. The comparison revealed very good qualitative agreement between the model and experiment, and also indicated some quantitative deviations. Such deviations could have resulted from the different assumptions invoked on the analytical model. First, it was assumed that the angle of contact between surface line and the container is ninety degrees and that this point is free to slip on the surface. Actual conditions may deviate from this assumption. Second, it is assumed that the voltage is generated due to the bulk motion of the fluid. However, voltage can also be generated due to the individual rotation of the magnetic dipoles. Third, only two-mode nonlinear interactions were considered. However, when inspecting the results, it becomes evident that other nonlinear interactions are possible in the vicinity of the height-to-width ratios considered in the experiments. Finally, the model neglected the backward coupling resulting from the electric damping. This can actually explain why the wave heights obtained analytically over predict the experimental data.

6.2 Ferrouid-based energy harvester under parametric excitation

A theoretical nonlinear model which governs the electro-magneto-hydrodynamics of a ferrofluid based energy harvester under parametric excitations was developed. An approximate analytical single mode solution of the model is obtained away from any internal resonances using the method of multiple scales. The results of the theoretical model are compared to experimental findings for several design parameters. The comparison revealed very good qualitative agreement between the model and experiment. It was observed that the orthogonality of the magnetic field distribution along the width the container to the shape of the mode being excited plays a critical role in determining the output power of the harvester. Specifically, regardless of the input excitation

level and the size of the induced sloshing waves, very little energy can be harnessed from the environment when the magnetic field distribution is an even (odd) function of the containers width while the mode shape being excited is an odd (even) function of the width. It was shown that, unlike the primary resonance scenario, a threshold excitation level must be achieved in the principle parametric resonance case before the harvester can produce measurable voltage levels. This threshold increases with the strength of the applied magnetic field. Overall, one key advantage of the parametric excitation is its ability to activate different modes of the harvester by simply changing the direction of the applied MFD. In terms of power output, the harvester exhibited better performance under parametric excitations as long as the base acceleration threshold required to activate the principle parametric resonance was met.

6.3 Concurrent Vibration Suppression And Energy Harvesting

An experimental study which examines the design parameters affecting the performance characteristics of a tuned magnetic-fluid damper (TMFD) device designed to concurrently mitigate structural vibrations and harvest vibratory energy has been presented. The device which is mounted on a vibrating structure, consists of a rectangular container carrying a magnetized ferrofluid and a pick-up coil wound around the container to enable energy harvesting. Experiments are performed to investigate the three-way interaction between the vibrations of the structure, the sloshing of the fluid, and the harvesting circuit dynamics. The experimental response of the device is compared against the conventional TMFD at different excitation levels and frequencies. Results demonstrating the influence of the significant parameters on the relative performance are presented and discussed in terms of vibration suppression and power generation capabilities. It is shown through an experimental study that a TMFD employing ferrofluids can be used effectively to reduce structural vibrations while simultaneously acting as an electromagnetic energy harvester. It was also demonstrated that, the optimal magnetic field for which vibration suppression is most effective, is different than the optimal field for which the output power is maximized.

Bibliography

[1] Stefano Gregori, Yunlei Li, Huijuan Li, Jin Liu, and Franco Maloberti. 2.45 ghz power and data transmission for a low-power autonomous sensors platform. In *Low Power Electronics and Design, 2004. ISLPED'04. Proceedings of the 2004 International Symposium on*, pages 269–273. IEEE, 2004.

[2] Jong-Wan Kim, Hidekuni Takao, Kazuaki Sawada, and Makoto Ishida. Integrated inductors for rf transmitters in cmos/mems smart microsensor systems. *Sensors*, 7(8):1387–1398, 2007.

[3] Wouter Bracke, P Merken, Robert Puers, and Christiaan Van Hoof. Generic architectures and design methods for autonomous sensors. *Sensors and Actuators A: Physical*, 135(2):881–888, 2007.

[4] Joseph Paradiso, Thad Starner, et al. Energy scavenging for mobile and wireless electronics. *Pervasive Computing, IEEE*, 4(1):18–27, 2005.

[5] C Shearwood and Rob B Yates. Development of an electromagnetic micro-generator. *Electronics Letters*, 33(22):1883–1884, 1997.

[6] Rajeevan Amirtharajah and Anantha P Chandrakasan. Self-powered signal processing using vibration-based power generation. *Solid-State Circuits, IEEE Journal of*, 33(5):687–695, 1998.

[7] Henry A Sodano, Daniel J Inman, and Gyuhae Park. A review of power harvesting from vibration using piezoelectric materials. *Shock and Vibration Digest*, 36(3):197–206, 2004.

[8] Henry A Sodano, Daniel J Inman, and Gyuhae Park. Generation and storage of electricity from power harvesting devices. *Journal of Intelligent Material Systems and Structures*, 16(1):67–75, 2005.

[9] Shad Roundy. On the effectiveness of vibration-based energy harvesting. *Journal of intelligent material systems and structures*, 16(10):809–823, 2005.

[10] Vinod R Challa, MG Prasad, Yong Shi, and Frank T Fisher. A vibration energy harvesting device with bidirectional resonance frequency tunability. *Smart Materials and Structures*, 17(1):015035, 2008.

[11] F Cottone, H Vocca, and L Gammaitoni. Nonlinear energy harvesting. *Physical Review Letters*, 102(8):080601, 2009.

[12] A Erturk, J Hoffmann, and DJ Inman. A piezomagnetoelastic structure for broadband vibration energy harvesting. *Applied Physics Letters*, 94(25):254102, 2009.

[13] Einar Halvorsen. Energy harvesters driven by broadband random vibrations. *Microelectromechanical Systems, Journal of*, 17(5):1061–1071, 2008.

[14] G Litak, MI Friswell, and S Adhikari. Magnetopiezoelastic energy harvesting driven by random excitations. *Applied Physics Letters*, 96(21):214103, 2010.

[15] Niell G Elvin, Nizar Lajnef, and Alex A Elvin. Feasibility of structural monitoring with vibration powered sensors. *Smart materials and structures*, 15(4):977, 2006.

[16] Samuel C Stanton, Alper Erturk, Brian P Mann, Earl H Dowell, and Daniel J Inman. Nonlinear nonconservative behavior and modeling of piezoelectric energy harvesters including proof mass effects. *Journal of Intelligent Material Systems and Structures*, 23(2):183–199, 2012.

[17] Angela Triplett and D Dane Quinn. The effect of non-linear piezoelectric coupling on vibration-based energy harvesting. *Journal of Intelligent Material Systems and Structures*, 20(16):1959–1967, 2009.

[18] CB Williams, C Shearwood, MA Harradine, PH Mellor, TS Birch, and RB Yates. Development of an electromagnetic micro-generator. In *Circuits, Devices and Systems, IEE Proceedings-*, volume 148, pages 337–342. IET, 2001.

[19] Christophe Serre, Alejandro Pérez-Rodríguez, Nuria Fondevilla, Emile Martincic, Susanna Martínez, Joan Ramon Morante, Josep Montserrat, and Jaume Esteve. Design and implementation of mechanical resonators for optimized inertial electromagnetic microgenerators. *Microsystem Technologies*, 14(4-5):653–658, 2008.

[20] BP Mann and ND Sims. Energy harvesting from the nonlinear oscillations of magnetic levitation. *Journal of Sound and Vibration*, 319(1):515–530, 2009.

[21] Dewei Jia, Jing Liu, and Yixin Zhou. Harvesting human kinematical energy based on liquid metal magnetohydrodynamics. *Physics Letters A*, 373(15):1305–1309, 2009.

[22] A. Bibo, R. Masana, A. King, G. Li, and M. Daqaq. Electromagnetic ferrofluid-based energy harvester. *Journal Physics Letters A*, 43(376):2163–2166, May 2012.

[23] Ranjan Ganguly, Amit P Gaind, Swarnendu Sen, and Ishwar K Puri. Analyzing ferrofluid transport for magnetic drug targeting. *Journal of Magnetism and Magnetic Materials*, 289:331–334, 2005.

[24] Andreas Jordan, P Wust, H Fähling, W John, A Hinz, and R Felix. Inductive heating of ferrimagnetic particles and magnetic fluids: physical evaluation of their potential for hyperthermia. *International Journal of Hyperthermia*, 25(7):499–511, 2009.

[25] Claudio Scherer and Antonio Martins Figueiredo Neto. Ferrofluids: properties and applications. *Brazilian Journal of Physics*, 35(3A):718–727, 2005.

[26] Maryamalsadat Lajvardi, Jafar Moghimi-Rad, Iraj Hadi, Anwar Gavili, Taghi Dallali Isfahani, Fatemeh Zabihi, and Jamshid Sabbaghzadeh. Experimental investigation for enhanced ferrofluid heat transfer under magnetic field effect. *Journal of Magnetism and Magnetic Materials*, 322(21):3508–3513, 2010.

[27] K Raj and R Moskowitz. Commercial applications of ferrofluids. *Journal of Magnetism and Magnetic Materials*, 85(1):233–245, 1990.

[28] K Raj, B Moskowitz, and R Casciari. Advances in ferrofluid technology. *Journal of magnetism and magnetic materials*, 149(1):174–180, 1995.

[29]

[30] John P McTague. Magnetoviscosity of magnetic colloids. *The Journal of Chemical Physics*, 51(1):133–136, 1969.

[31] Thiago Seuaciuc-Osório and Mohammed F Daqaq. Effect of bias conditions on the optimal energy harvesting using magnetostrictive materials. In *The 15th International Symposium on: Smart Structures and Materials & Nondestructive Evaluation and Health Monitoring*, pages 69280B–69280B. International Society for Optics and Photonics, 2008.

[32] Noel E DuToit and Brian L Wardle. Experimental verification of models for microfabricated piezoelectric vibration energy harvesters. *AIAA journal*, 45(5):1126–1137, 2007.

[33] Jamil M Renno, Mohammed F Daqaq, and Daniel J Inman. On the optimal energy harvesting from a vibration source. *Journal of sound and vibration*, 320(1):386–405, 2009.

[34] BP Mann and ND Sims. Energy harvesting from the nonlinear oscillations of magnetic levitation. *Journal of Sound and Vibration*, 319(1):515–530, 2009.

[35] Vinod R Challa, MG Prasad, Yong Shi, and Frank T Fisher. A vibration energy harvesting device with bidirectional resonance frequency tunability. *Smart Materials and Structures*, 17(1):015035, 2008.

[36] Ali Hasan Nayfeh. *Nonlinear interactions*. Wiley, 2000.

[37] Raouf A. Ibrahim. *Liquid Sloshing Dynamics: Theory and Applications*. Cambridge University Press, 2005.

[38] Ali Hasan Nayfeh. *Nonlinear interactions*. Wiley, 2000.

[39] SF Alazemi, A Bibo, and Mohammed Farid Daqaq. A ferrofluid-based energy harvester: An experimental investigation involving internally-resonant sloshing modes. *The European Physical Journal Special Topics*, 224(14-15):2993–3004, 2015.

[40] AH Nayfeh. Perturbation techniques, 1981.

[41] M. Faraday. On a Peculiar Class of Acoustical Figures; and on Certain Forms Assumed by a Group of Particles upon Vibrating Elastic Surfaces. *Philosophical Transactions of The Royal Society*, 121:299–318, 1831.

[42] J. Strutt and L. Rayleigh. On the Crispations of Fluid Resting upon a Vibrating Support. *Philosophical Magazine*, 16:50–53, 1883.

[43] Lin Su, Goodarz Ahmadi, and Iradj G Tadjbakhsh. A comparative study of performances of various base isolation systems, part i: shear beam structures. *Earthquake engineering & structural dynamics*, 18(1):11–32, 1989.

[44] Ian G Buckle and Ronald L Mayes. Seismic isolation: history, application, and performance-a world view. *Earthquake spectra*, 6(2):161–201, 1990.

[45] Ri-Hui Zhang, TT Soong, and P Mahmoodi. Seismic response of steel frame structures with added viscoelastic dampers. *Earthquake engineering & structural dynamics*, 18(3):389–396, 1989.

[46] KCS Kwok and B Samali. Performance of tuned mass dampers under wind loads. *Engineering Structures*, 17(9):655–667, 1995.

[47] T Pinkaew and Y Fujino. Effectiveness of semi-active tuned mass dampers under harmonic excitation. *Engineering Structures*, 23(7):850–856, 2001.

[48] Genda Chen and Jingning Wu. Optimal placement of multiple tune mass dampers for seismic structures. *Journal of Structural Engineering*, 127(9):1054–1062, 2001.

[49] Allen J Clark et al. Multiple passive tuned mass damper for reducing earthquake induced building motion. In *Proc*, volume 9, pages 779–784, 1988.

[50] Davorin Hrovat, Pinhas Barak, and Michael Rabins. Semi-active versus passive or active tuned mass dampers for structural control. *Journal of Engineering Mechanics*, 109(3):691–705, 1983.

[51] J Kim Vandiver and Shuhei Mitome. Effect of liquid storage tanks on the dynamic response of offshore platforms. *Applied Ocean Research*, 1(2):67–74, 1979.

[52] VJ Modi and F Welt. Damping of wind induced oscillations through liquid sloshing. *Journal of Wind Engineering and Industrial Aerodynamics*, 30(1):85–94, 1988.

[53] VJ Modi. Vibration damping through liquid sloshing, part 2: Experimental results. *Journal of vibration and acoustics*, 114:17, 1992.

[54] Y Saoka, T Tamaki, F Sakai, and S Takaeda. A proposal for suppression of structural vibrations by tuned liquid column damper. In *Proceedings of the 43rd Annual Meeting*. JSCE, 1989.

[55] Y Fujino, LM Sun, and K Koga. Simulation and experiment on tuned liquid damper subjected to pitching motion. *JSCE J Struct Eng A*, 37:805–814, 1991.

[56] T Noji, H Yoshida, E Tatsumi, H Kosaka, and H Haguida. Study of water-sloshing vibration control damper. *J Struct Const Eng AIJ*, 411:97–105, 1990.

[57] Y Fujino and LM Sun. Vibration control by multiple tuned liquid dampers (mtlds). *Journal of Structural Engineering*, 119(12):3482–3502, 1993.

[58] K Shankar and T Balendra. Application of the energy flow method to vibration control of buildings with multiple tuned liquid dampers. *Journal of Wind Engineering and Industrial Aerodynamics*, 90(12):1893–1906, 2002.

[59] CG Koh, S Mahatma, and CM Wang. Reduction of structural vibrations by multiple-mode liquid dampers. *Engineering structures*, 17(2):122–128, 1995.

[60] K. Fujii, Y. Tamura, T. Sato, and T. Wakahara. Wind-induced vibration of tower and practical applications of tuned sloshing damper. *Journal of Wind Engineering and Industrial Aerodynamics*, 33(12):263 – 272, 1990.

[61] T. Wakahara, T. Ohyama, and K. Fujii. Suppression of wind-induced vibration of a tall building using tuned liquid damper. *Journal of Wind Engineering and Industrial Aerodynamics*, 43(13):1895 – 1906, 1992. International Conference on Wind Engineering.

[62] T. Ueda, R. Nakagaki, and K. Koshida. Suppression of wind-induced vibration by dynamic dampers in tower-like structures. *Journal of Wind Engineering and Industrial Aerodynamics*, 43(13):1907 – 1918, 1992. International Conference on Wind Engineering.

[63] Y. Fujino, B. Pecheco, P. Chaiseri, and L. Sun. Parametric studies on tuned liquid damper (TLD) using circular containers by free-oscillation experiment. *Journal Structural Eng. and Earthquake Eng*, 5(2):381–391, October 1988.

[64] Y. Fujino and L. Sun. Vibration control by multiple tuned liquid dampers (mtlds). *Journal Structural Engineering*, 119(12):3482–3502, December 1993.

[65] L. Sun, Y. Fujino, P. Chaiseri, and B. Pacheco. The properties of tuned liquid dampers using a tmd analogy. *Journal Earthquake Eng. Struct. Dyn.*, 24(7):967–976, July 1995.

[66] JC Amieux and M Dureigne. Analytical design of optimal nutation dampers. *Journal of Spacecraft and Rockets*, 9(12):934–935, 1972.

[67] Y Matsuura, K Matsumoto, and M Mizuuchi. On a mean to reduce excited-vibration with the sloshing in a tank. *Journal of the Society of Naval Architects of Japan*, 160, 1986.

[68] Y Tamura, K Fujii, T Sato, T Wakahara, and M Kosugi. Wind-induced vibration of tall towers and practical applications of tuned sloshing damper. In *Proc Workshop Serviceability of Buildings*, pages 228–241, 1988.

[69] T Wakahara, T Ohyama, and K Fujii. Wind response analysis of tld structure system considering nonlinearity of liquid motion. *J Struct Construct Eng AU*, 426:79–88, 1991.

[70] KT Alfriend and TM Spencer. Comparison of filled and partly filled nutation dampers. In *AAS/AIAA Astrodynamics Specialist Conference*, pages 81–141, 1981.

[71] Y Fujino, BM Pacheco, P Chaiseri, and K Fujii. An experimental study on tuned liquid damper using circular containers. *JSCE J Struct*, pages 603–616, 1988.

[72] Y Fujino, BM Pacheco, P Chaiseri, LM Sun, and K Koga. Understanding of tld properties based on tmd analogy. *JSCE J Struct Eng A*, 36:577–590, 1990.

[73] Ronald E. Zelazo and James R. Melcher. Dynamics and stability of ferrofluids: surface interactions. *Journal of Fluid Mechanics*, 39:1–24, 10 1969.

[74] N Omura, K Yamashita, T Sawada, and M Ohaba. Dynamic characteristics of a magnetic fluid column formed by magnetic field. *Journal of Magnetism and Magnetic Materials*, 201(13):297 – 299, 1999.

[75] M. Abe, Y. Fujino, and S. Kimura. Active tuned liquid damper (TLD) with magnetic fluid. *Journal Smart Structure and Materials*, March 1998.

[76] K. Ohno, M. Shimoda, and T. Sawada. Optimal design of a tuned liquid damper using a magnetic fluid with one electromagnet. *Journal Physics: Condensed Matter*, 2008.

[77] K. Ohno, H. Suzuki, and T. Sawada. Analysis of liquid sloshing of a tuned magnetic fluid damper for single and co-axial cylindrical containers. *Journal Magnetism and Magnetic Materials*, 323(10):1389–1393, May 2011.

[78] Y. Ohira, H. Houda, and T. Sawada. Effect of magnetic field on a tuned liquid damper using a magnetic fluid. *Journal International Journal of Applied Electromagnetics and Mechanics*, 13(1).

[79] T Sawada, H Kikura, and T Tanahashi. Kinematic characteristics of magnetic fluid sloshing in a rectangular container subject to non-uniform magnetic fields. *Experiments in fluids*, 26(3):215–221, 1999.